

DISRUPTIVE INSTABILITIES IN A  
POLOIDAL DIVERTOR TOKAMAK

by  
THOMAS HOWARD OSBORNE

A thesis submitted in partial fulfillment of the  
requirements for the degree of

DOCTOR OF PHILOSOPHY  
(Physics)

at the

UNIVERSITY OF WISCONSIN - MADISON

1984

ACKNOWLEDGEMENTS

I would like to thank my advisor Professor Stewart C. Prager for his unfailing enthusiasm and support for this research. He often provided the key ideas needed to bridge impediments to further progress in this work.

I would also like to thank Professor R.N. Dexter for his help and ideas, especially on the  $q < 1$  research, and for the use of his surface barrier diode diagnostic, without which much of this work would not have been possible. I also acknowledge the support of Professor J.C. Sprott, principal investigator for the Tokapole II group, who was responsible for the design and construction of the device.

This work would not have been possible without the expert technical assistance of Tom Lovell, who also kept Tokapole II operating from day to day, despite the odds.

I would also like to thank all the other graduate students and faculty, too numerous to mention, who have contributed ideas or labor to this research.

I am very grateful to Ralph Izzo, Don Monticello, and Wonchull Park of the Princeton Plasma Physics Laboratory, who provided the HIB code, and spent many hours instructing me in the codes use, and discussing its results. I would also like to thank Kevin McGuire of PPPL for his interest in this research and for several useful suggestions.

Finally I would like to acknowledge the contribution of Dr Nancy S. Brickhouse to this research. She deserves a large portion of the credit for the experimental work described in this thesis, especially the soft x-ray data. She is responsible for the discovery of the phase shift in the sawtooth crash in the  $\langle q \rangle = 1$  case, which is of key importance in the overall picture of disruptions in Tokapole II. She has also contributed many ideas to the interpretation of the results. Her perseverance kept this work going on the many occasions when progress appeared to be hopeless.

DISRUPTIVE INSTABILITIES IN A  
POLOIDAL DIVERTOR TOKAMAK

Thomas Howard Osborne

Under the supervision of Associate Professor Stewart C. Prager

Relaxation oscillations in the plasma pressure, that appear as sawtooth oscillations on collimated soft x-ray detectors, are observed in all Tokapole II discharges. These instabilities exhibit characteristics which are unexpected from the usual picture of disruptive instabilities in poloidal divertor tokamaks without a close fitting conducting shell.

Tokamak discharges are observed with safety factor,  $q$ , as low as 0.5 over most of the current channel within the poloidal divertor separatrix. These discharges show sawtooth oscillations, but magnetic probe measurements indicate the central  $q$  values, instead of relaxing to 1, remain nearly fixed. The  $q=1$  surface for this case is very near the separatrix, and there is a small oscillation in  $q$  near the  $q=1$  surface which is time correlated with the sawtooth oscillations. The observation of discharges which maintain  $q < 1$  is at variance with the usual resistive MHD theory of sawtooth oscillations. These discharges have poor energy confinement ( $\tau_E < 50 \mu s$ ).

If  $q=1$ , sawtooth oscillations are observed in which the disruption (sawtooth crash) itself has an  $n=m=1$  helical structure.

This suggests that these disruptions may maintain a single helicity through the nonlinear phase.

At low toroidal plasma current and high toroidal field, several small sawteeth of period 100-200 $\mu$ s are superimposed on giant sawteeth of period 1ms. Precursor oscillations with even  $m$  and odd  $n$  are observed on magnetic loops for both types of sawtooth oscillations. This is consistent with the standard model for a disruption that results from the  $m=2, n=1$  mode. Except at very low electron density, the plasma current is not terminated in a disruption.

As the plasma current is increased with the toroidal magnetic field constant, the giant sawteeth become less regular. At large enough plasma current, only small sawtooth oscillations are observed: these show an  $m=n=1$  precursor in the soft x-ray. An MHD equilibrium code predicts that the  $q=2$  surface is very near the divertor separatrix for this case. This suggests that the  $m=2, n=1$  disruption may be eliminated by the proximity of the  $q=2$  surface and the separatrix. These discharges have good energy confinement time ( $\tau=600\mu$ s).

## TABLE OF CONTENTS

	Page
ABSTRACT	ii
ACKNOWLEDGEMENTS	iv
TABLE OF CONTENTS	vi
I INTRODUCTION	1
A. Background	1
B. Overview of Thesis Research	3
C. Outline of Thesis	4
II. TOKAMAK STABILITY LIMITS	8
A. Introduction	8
B. Low $q$ Operation and the Tokamak Fusion Reactor	12
C. Disruptions Resulting from $m=n=1$ Helical Modes	16
D. Disruptions Resulting from $m>1$ Helical Modes	31
E. $q < 2$ Tokamaks	41
III. APPARATUS AND DIAGNOSTICS	46
A. Tokapole II	46
B. Magnetic Probe Measurements of $q$ and $\phi$	57
C. Soft X-Ray Measurements	65
D. Electric Field Probes	68
IV INTRODUCTION TO RESULTS	76
V. DATA AND ANALYSIS FOR $\langle q \rangle = 3.0$	85
A. Soft X-Ray Data	85

B. Magnetic Precursor Oscillations	97
C. Current Termination in Tokapole II Disruptions	111
D. Transport Across the Equilibrium X-Points During Disruption	117
VI. DATA AND ANALYSIS FOR $\langle q \rangle = 2.0$	123
A. Soft X-Ray Data	123
B. Magnetic Oscillations	132
C. $q < 2$ and the Lack of 2/1 Disruptions	132
VII. DATA AND ANALYSIS FOR $\langle q \rangle = 1.0$	146
A. Soft X-Ray Data	146
B. Interpretation of Disruptive Phase Shift	152
VIII. DATA AND ANALYSIS FOR $\langle q \rangle < 1.0$	158
A. $q < 1$ Discharge General Characteristics	159
B. Connection of Sawtooth Oscillations to $q=1$	164
C. $q$ Oscillations During a Sawtooth	167
D. Heuristic Model for Partial Reconnection	185
E. H1B Resistive MHD Code Results	196
F. Parameter Scaling and Confinement at Low $q$	230
IX. SUMMARY CONCLUSIONS AND SUGGESTIONS FOR FUTURE WORK	247
APPENDIX REDUCED RESISTIVE MHD EQUATIONS TO ORDER $\epsilon^3$	252

BACKGROUND AND OVERVIEWA. Background

"Disruptive instabilities" represent a major impediment to the achievement of reactor plasmas in tokamaks. In these instabilities a large portion of the thermal energy content of the plasma can be rapidly lost to the vessel walls, often resulting in complete termination of the discharge. The understanding and control of disruptions has, for the past 10 years, been one of the major concerns of theoretical and experimental plasma physics. Chapter 2 contains a review of the experimental and theoretical results for disruptive instabilities, and also an account of the relation of these instabilities to the goal of controlled fusion in tokamaks.

A fairly complete understanding of these instabilities, based on the deceptively simple set of single fluid resistive magnetohydrodynamic equations, has emerged from this research. Experimental work led to the identification of helical perturbations to the toroidally symmetric equilibrium, that are precursors to the disruptions. These helical modes are resonant with the pitch of magnetic field lines in the region where their amplitudes are peaked, and grow in amplitude just before the disruption. The time scale for the disruption, and the growth rate for the precursor oscillations is intermediate between the

principal time scales for resistive MHD: the hydromagnetic time scale (the time for an Alfvén wave to propagate around the torus) and the resistive diffusion time scale. These hydromagnetic and resistive time scales can be a factor of  $10^6$  different in today's tokamaks. The great physical insight of a few individuals, led to the recognition of the importance of a small, but finite, resistivity to the stability of the tokamak magnetic topology. Despite the fact that the resistive decay time for the plasma current can be 1000 times the disruption time, even very small values of resistivity allow localized magnetic field line reconnection that affects the magnetic field structure globally. The growth rates of the helically resonant precursor oscillations fit well with the field line reconnection instabilities of resistive MHD linear theory. These results suggested that an explanation of the disruption might be found in the nonlinear behavior of the resistive MHD modes, and led to the building of large computer codes to follow the 3-D nonlinear evolution and interaction of the helical modes. The nonlinear code runs showed that field line reconnection could lead to the destruction or rearrangement of the magnetic surfaces which results in the sudden heat loss.

The extension of nonlinear resistive MHD codes to include high thermal pressure effects, and more complex magnetic geometry, is a topic of current research. Also of current interest is the effect of turbulence, based on the resistive MHD model, on the fine scale

integrity of the magnetic surfaces. It is hoped that this turbulence model may provide an understanding, and perhaps an avenue of control, for the anomalously high electron thermal conductivity that is the chief energy loss channel for tokamaks today.

### B. Overview of Thesis Research

The research of this thesis centers on an attempt to understand certain operational modes and instabilities in Tokapole II, that were unexpected from the point of view of the theory of disruptions. It is possible to operate at tokamak safety factor,  $q$ , values below what would normally be prevented by disruptions. The device has several unusual features which may be related to the ability to operate at low  $q$ . In particular, Tokapole II may be the only poloidal divertor tokamak that is routinely run with substantial plasma current outside the divertor separatrix. This might produce a unique relationship between the location of the magnetic surfaces at which the helical modes are resonant, and the current density gradient which drives the reconnection, that may be responsible for the low  $q$  operation.

The device can be operated with central  $q$  values ( $q=1/\text{field line pitch}$ ) as low as 0.5. In the usual model, when  $q$  drops below 1, a helical mode that is resonant with the magnetic field lines on the  $q=1$  magnetic surface, grows until the current density profile within the  $q=1$  surface is flattened, raising  $q$  above 1 everywhere.

The periodic flattening of the temperature profile that results from the magnetic field line reconnection in this instability is manifested as "sawtooth" oscillations on collimated soft xray detectors. Even though sawtooth oscillations are observed in the soft xrays, the central  $q$  values remain below 1. An attempt has been made to explain the behavior with a nonlinear resistive MHD code. The energy confinement of these very low  $q$  discharges is relatively poor.

At higher toroidal magnetic field, in cases for which the energy confinement is an order of magnitude better than the very low  $q$  case, it appears to be possible to operate with most of the region within the divertor separatrix below  $q=2$  without a major disruption. In these  $q<2$  discharges only internal disruptions are observed. The ability to operate below  $q=2$  without a conducting boundary near the plasma surface would be unique.

If  $q=3$ , disruptions are observed which have magnetic precursor oscillations indicative of the  $m=2$ ,  $n=1$  helical modes seen on other tokamaks. No termination of the plasma current, however, is normally seen for these discharges. This may be the result of the smallness of the disruption major axis shift predicted in Tokapole II magnetic geometry, and the lack of a material boundary near the separatrix.

#### C. Outline of Thesis

Chapter 2 contains a brief review of the experimental and theoretical results for disruptive instabilities, and also an account of the relation of these instabilities to the goal of controlled fusion in tokamaks.

In chapter 3, Tokapole II is described, and some details of the diagnostics and data analysis are given.

Chapter 4 gives a detailed outline of the experimental results and discusses their interrelation.

Chapter 5 discusses the details of high toroidal field discharges in which periodic minor disruptions are observed. These disruptions have magnetic precursor oscillations consistent with the  $m=2$ ,  $n=1$  modes observed on other tokamaks. Distortion of the precursors are consistent with an odd  $m$  even  $n$  mode. The lack of current termination in these disruptions may be related to the small major axis shift that would occur in Tokapole magnetic field geometry. Langmuir probe studies indicate a rapid loss of plasma to the region near the divertor rings during the disruption.

In chapter 6 the high toroidal field  $q<2$  case is discussed. This case exhibits sawtooth oscillations in the soft xrays with  $m=n=1$  precursor oscillations. Fits of the inversion radius for the sawtooth oscillations and various global parameters to a MHD equilibrium code indicate that the  $q=2$  surface is very close to the divertor separatrix.

Chapter 7 give an account of the results for a low toroidal field case with  $q=1$ . Sawtooth oscillations are also observed in these discharges; however, instead of  $m=n=1$  precursor oscillations, the disruption itself propagates with the pitch of an  $m=n=1$  field line. This may be a relatively clear example of a helical structure in the nonlinear phase of the modes growth that is not normally observed, that may be more consistent with the classical Kadomtsev picture than with the propagation of an axisymmetric turbulent region.

Chapter 8 discusses the very low  $q$  data. Here the central  $q$  values remain below 1 during sawtooth oscillations. Some nonlinear resistive MHD code results, with the original position of the  $q=1$  surface near the separatrix in the equilibrium flux plot, showed an apparent saturation of the instability. In these code runs, however, most of the current density profile is flattened; which would have resulted in an experimentally measured  $q$  value near 1. Another resistive MHD code run showed the usual development of the instability with  $q$  relaxing to values greater than 1. The factors which determine whether saturation will occur are not yet understood. Also discussed in this chapter are scalings of various parameters with  $q$ . An attempt is made to account for the poor confinement of these discharges on the basis of localized interchange modes. Although the circular flux surface version of the Mercier criteria suggests instability at these low  $q$  values, more detailed calculations, using the MHD equilibrium code,

indicate that, at the very low pressures of these discharges, even the relatively flat toroidal current profiles observed experimentally have sufficient shear to stabilize these modes.

## CHAPTER 2

TOKAMAK STABILITY LIMITSA. Introduction

Among the first attempts at managing the energy of thermonuclear fusion was the linear "z-pinch."<sup>1</sup> In this device a large current is driven through a plasma discharge column. This current serves to ohmically heat the plasma, and the magnetic field generated compresses the column, isolating it from the vessel walls and further raising the plasma pressure. Unfortunately, this simple type of discharge is unstable to kinking or local pinching off of the current channel. A strong magnetic field added along the column's length can act through its magnetic pressure to prevent the pinching off instability, and also, if it is large enough, can, through its magnetic tension suppress the kink mode as well. Unfortunately, with a large magnetic field component along the discharge length, plasma particles can easily flow along the field and escape. A solution to this free streaming problem is to simply connect the two ends of the current column together forming a torus, and drive the plasma current inductively as a transformer secondary: this is the tokamak configuration.

The  $q$ , or tokamak safety factor, is a measure of the ratio of the magnetic field along the current column,  $B_\phi$ , to the toroidal

plasma current,  $I_p$ . On a field line, in a circular cross section tokamak,

$$q = d\phi/d\theta \approx rB_\phi/RB_\theta, \quad (2.1)$$

where  $\phi$  is the angular toroidal coordinate, and  $\theta$  is the angular poloidal coordinate,  $B_\theta$  is the poloidal magnetic field,  $r$  is the minor radius and  $R$  is the major radius (figure 2-1). In any type of toroidal geometry,

$$q = \lim(\text{toroidal transits}/\text{poloidal transits}), \quad (2.2)$$

where the limit is to an infinite number of toroidal transits. In axisymmetric toroidal geometry,

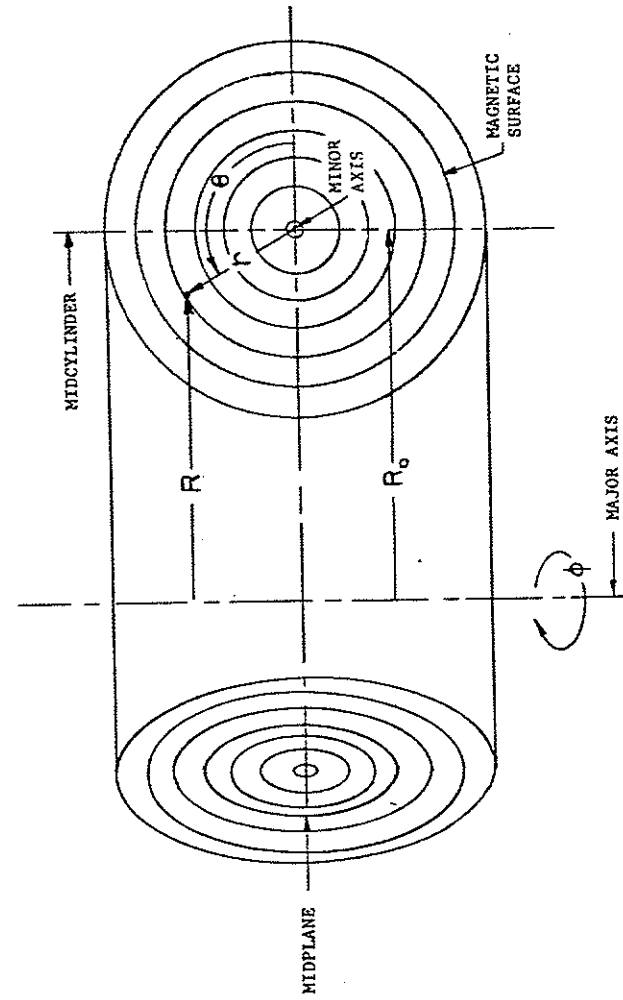
$$q = \frac{d\phi_{\text{tor}}}{d\phi_{\text{pol}}}, \quad (2.3)$$

where  $\phi_{\text{tor}}$  is the flux of the toroidal magnetic field within a magnetic surface, and  $\phi_{\text{pol}}$  is the flux of the poloidal field.

Although operating at sufficiently high  $q$  solves the problem of the  $I_p$  driven modes described above, this is a rather Pyrrhic victory. As will be described in more detail in the next section, the particle and energy confinement in a tokamak depends on the presence of the poloidal magnetic field, and scales inversely with  $q$ . In addition, in order for tokamaks to be feasible as reactors,



FIG. 2-1. Definition of coordinates and terms used in toroidal geometry.



they must be operated at high thermal pressure. The maximum pressure attainable for a given magnetic field strength may be limited by pressure driven instabilities. The limit of the ratio of thermal to magnetic pressure is theoretically predicted to scale inversely with  $q^2$ . These considerations have made low  $q$  operation of great importance in the tokamak controlled fusion program, which has brought an extensive theoretical and experimental effort to bear on understanding the physics of the current driven instabilities, and thereby facilitating their control.

### B. Low $q$ Operation and the Tokamak Fusion Reactor

The power density from fusion reactions is given by<sup>2</sup>

$$P_f = \gamma_{i,j} n_i n_j \langle \sigma v \rangle_{i,j} E_f, \quad (2.4)$$

where  $\gamma_{i,j}=1/2$  for  $i=j$  and  $\gamma_{i,j}=1$  for  $i \neq j$ ,  $n_i$  is the species density,  $\langle \sigma v \rangle_{i,j}$  is the velocity space averaged reaction rate, and  $E_f$  is the energy per fusion.  $\langle \sigma v \rangle_{i,j}$  is a very strongly increasing function of temperature, rising over 3 orders of magnitude for temperatures from 3 to 30 keV. Significant power production in tokamaks, thus, depends on operation at high plasma pressure.

The plasma pressure gradient can drive instabilities which may limit the maximum attainable plasma pressure. If the magnitude of  $B$  decreases in the direction that the pressure decreases, then the volume of a tube with a given amount of magnetic flux increases

while the pressure within it decreases. If a tube from the outside low pressure, high volume region is adiabatically interchanged with a tube from the high pressure, low volume region then the energy of the system will be lowered resulting in an instability which flattens the pressure gradient. In a tokamak the volume of a flux tube is normally dominated by the  $1/R$  variation of the toroidal magnetic field; on the large major radius side of the torus the interchange described above lowers the energy of the plasma, while on the small major radius side of the torus, the pressure gradient is in the direction of decreasing flux tube volume and so the interchange raises the plasma energy. However, if the interchange is localized to the large major radius, or "bad curvature" side, then the displacement of the plasma must vary along a field line. This variation must bend the field line, which represents a restoring force that helps to stabilize the "ballooning." This field line bending becomes more pronounced the more quickly a field line goes from bad to good curvature, thus, this mode is more stable at low  $q$ . A theoretically predicted limit on the ratio of the plasma pressure to the magnetic pressure,

$$\langle \beta \rangle \equiv 2\mu_0 \langle p \rangle / B_0^2, \quad (2.5)$$

which results from the "ballooning" mode of ideal (resistivity,  $\eta_r=0$ ) MHD implies that<sup>3</sup>

$$\langle \beta \rangle < \beta_{\text{crit}} = r\xi / (Rq_a^2) = 5\% , \quad (2.6)$$

where  $\xi$  is a parameter that depends on the shape of the plasma cross section and  $q_a$  is the  $q$  value at the plasma edge. Since the technologically attainable  $B_\phi$  over the ~2m minor radius envisioned for fusion reactors is 5-10T,  $\langle \beta \rangle = 5\%$  is barely adequate for significant power production ( $Q=5$ ).<sup>4</sup> Although the ballooning mode limit has not yet been completely verified by experiment, if it does exist, operating at higher fusion power densities, or at a lower, more economically desirable  $B_\phi$  value may be possible at lower  $q$ .

If the mode is of constant amplitude along a field line rather than localized in the bad curvature, then the field line bending mentioned above does not occur. In this case stability is determined by a competition of the effects of the displacement in the good curvature and bad curvature region. For  $q < 1$  the overall effect is destabilizing. A necessary condition for stability of this mode is given by the Mercier criteria for a  $R/r \gg 1$ , circular tokamak<sup>5</sup> as

$$\frac{1}{4} \left( \frac{q'(r)}{q(r)} \right)^2 + 2\mu_0 \frac{P'(r)}{rB_\phi^2} (1-q^2) > 0. \quad (2.7)$$

Since the shear of the magnetic field lines is stabilizing through

the first term in equation 2.7, this mode is expected to be important only near the magnetic axis.

For a given fusion power level to be sustained, either the power produced must be greater than the losses, or power input (ohmic heating, rf, neutral beams, etc.) must make up the difference. The ability of the tokamak to confine energy, which is characterized by the global parameter

$$\tau_E = 3/2 \langle nk(T_i + T_e) \rangle / (P_{\text{input}} + P_f), \quad (2.8)$$

then, may determine the engineering feasibility of attaining sustained fusion.

The ion energy confinement time is experimentally in good agreement with "neoclassical" theory<sup>6</sup> and so should scale as  $1/q^2$ .<sup>7</sup> The electron thermal conductivity, which is the dominant loss from most large tokamaks, is not completely understood; however, a theory based on resistive ballooning mode turbulence predicts that<sup>4,8</sup>

$$\tau_{Ee} \sim T_e / (q^2 \langle \beta \rangle R/r)^2. \quad (2.9)$$

Operating at low  $q$  may, thus, reduce the amount of power input needed to attain a given level of fusion power production.

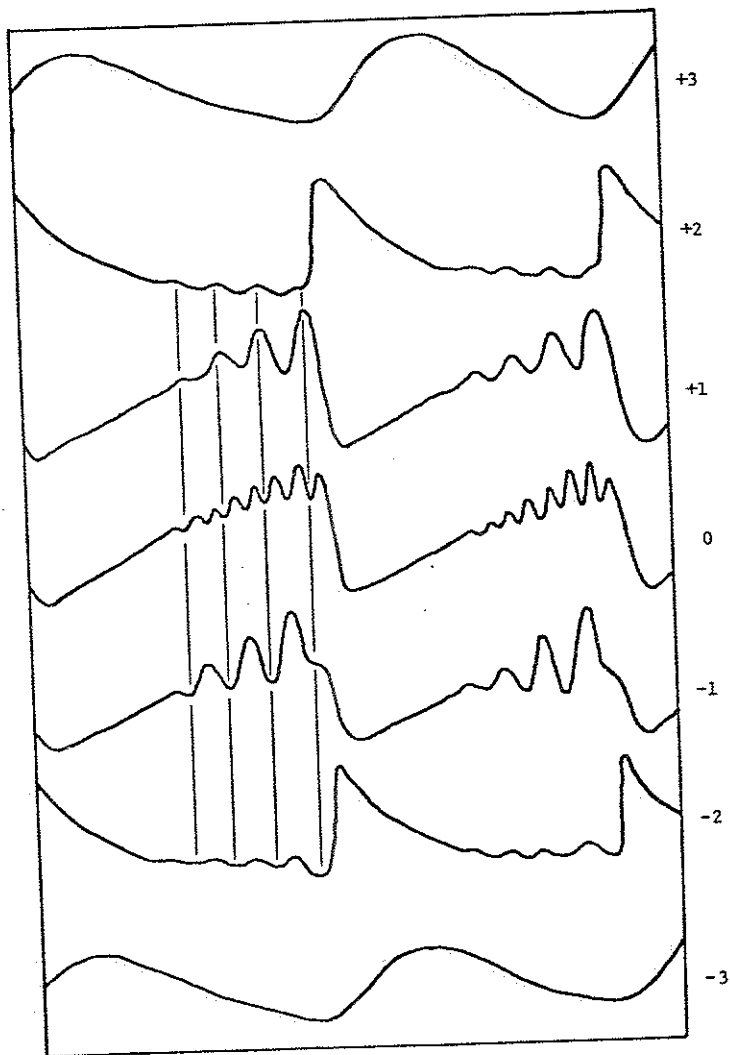
The instabilities which have set a lower limit on  $q$  are related to the simple kink mode of the linear  $z$ -pinch. The magnetic energy associated with large toroidal currents can drive modes which rearrange the magnetic field geometry in a destructive fashion. These modes are known as "disruptive instabilities" because of their often dramatic effect on the tokamak discharge.

### C. Disruptions Resulting from $m=n=1$ Helical Modes

In 1973 relaxation oscillations in the soft xray (0.5-10 keV) emissivity were first observed on the T-4 tokamak at the Kurchatov Institute in the USSR.<sup>9</sup> This was quickly followed by similar observations on the ST<sup>10</sup> and ATC<sup>11</sup> tokamaks at the Princeton Plasma Physics Laboratory. These "sawtooth" oscillations have subsequently been seen on all tokamaks, on many different diagnostics.

The general character of the soft xray (SXR) signals as they appear on a highly collimated, multichord, SXR array is shown schematically in figure 2-2. All the central chord signals show a slow rise followed by an essentially simultaneous rapid drop. Beyond a transition radius the sawteeth are inverted in character; each chord begins to rise simultaneously, and chords further from the plasma center peak progressively later. These "internal disruptions" occur nearly simultaneously at all toroidal angles.

FIG. 2-2. Schematic representation of typical sawtooth oscillations and  $m=n=1$  precursor oscillations as observed on a highly collimated SXR array. The numbers denote the position of each chord above (+) and below (-) the midplane. The central chord shows a frequency doubling of the precursor oscillation due to line averaging effects.



Accompanying the sawteeth are nearly sinusoidal precursor oscillations which grow in amplitude as the central chord signals ramp up. The structure of the precursor oscillation is found to be  $m=n=1$ ,<sup>10</sup> where the mode numbers are determined by assuming a phase factor  $\exp(i(m\theta - n\phi))$ . These are the mode numbers for a disturbance which has the same helical pitch as, i.e. is resonant with, the magnetic field lines on the  $q = 1$  magnetic surface.

The current density profile, and hence  $q$ , of tokamak plasmas is usually determined from Thomson scattering measurements of the electron temperature,  $T_e$ , and density,  $n_e$ , profile. From  $n_e$  and  $T_e$ , the resistivity profile is computed from the Spitzer relation<sup>12</sup> under the assumption that  $Z_{eff}$  (the effective ion charge state) is a constant. The current density profile can then be determined if the current density is assumed to be in equilibrium with respect to resistive diffusion, so that  $J_\phi \sim 1/\eta$ .<sup>10,11</sup> The  $q$  profile has also been determined by analyzing the drift orbits of injected neutral particles.<sup>13</sup> These techniques show that the inversion radius of the sawtooth oscillations is near the  $q=1$  surface. In addition, when no  $q=1$  surface exists in the plasma, the sawtooth oscillations are not present.<sup>14,15,16</sup>

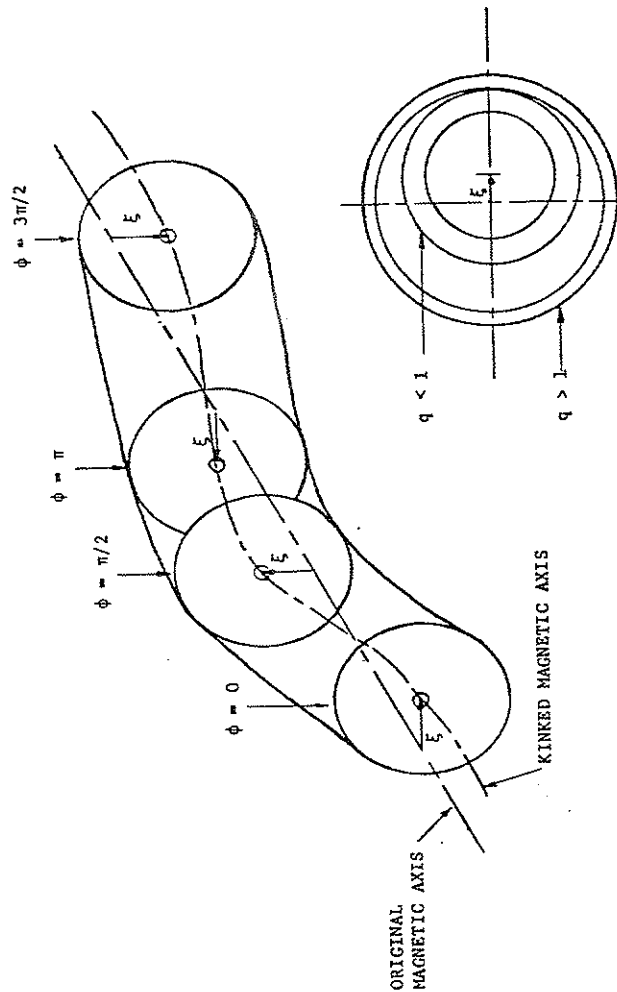
Although the SXR detectors are sensitive to electron density ( $\sim n_e^2$ ) and temperature ( $\sim T_e^3$ ), the TFR group has shown<sup>14</sup> that the internal disruption is predominantly a relaxation of  $T_e$ . On ATC, the central  $T_e$  from Thomson scattering saturated near the time the

sawtooth oscillation began, indicating that the internal disruptions affect the heat confinement.<sup>11</sup>

These facts suggest the following model for the internal disruption.<sup>17</sup> Prior to the disruption, the temperature of the region of the plasma within the  $q=1$  surface increases by  $\eta J^2$  heating, causing the central chord SXR signals to ramp up. At some point a catastrophe occurs which rapidly transports heat outward across the  $q=1$  surface causing the rapid rise of the external chord signals. Further from the plasma center, the rounded character of the inverted sawtooth is consistent with the arrival of a diffusive heat pulse.<sup>17,18</sup> B. Kadomtsev<sup>19</sup> provided a heuristic description of the rapid heat loss mechanism that is consistent with the  $q=1$  surface inversion point, and the growing  $m=n=1$  precursor oscillations.

In ideal MHD, a plasma with  $q < 1$  can lower its magnetic energy by kinking into a helix with  $m=n=1$ .<sup>20</sup> This can be envisioned as a rigid shift of the poloidal cross section in the direction of the displacement vector  $\xi$  which rotates with a helical pitch of  $m=n=1$  as shown in figure 2-3. Since the magnetic energy of outer region of the plasma with  $q > 1$  is raised by such a kinking, the displacement  $\xi$ , for the most unstable mode, must go to zero near the  $q=1$  surface. Thus, as the amplitude of the mode grows, magnetic flux is compressed between the  $q < 1$  and  $q > 1$  regions. This compression would saturate the ideal mode at a low amplitude.<sup>21</sup> The flux that is being compressed comes from the component of  $B$

FIG. 2-3.  $m=n=1$  kink. At each toroidal azimuth,  $\phi$ , the part of the plasma current column within the  $q=1$  surface is shifted radially outward without distortion of the surfaces. Since the region outside the  $q=1$  surface remains fixed, as the kink grows flux is compressed between the  $q < 1$  and  $q > 1$  regions.



perpendicular to the field at the  $q=1$  surface. For a finite resistivity plasma, this compressed flux (which can also be thought of as an image current generated in the  $q>1$  plasma by the outward motion of the kink) can resistively decay. Thus the kink can continue to grow as flux just within the  $q=1$  surface is resistively reconnected to flux just outside the  $q=1$  surface. This process changes the topology of the flux surfaces, creating a helical "magnetic island" as shown in figure 2-4. The reconnection continues until the current density is flattened within the original  $q=1$  surface, and  $q$  is raised above 1 everywhere. Toroidal axisymmetry is restored with the  $o$ -point of the island becoming the magnetic axis (figure 2-5). The magnetic energy liberated in this process is lost to thermal energy as the image current generated at the reconnection point (island  $x$ -point) is resistively dissipated, and also to the kinetic energy of the fluid flows.

Since magnetic surfaces within the hot  $q<1$  region are connected to surfaces in the cold  $q>1$  region, heat is rapidly transported outwards as the temperature equilibrates through the large thermal conductivity within a given surface; this produces the SXR sawtooth oscillations.

The time required for the instability to flip the magnetic topology,  $\tau_{\text{flip}}$ , can be estimated as follows.<sup>19,22,23</sup> In cylindrical geometry, the flux which is reconnected comes from the component of  $B$  perpendicular to a helical surface containing a magnetic field line on the  $q=1$  surface. For modes with long

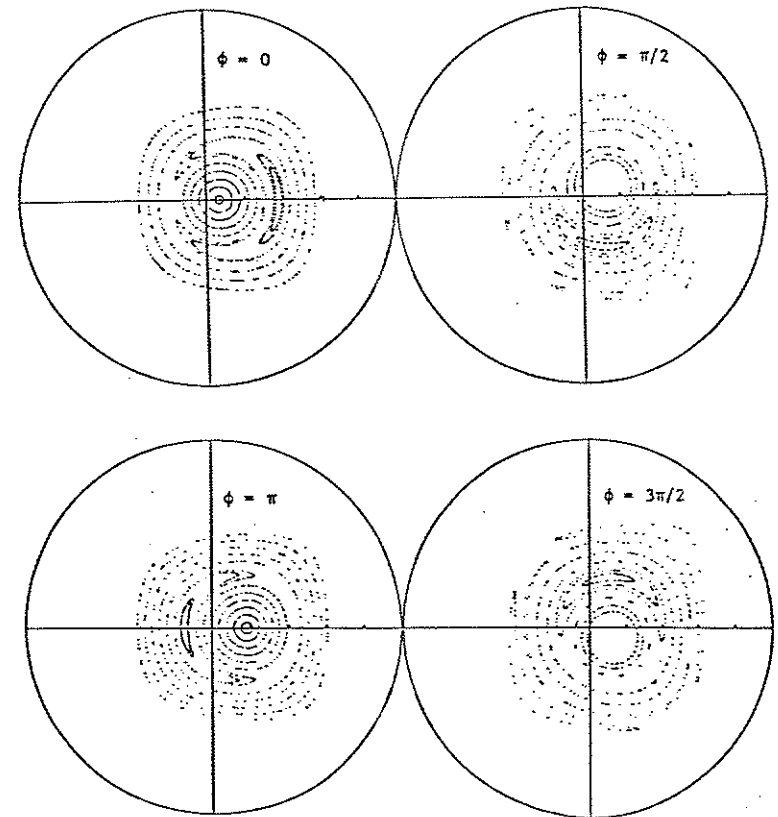
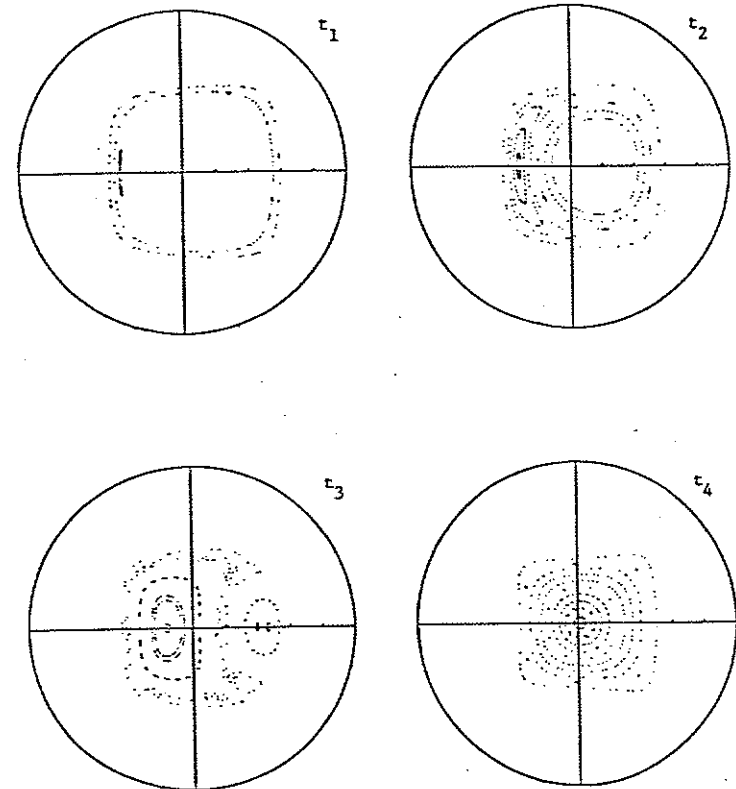


FIG. 2-4. Helical magnetic island generated by flux reconnection at the  $q=1$  surface.  $\phi$  denotes the toroidal azimuth.



FIG. 2-5. 1/1 disruption,  $t_1 < t_2 < t_3 < t_4$ . The  $m=n=1$  island continues to grow until all the flux within the original  $q=1$  surface is reconnected and the island o-point becomes the new axisymmetric magnetic axis.



toroidal compared to poloidal wave length, this helical flux,  $\chi$ , satisfies the magnetic diffusion equation,

$$\frac{\partial \chi}{\partial t} + \vec{v}_i \cdot \nabla \chi = -\eta J_z. \quad (2.10)$$

Since the flow pattern of the resistive mode is similar to the ideal mode, the radial flows go to zero near the reconnection point, so that at this point the flows are nearly purely poloidal, and so

$$\frac{\partial \chi}{\partial t} = -\eta J_s, \quad (2.11)$$

where  $J_s$  is the current generated at the reconnection point by the jump in the component of B that generates the helical flux,  $B^*$ ,

$$J_s = 2 \frac{B^*}{\delta}, \quad (2.12)$$

where  $\delta$  is the width of the reconnection layer. Outside the reconnection layer, the plasma behaves as in ideal MHD so

$$\frac{\partial \chi}{\partial t} = -v_r \frac{\partial \chi}{\partial r} = -v_r B^*. \quad (2.13)$$

Since the helical flux is essentially conserved during the reconnection, equating (2.11) and (2.13) gives

$$\tau_{\text{flip}} = \frac{a}{v_r} = \frac{\delta \tau_R}{a}, \quad (2.14)$$

where  $a$  is the minor radius, and  $\tau_R$  is the characteristic resistive diffusion time  $\equiv a^2/\eta$ . The width,  $\delta$ , is determined from the incompressibility condition  $\nabla \cdot \vec{v} = 0$ ,

$$v_r = \frac{\delta v_A^*}{a}, \quad (2.15)$$

where  $v_A^*$  is the Alfvén speed in the  $B^*$  field. Combining (2.13), (2.14), and (2.15) gives,

$$\tau_{\text{flip}} = (2\tau_A^* \tau_R)^{1/2}, \quad (2.16)$$

where  $\tau_A^*$  is the characteristic Alfvén time  $\equiv a/v_A^*$ . The disruption time arrived at in this way is close to the time the central chord SXR signals take to fall in the experiments. In the Tokapole II  $q=1$  plasmas, equation (2.16) gives  $\tau_{\text{flip}} = 24 \mu\text{s}$  which is close to the observed value.

The  $m=n=1$  precursor oscillations can be understood as being the image of a rotating, helically kinked structure. Diamagnetic frequencies, inferred from temperature and density profile measurements, are in agreement with the frequency of the  $m=n=1$ .<sup>10</sup>

Nonlinear resistive MHD codes have been in good qualitative agreement with Kadomtsev's picture. Codes including parallel transport have reproduced the drop in the central temperature and rise in the outer regions, and are in agreement with the time taken for the central chord SXR signal to fall.<sup>24</sup> These codes also

indicate that, in the nonlinear phase, the mode continues to grow exponentially at a growth rate determined from a linear picture, which is proportional to  $(dq/dr)^{2/3}$ .<sup>25</sup> This fact allows the growth rate of the island, and hence its size, to be computed as a function of time as ohmic heating peaks the current profile and so increases  $dq/dr$ .<sup>15,17</sup> The growth rate thus predicted is in good agreement with the growth rate of the precursor oscillations. Also, by assuming that the disruption occurs when the island width is equal to the minor radius, the sawtooth period can be computed and is in good agreement with that found in tokamaks operating in many different parameter regimes.<sup>15</sup>

The internal disruption restriction of  $q > 1$  represents an, as yet, unsurmounted obstacle to low  $q$  operation in tokamaks. The energy confinement of the plasma within the  $q=1$  surface before the disruption is as good as the remainder of the plasma,<sup>26</sup> but  $\tau_E(q<1)$  is poor when averaged over a sawtooth period. For tokamaks operating at high edge  $q$  values ( $>2$ ) the radius of the  $q=1$  surface is small compared to the minor radius; and so, the  $\tau_E$  of the overall plasma is relatively unaffected by the internal disruption. For tokamaks operating below  $q_a=2$ , the internal disruption can dominate the overall energy confinement.<sup>26</sup>

The internal disruption was suppressed in the Tosca tokamak by an  $m=n=1$  external winding. The required winding current was, however, nearly 20% of the plasma current.<sup>27</sup> Locally intense microwave heating of the plasma electrons on the T-10 tokamak

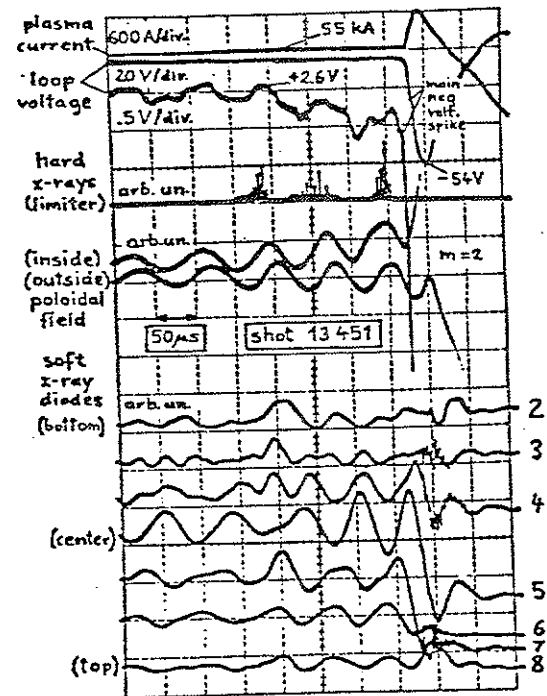
greatly extended the sawtooth period, presumably through some local profile change. The resistive  $m=n=1$  mode is stabilized by pressure effects at high  $\langle\beta\rangle$ ,<sup>28</sup> and so may not be a problem in reactor tokamaks.

#### D. Disruptions Resulting from $m>1$ Helical Modes

Perhaps the most dramatic problem to confront the tokamak reactor effort is the disruption. In its most destructive form, this mode can result in the loss of nearly the entire thermal energy content of the plasma and termination of the plasma current in a time less than 1 % of the discharge length. This can result in a power loss rate of 10 gigawatts for a reactor scale device.<sup>4</sup> In addition to the power deposition problems, the rapid current change can result in eddy current generation, which can produce severe mechanical stresses, or induce dangerously large voltages in poloidal flux supply circuitry. This mode also restricts the maximum plasma density that can be obtained by neutral gas puffing, and the maximum plasma current that can be obtained for a given toroidal field;<sup>29</sup> thus, it is a significant obstacle to the attainment of reactor plasmas in tokamaks.

The sequence of events involved in the disruptive instability in the Pulsator I tokamak,<sup>30</sup> which is typical of most devices, is shown in figure 2-6. Some time before the disruption, an  $m=2$   $n=1$  oscillation is observed on magnetic field pickup coils located at the wall. The  $m=2$  mode grows in amplitude as the time of the

FIG. 2-6. 2/1 disruption on Pulsator I.<sup>30</sup>  $m=2$  modes observed on magnetic pick up loops grow in amplitude before the disruption.  $m=1$  modes of the same frequency as the  $m=2$  are observed on the SXR array. As the coupling point of the  $m=1$  and  $m=2$  modes passes the limiter, bursts of hard x-rays from the limiter occur. At the time of the disruption the SXR signals drop, a large negative voltage spike is observed on the loop voltage, and the plasma current jumps upward. After the disruption the plasma current falls relatively slowly to 0.



disruption approaches and eventually impresses its frequency on an  $m=n=1$  mode observed on the soft xray emission from the plasma center. Roughly  $40 \mu\text{s}$  before the disruption (defined as the time at which the toroidal loop voltage falls by more than 30 volts in  $3 \mu\text{s}$ ) there is a burst of hard xrays (MeV). For the following  $40 \mu\text{s}$  the loop voltage drops by a few volts while the central chord soft xray signal falls to nearly zero. At the time of the main negative voltage spike there is a rapid increase in the loss of fast neutral particles (energy  $> T_e$ ) and a sudden increase in the plasma current, which then decays to zero over the next few hundred  $\mu\text{s}$ .

The plasma current is not always totally lost during the disruption. For so called "minor" disruptions, the effect on the plasma current is small and several of this type of disruption are often seen during a discharge.<sup>30,31</sup> The disruptions which terminate the discharge are referred to as "major" disruptions. In some discharges no disruption occurs, but a  $2/1$  mode of constant amplitude is seen through most of the discharge duration.<sup>31</sup>

Direct magnetic probe measurements of the current profile show that the central current falls rapidly during the time of the negative voltage spike while increasing somewhat on the outside.<sup>33,34</sup> This drop in the plasma inductance is the primary cause of the negative voltage spike. In most large tokamaks, the plasma is kept centered in the vacuum vessel by an externally applied vertical magnetic field. When the disruption greatly lowers the plasma inductance and pressure ( $\beta_{po1}$ ), the plasma

current generated forces, which push the plasma outwards in major radius, are reduced. The applied vertical magnetic field usually cannot respond on the time scale of the disruption, however, and so the plasma is thrown against the vessel inner wall.<sup>36</sup>

The appearance of a growing  $m=2$ ,  $n=1$  oscillation prior to the disruption is a feature common to most tokamaks.<sup>30-33</sup> Disruptions, however, are sometimes seen with a dominant  $3/1$  mode, or with no precursor oscillations.<sup>31</sup> The appearance of a coupled  $1/1$  mode is less generic however. In some cases the  $1/1$  mode seems to be related to the instability but does not have the frequency of the  $2/1$ ;<sup>31</sup> in others, a coupled  $3/2$  mode is observed.<sup>32,33</sup> The  $q=2$  surface (at which a  $2/1$  mode is resonant), as determined by magnetic field and Thompson scattering measurements, is further implicated in the disruption by the fact that the current and soft xray emissivity drop is sometimes observed to propagate inwards from this surface.<sup>31,34</sup> Resistive MHD theory incorporating nonlinear mode coupling has been very successful in accounting quantitatively for the features of the disruption.

While the toroidal  $m=n=1$  mode is marginally unstable ( $\gamma=0$ ) in ideal MHD, the  $m>2$  modes are stable.<sup>37</sup> This is a result of the fact that the  $m=1$  mode is a rigid displacement of the plasma cross section while the  $m>2$  modes distort this cross section. This tends to localize the perturbation for  $m>2$  to the region near the resonant surface, and produces a tearing mode which is weaker in the sense that its exponential growth rate is closer to a resistive

time scale  $\gamma_{m>1} \sim \tau_R^{-3/5}$ ,<sup>38</sup> while  $\gamma_{m=1} \sim \tau_R^{-1/3}$ .<sup>37</sup> Because of the weakness of the  $m>2$  tearing mode, forces due to second order currents are able to change the growth from exponential to linear in time at a rate on a resistive time scale.<sup>39</sup> Even this slow process, which can be comparable to the discharge duration, can be halted by a self stabilization through quasilinear flattening of the current density profiles.<sup>40</sup> The saturated island width is determined by the shape of the equilibrium current density and resistivity profile, and generally is larger when the current density gradient is steepest. A typical saturated island width for the 2/1 mode is 10% of the minor radius. The saturation of a 2/1 island explains the observation of discharges with continuous 2/1 fluctuations and no disruption.

B. Carreras and others<sup>41,42,43</sup> have shown that the nonlinear interaction of the 2/1 with other modes can lead to destabilization of many tearing modes. This destabilization proceeds both through quasilinear modification of the equilibrium current density profile, and through direct nonlinear mode coupling. The modes primarily studied by Carreras et al. were the 2/1 and 3/2. Both of these modes were linearly unstable for the current density profiles employed. The quasilinear perturbation of equilibrium by the 2/1 and 3/2 destabilized the 5/3, which in turn coupled to the 3/2, tremendously increasing its growth rate and also destabilizing the 2/1. This process produced large perturbations of incommensurate helicity occupying the same region of the plasma.

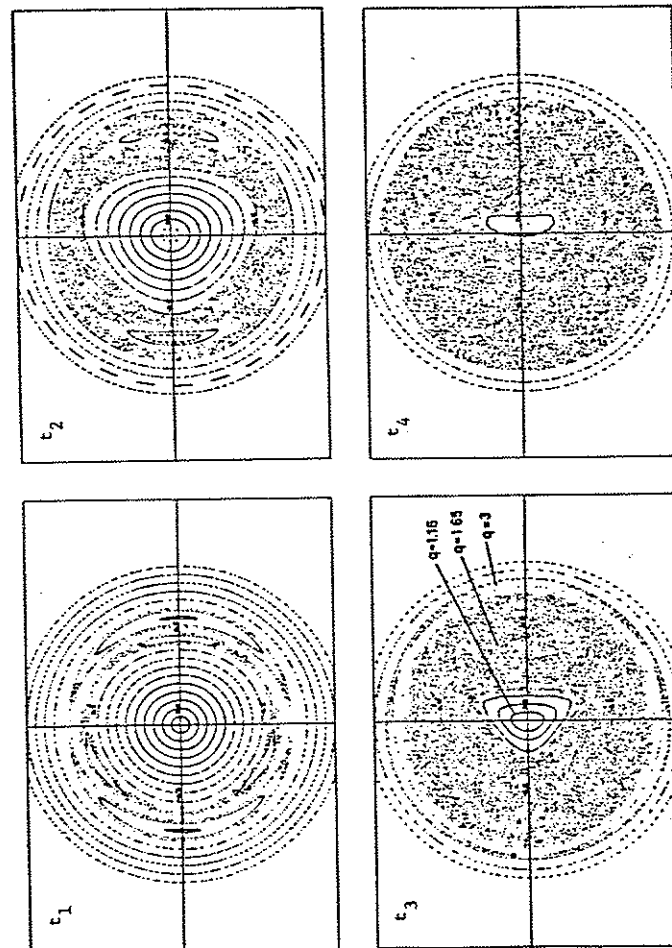
Because of the 3-D nature of the magnetic geometry, this interaction produces a region of ergodic field rather than magnetic surfaces as shown in figure 2-7. The exact extent of the ergodic region depends on the modes involved and the current density profile.

This model is consistent with the experimental results which show that the disruption is initiated on the inside of the  $q=2$  surface. The experimental data seems to be more indicative of 1/1, 2/1 coupling. However, the model also predicts that a 1/1 mode will be driven by coupling of the 2/1 and 3/2.

In experiments on JIPP T-II the 3/2 mode was identified. The workers on this experiment were able to prevent the occurrence of disruptive instability by controlled gas puffing and plasma current programming.<sup>33</sup> E.R. Hicks et al.<sup>44</sup> used the current density profiles obtained for this experiment as initial conditions for code runs. They were able to predict the duration and size of the negative voltage spike observed on the discharges that did disrupt. For those discharges which did not disrupt, the mode interaction was found to be small and the magnetic islands remained saturated. The code accurately predicted the level of magnetic field fluctuation observed.

The 2/1 mode is important in the disruption because the  $q=2$  surface lies near the edge of the plasma in a region of large current density gradient. As already mentioned, the magnetic island size generally increases with the equilibrium current

FIG. 2-7. Production of a large ergodic field region through the interaction of the 2/1 and 3/2 modes. At  $t_1$  the 2/1 and 3/2 island are visible and some ergodicity is seen in the outer island surfaces; from  $t_2$  to  $t_4$  the ergodicity spreads until it covers nearly the entire plasma column.



density gradient at the mode rational surface. Since the size of the 2/1 island determines the strength of its interaction with other modes, the current density gradient at the  $q=2$  surface determines if a disruption will occur. Increasing the plasma density by gas puffing from the wall increases the impurity input from the wall and subsequently cools the edge of the plasma. Cooling of the edge plasma decreases the current density in this region and, thus, increases the current density gradient near the  $q=2$  surface. Increasing the plasma density by pellet injection may avoid this effect and allow the disruptive density limit to be surpassed. Improving wall cleanliness, either by discharge cleaning or gettering, can decrease the impurity input that results from increased recycling with heavy gas puffing. This technique has allowed higher density operation without disruption in several tokamaks.<sup>33,45</sup> The disruptive current limit can be understood on the same grounds. As  $I_p$  is increased, the  $q=2$  surface moves closer to the edge where the current density is larger producing a larger 2/1 island.

Control of the disruption centers on control of the 2/1 mode. Attempts to actively suppress the disruption involve either flattening the current density profile in the region near the  $q=2$  surface, or attacking the 2/1 perturbation directly by  $dc$ <sup>27,30</sup> or feedback controlled<sup>46</sup> external helical windings. Although 2/1 helical windings have been somewhat successful, on larger tokamaks the helical coils require prohibitively large currents, and the

helical windings can add significantly to the complexity of the device. A related technique uses a nonresonant winding to destroy the magnetic surfaces, and thus flatten the temperature and current density gradient in the neighborhood of  $q=2$ .<sup>47</sup>

Most tokamaks today use  $I_p$  and gas puff programing to control the current density profile at the  $q=2$  surface.<sup>33,48</sup> Because the plasma is a good conductor, attempting to rapidly increase its current will generate skin currents which flatten the current density near the plasma edge, and counteract the peaking effect of impurities produced by gas puffing. Using this technique many large tokamaks are able to operate routinely below  $q_{edge}=2.5$ .

#### E. $q < 2$ Tokamaks

All tokamaks which have operated with  $q < 2$  have employed a conducting wall near the plasma surface.<sup>26,27,49</sup> This wall acts to stabilize the 2/1 mode when it is near the plasma edge. Once  $q_{edge} < 2$ , no 2/1 disruptions are observed; usually a positive voltage spike is observed near the transition to  $q < 2$ . The energy confinement time of DIVA,<sup>26</sup> when operated below  $q_{edge}=2$ , is not significantly lower than for  $q_{edge} > 2$  operation. As  $q$  is lowered further, the energy loss becomes dominated by internal disruptions as the  $q=1$  surface moves near the plasma boundary. During the sawtooth ramp up,  $\tau_E$  is a factor of 4 better than the average value. Below  $q_{edge}=1.3$ ,  $\tau_E$  drops by a factor of 100, and a saturated  $m=n=1$  kink is observed. The authors attributed this drop



to the close proximity of the  $q=1$  surface to the plasma boundary. In the LQT (Low  $q$  Tokamak) at Culham laboratory,<sup>49</sup> as  $q$  approaches 1, positive voltage spikes appear and a rapid "pump out" of plasma density occurs. Sawtooth oscillations occur, accompanied by predominantly  $m=n=1$  oscillations observed on magnetic loops at the plasma edge. These authors did not attribute the loss of confinement directly to internal disruptions. In both experiments the current could not be raised beyond the point at which the loss in confinement occurred.

The  $q < 2$  regime was reached in the TORIUT-4 tokamak with the conducting boundary placed as far out as 1.5 times the plasma minor radius. This was made possible through the use of an external 3/1 winding that ergodized the 2/1 island during the current build up phase of the discharge.<sup>47</sup>

References for Chapter 2

- <sup>1</sup>S.W. Cousins and A.A. Ware, Proc. Phys. Soc. (London), A64, 159 (1951).
- <sup>2</sup>R.W. Conn, "Magnetic Fusion Reactors," Fusion, Academic Press, 1, 194 (1981).
- <sup>3</sup>A.M. Todd, M.S. Chance, J.M. Green, R.C. Grimm, J.L. Johnson, and J. Manickam, Phys. Rev. Letters, 38, 826 (1977).
- <sup>4</sup>Y.-K.M. Peng, et al., in Plasma Physics and Controlled Thermonuclear Fusion Research (Proc. 9th Int. Conf. Baltimore 1982), 1, IAEA Vienna (1983).
- <sup>5</sup>V.O. Shafranov and E.I. Yurchenko, Sov. Phys. JETP, 26, 682 (1968).
- <sup>6</sup>I.A. Artsimovich, Nucl. Fusion, 12, 215 (1972).
- <sup>7</sup>F.L. Hinton and R.D. Hazeltine, Reviews of Modern Phys., 48, 239 (1976).
- <sup>8</sup>D.W. Swain, et al., Nucl. Fusion, 21, 1409 (1981).
- <sup>9</sup>V.A. Vershkov, C.E. Lisenko, I.B. Semenov, and A.T. Scherbac, PPPL Report MATT-TRANS 112 (1974).
- <sup>10</sup>S. von Goeler, W. Stodiek, and N. Sauthoff, Phys. Rev. Letters, 11, 1201 (1974).
- <sup>11</sup>R.R. Smith, Nucl. Fusion, 16, 1053 (1976).
- <sup>12</sup>L. Spitzer, Physics of Fully Ionized Gases, John Wiley & Sons, (1962).
- <sup>13</sup>R.J. Goldston, PPPL Report - 1432, (1978).
- <sup>14</sup>TFR Group, Plasma Physics, 19, 349 (1977).
- <sup>15</sup>K. McGuire, D. Robinson, Nucl. Fusion, 19 505 (1979).
- <sup>16</sup>S.J. Fielding, et al., Nucl. Fusion, 17, 1382 (1977).
- <sup>17</sup>G.L. Jahns, M. Soler, B.V. Waddell, J.D. Callen, H.R. Hicks, Nucl. Fusion, 18, 609 (1978).

- 18 J.D. Callen and G.L. Jahns, Phys. Rev. Letters, 28, 491 (1977).
- 19 B.B. Kadomtsev, Sov. J. Plasma Phys., 1, 389 (1975).
- 20 V. Shafranov, Sov. Phys. Tech. Phys., 15, 175 (1970).
- 21 M.N. Rosenbluth, R.Y. Dagazian, P.H. Rutherford, Phys. Fluids, 18, 1894 (1973).
- 22 W. Park, D.A. Monticello, and R.B. White, Phys. Fluids, 27, 137 (1984).
- 23 R.B. White, D.A. Monticello, M.N. Rosenbluth, and B.V. Waddell. PPPL Report-1282 (1976).
- 24 A. Sykes and J.A. Wesson, Phys. Rev. Letters, 37, 140 (1976).
- 25 B.V. Waddell, M.N. Rosenbluth, D.A. Monticello, R.B. White, Nucl. Fusion, 16, 528 (1976).
- 26 DIVA Group, Nucl. Fusion, 20, 271 (1980).
- 27 J.J. Ellis, K. McGuire, R. Peacock, D.C. Robinson, I. Stares, in Plasma Physics and Controlled Thermonuclear Fusion Research (Proc. 8th Int. Conf. Brussels, 1980), 1, IAEA, Vienna, 731 (1981).
- 28 M. Azumi, Japan Atomic Energy Research Institute Rep. JAERI-M 9787 (1981).
- 29 Equipe TFR, Nucl. Fusion, 17, 1283 (1977).
- 30 F. Karger, et al., in Plasma Physics and Controlled Thermonuclear Fusion Research (Proc. 6th Int. Conf. Berchtesgarden, 1976), 1, IAEA, Vienna 267 (1976).
- 31 N.R. Sauthoff, S. von Goeler, W. Stodiek, Nucl. Fusion, 18, 1445 (1978).
- 32 D.B. Albert and A.H. Morton, Nucl. Fusion, 17, 863 (1977).
- 33 K. Tol. et al., Nucl. Fusion, 19, 1643 (1979).
- 34 I.H. Hutchinson, Phys. Rev. Letters, 37, 338 (1976).
- 35 K. Makishima, T. Tominaga, H. Tohyama, and S. Yoshikawa, Phys. Rev. Letters, 36, 142 (1976).
- 36 M. Okabayashi, H. Maeda, H. Takahasi, M. Reusch, PPPL Report - 1707 (1980).

- 37 P.H. Rutherford, in Physics of Plasma Close to Thermonuclear Conditions (Proc. of the Cours., Varenna 1979), 1, Commission of the European Communities, Brussels, 129 (1979).
- 38 H. Furth, J. Killeen and M.N. Rosenbluth, 6, 459 (1963).
- 39 P.H. Rutherford, Phys. Fluids, 16, 1903 (1973).
- 40 R.B. White, D. Monticello, M.N. Rosenbluth, B.V. Waddell, PPPL Report MATT-1267 (1976).
- 41 H.R. Hicks, B. Carreras, J.A. Holmes, B.V. Waddell, ORNL Report TM-6096 (1977).
- 42 B. Carreras, B.V. Waddell, H.R. Hicks, ORNL Report TM-6175 (1979).
- 43 R. Izzo et al., Phys. Fluids, 26, 2240 (1983).
- 44 H.R. Hicks, J.A. Holmes, V.E. Lynch, B.A. Carreras, ORNL Report TM-7733 (1981).
- 45 S. Fielding, et al., Nucl. Fusion, 17, 1382 (1977).
- 46 V.V. Arsenin and V.A. Chuyanov, Sov. Phys. Usp., 20, 736 (1977).
- 47 Z. Yoshida, et al., in Plasma Physics and Controlled Thermonuclear Fusion Research (Proc. 9th Int. Conf. Baltimore 1982), 3, 273 (1982).
- 48 D.O. Overskei, et al., Journal of Magnetism and Magnetic Materials, 11, 363 (1979).
- 49 T. Edlington, J.L. Luxon, T.N. Todd, D.C. Robinson, in Plasma Physics and Controlled Thermonuclear Fusion Research (Proc. 9th Int. Conf. Baltimore 1982), 3, 241 (1982).

## CHAPTER 3

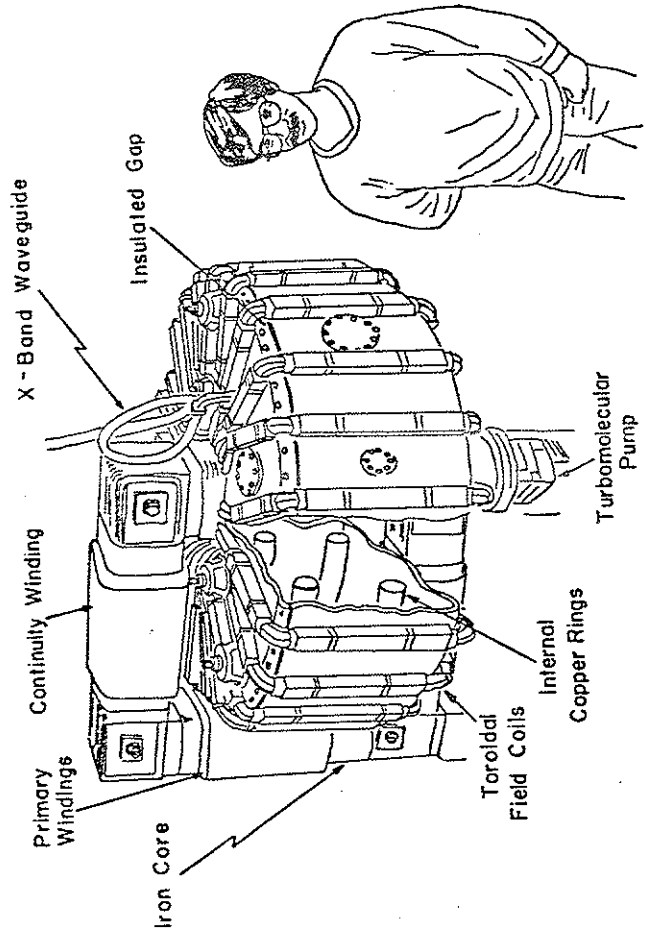
APPARATUS AND DIAGNOSTICSA. Tokapole II

These experiments were carried out in Tokapole II<sup>1</sup> (figure 3-1), a poloidal divertor tokamak, which has been in operation at the University of Wisconsin-Madison physics department since March 1978. An excellent description of the engineering and physics considerations involved in the design of the device can be found in references 2 and 3.

The vacuum vessel consists of a 44 cm square cross section torus, with a major radius of 50 cm (figure 3-2). The vessel walls are 3 cm thick aluminum, with insulated breaks both poloidally and toroidally to allow the magnetic fields to enter. Within the vessel are four, solid copper, 5 cm cross sectional diameter, toroidal rings, which are each supported at three points by beryllium copper rods. The rings can be moved vertically  $\pm 5$  mm to position the plasma.

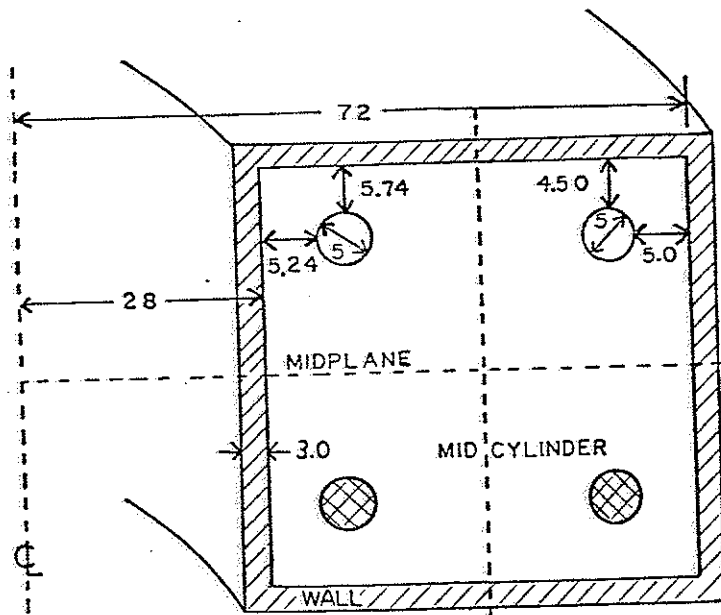
The toroidal current in the rings and plasma is driven inductively through a 40:1 turns ratio transformer core, by a 7.4 mF, 5 kV capacitor bank. The current in the rings, which is typically a total of 200 kA, produces an octupole pattern of poloidal flux contours in the absence of plasma current, as shown in figure 3-3a. The position of the rings within the conducting

FIG. 3-1. Wisconsin Tokapole II poloidal divertor tokamak and typical experimenter.



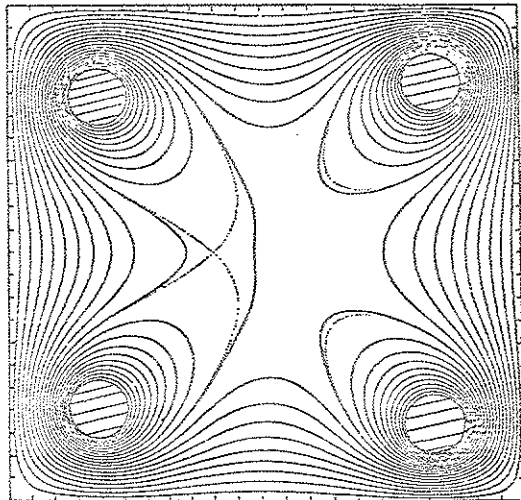
TOKAPOLE II

FIG. 3-2. Cross section of Tokapole II vacuum vessel. The divertor rings are shown in the position used for most of the experiments in this thesis.

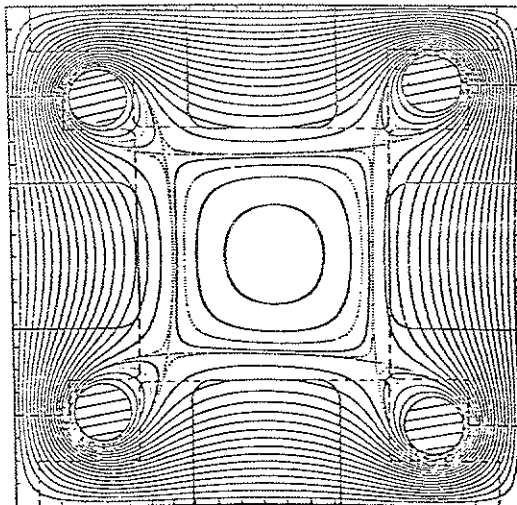


DIMENSIONS IN cm

FIG. 3-3. Contours of constant poloidal magnetic flux for (a) with no plasma current and (b) with plasma current. The insertable baffle plates are shown in their current shapes as a solid line, and by a dashed line for their original shapes.



(a)



(b)

2 cm

wall determines that about half the total flux encircles all four rings (the "common flux") and the remainder encircles only a particular hoop (the "private flux"). Because of this flux division, the vacuum electric field at the machine center, which drives the plasma current, is about half what it is at the machine wall.

The contours of poloidal flux with toroidal plasma current present are shown in figure 3-3b. For these experiments, the plasma current was varied from 8 to 50 kA. A distinctive feature of the poloidal divertor magnetic topology of poloidal divertors are the "separatrices:" flux contours which contain saddle points ("x-points") at which the poloidal field vanishes. The separatrices are boundaries between topologically distinct flux regions.

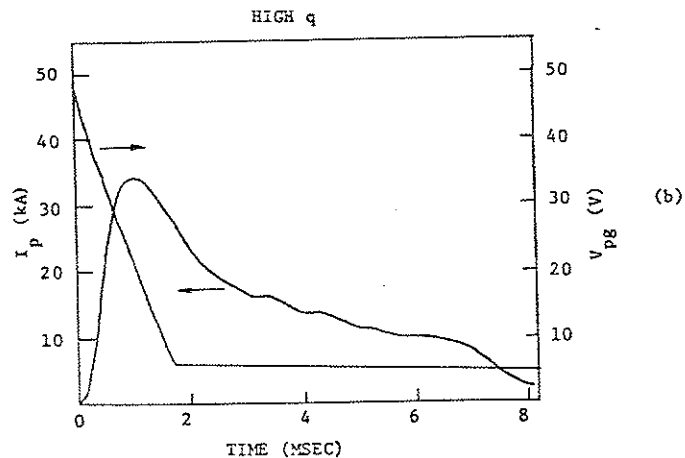
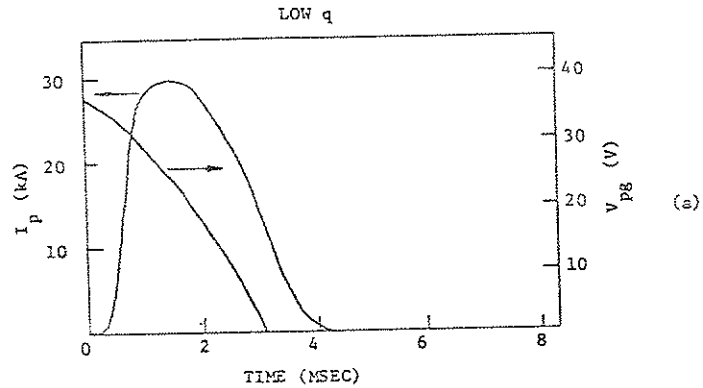
Throughout the remainder of this thesis, unless otherwise specified, "inside the separatrix" will refer to the poloidal flux which does not encircle any of the divertor coils, and "outside the separatrix" will refer to the remainder of flux space. Also shown in figure 3-3b are the four, thin stainless steel, baffle plates that can be used to restrict the current to the region within the separatrix.

The Tokapole II poloidal field geometry is similar to the Doublet III<sup>4</sup> (when run in expanded boundary mode), ASDEX<sup>5</sup>, PDX<sup>6</sup>, and DIVA<sup>7</sup> tokamaks, and is termed a poloidal divertor configuration since flux lines outside the separatrix are diverted from a

circular path to one which encircles the rings. A poloidal divertor configuration is important since the plasma wall interaction can be isolated to structures inserted into the plasma in the gap between the rings and the wall, which facilitates control of impurity influx.<sup>5,6,7</sup> Also the presence of the separatrix appears to allow the achievement of an enhanced confinement regime in neutral beam heated tokamaks.<sup>8</sup> Tokapole II is the only divertor tokamak that routinely runs with substantial hot plasma and plasma current outside the separatrix. In other poloidal divertor tokamaks the flux lines outside the separatrix intersect a limiter plate; this makes the gradients of pressure and current density large near the separatrix. In Tokapole II, substantial plasma current and pressure exist outside the separatrix so that the current density gradient in this region can be small. Since these gradients are important in determining tearing mode stability, disruptions in Tokapole II could behave much differently than in other poloidal divertor machines.

Two types of transformer primary waveforms were used in this experiment. For the "low q" case (figure 3-4a) the capacitor bank is connected directly to the transformer primary producing a single turn secondary voltage, " $V_{pg}$ ," of essentially a quarter sine wave; when  $V_{pg}$  reaches zero, a diode across the primary clamps the voltage. For the "high q" case (figure 3-4b) a resistor is added to the primary circuit which damps the main capacitor bank voltage

FIG. 3-4. Typical toroidal plasma current,  $I_p$ , and poloidal gap voltage,  $V_{pg}$ , for (a) a low q case and (b) a high q case.



waveform; a 0.96 F, 450 V capacitor bank added to the diode circuit clamps  $V_{pg}$  capacitor bank to 5 V capacitor bank.

The toroidal field, " $B_\phi$ ," is produced by 96 poloidal windings driven by a 52 mF, 5 kV capacitor bank; when the bank voltage reaches zero it is clamped by an ignitron across the windings. The  $B_\phi$  capacitor bank is usually triggered 6 ms before the bank which drives the ring and plasma currents; thus,  $B_\phi$  remains fairly constant over the course of the discharge (figure 3-5).  $B_\phi$  at the machine center ranged from 1.5 to 6 kG for these experiments.

Hydrogen gas is puffed into the vacuum vessel by a piezoelectric valve 16.66 ms before  $V_{pg}$  is fired. For the low q experiments, 50 watts of continuous S-band microwaves are used to preionize the plasma. The line averaged density as measured by a 70 GHz interferometer for this case is shown in figure 3-6a. For the high q experiments, in addition to the initial gas puff, a feedback or manually controlled gas bleed maintains the density (figure 3-6b). For the high q case a 500  $\mu$ s pulse of 8 kW K-band preionization is used.

Typical plasma parameters are  $T_e = 100\text{eV}$ ,  $T_i = 40\text{eV}$ ,  $n_e = 10^{13}\text{cm}^{-3}$ ,  $\tau_E = 50\mu\text{s}(\text{low } q)$  to  $600\mu\text{s}(\text{high } q)$ , and  $\langle\beta\rangle = 0.1\%$ .

#### B. Magnetic Probe Measurements of $q$ and $\psi$

The poloidal magnetic field was measured with magnetic probes. These probes consist of two 1 cm long coils of about 50 turns, wound on top of each other, and encased in 1/8 inch diameter, 0.010



FIG. 3-5. Toroidal magnetic field. The values shown are typical of a high  $q$  case.

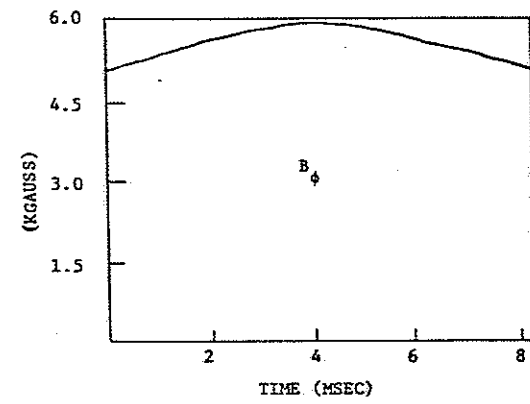
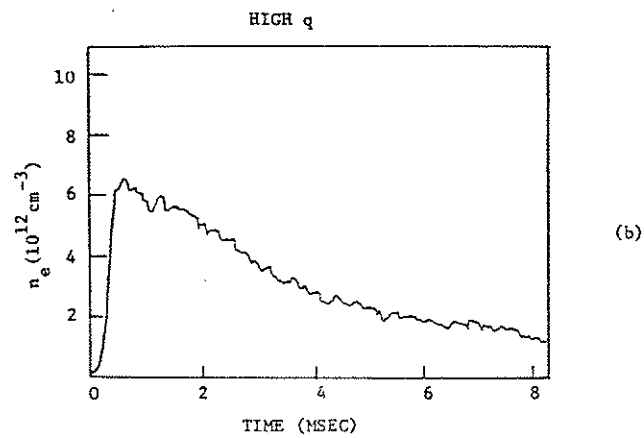
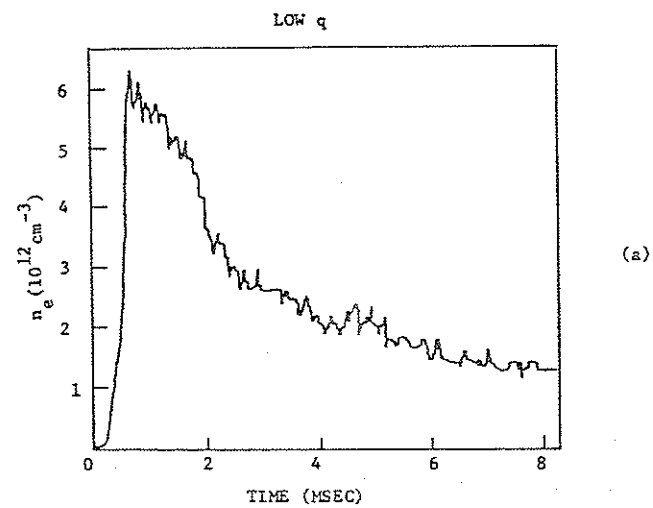


FIG. 3-6. Typical line averaged electron density for (a) a low  $q$  case and (b) a high  $q$  case.



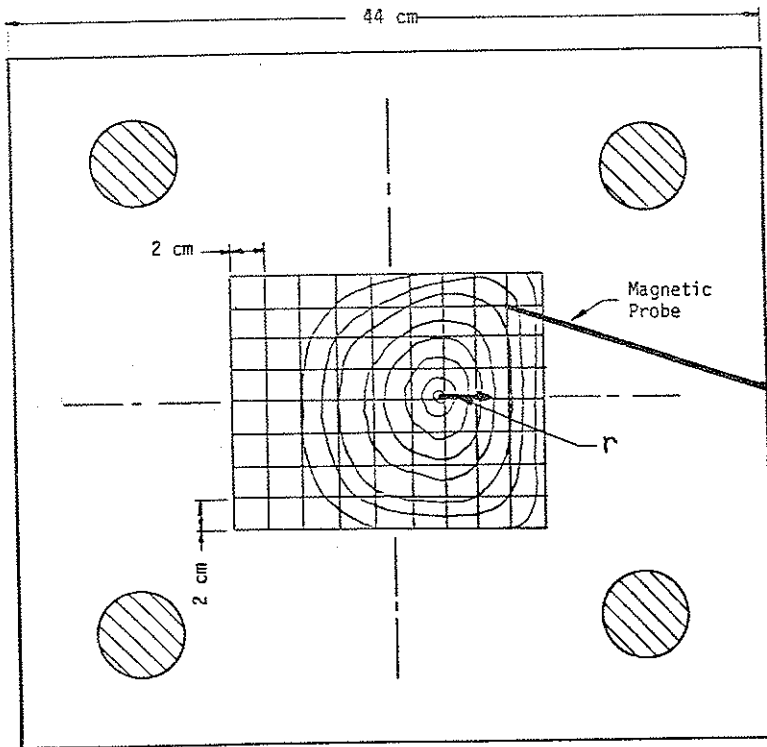
inch wall stainless steel tubes. Details of the probe design can be found in reference 9. The coils are oriented to detect the components of  $B_{pol}$  perpendicular and parallel to the probe axis. The frequency response of the probe was measured to better than 100 kHz.

The probe signals are first run through passive integrators with time constants of about 20 ms, and then digitized and stored by computer. Since slight misalignments of the probe about its axis would cause large  $B_\phi$  pickup, the probe signal from a pulse with vacuum toroidal field only is used as a baseline. The perturbation on the vacuum toroidal field that results from poloidal plasma currents was found to be  $< 5\%$  of  $B_\phi$ , and therefore, its effect on the baseline signal and in the computations described below were ignored. The data grid used for the magnetic probe measurements is shown in figure 3-7.

The poloidal magnetic field data was analysed, assuming toroidal symmetry, to produce plots of poloidal magnetic flux,  $\psi$ , profiles of the flux surface averaged  $q$ , and profiles of the current density averaged over an area between two flux surfaces.<sup>10</sup> The magnetic axis, at which  $B_{pol} = 0$ , was found by first searching the data for the minimum  $B_{pol}^2$  point, and then interpolating from a polynomial fit to the surrounding data points. The flux surfaces were then generated as contours of the function

$$\psi(r, \theta) = 2\pi \int_0^r dr' (R_0 + r' \cos \theta) B \times r', \quad (3.1)$$

FIG. 3-7. Typical data grid for magnetic probe measurements of  $\psi$  and  $q$ . The minor radius,  $r$ , used in the plots of  $q$  is defined as the distance from the magnetic axis to a given  $\psi$  surface in the direction of a major radius vector.



where  $R_0$  is the major radius to the midcylinder,  $r$  the radius from the magnetic axis,  $\vec{B}$  is a polynomial fit to the data, and  $\hat{r}$  is a unit vector along  $r$ . Once the locus of points for the  $k$ -th flux surface  $\{r(k, \theta)\}$  are known, the flux surface averaged  $q$ ,  $q(k)$ , the current within a surface,  $I(k)$ , and the area within a surface,  $A(k)$ , are computed from

$$q(k) = \frac{1}{2\pi} \int \frac{r B_{tor}}{R B_{pol}} d\theta, \quad (3.2a)$$

$$\{r(k, \theta)\}$$

$$I(k) = \frac{1}{\mu_0} \int B_{pol} d\theta, \quad (3.2b)$$

$$\{r(k, \theta)\}$$

$$A(k) = \int r^2 d\theta. \quad (3.2c)$$

$$\{r(k, \theta)\}$$

The average current density between two flux surfaces is then computed as

$$j(k) = [I(k+1) - I(k)] / [A(k+1) - A(k)]. \quad (3.3)$$

### C. Soft X-ray Measurements

As mentioned in chapter 1, disruptive instabilities are associated with rearrangement or destruction of the magnetic surfaces within the plasma. Because of the high thermal

conductivity parallel to the magnetic field, the temperature equilibrates rapidly over the new magnetic surfaces or ergodic regions created by the instability.

Radiation in the SXR in plasmas comes primarily from sources with emissivity that is strongly dependent on  $T_e$ ,<sup>11</sup> so that even though a collimated detector averages over a chord, the detected signal comes primarily from the hottest point along the chord. Detector arrays viewing several chords in a poloidal plane can, thus, provide a qualitative image of the changing magnetic topology. Very often plasmas rotate rapidly compared to the growth of the instabilities; this allows tomographic techniques to be applied, and the number of chords needed to invert the signals is reduced.<sup>12</sup>

The central temperature in Tokapole II is approximately 100 eV.<sup>13</sup> At this temperature, SXR radiation comes primarily from line radiation. For a Maxwellian electron distribution bremsstrahlung is expected to dominate recombination only when  $kT_e > 35.4Z_{\text{eff}}^2$ .<sup>14</sup> The right hand side of the preceding expression is about 220 eV in Tokapole II so that recombination radiation is expected to dominate bremsstrahlung. Dielectronic recombination, which is important in the outer shells of heavy impurities where the energy levels are closely spaced, is not expected to be significant, since the photons emitted would be below the detectable energy limit. Groebner and Dexter<sup>15</sup> determined from impurity doping experiments that radiation from light impurities

(eg. carbon or oxygen) accounted for < 20 % of the SXR signal. At 100 eV the emission from metals is predominately line radiation.<sup>16</sup> The intensity of this radiation is expected to vary approximately as<sup>16</sup>

$$I \sim n_e n_i e^{-E/T_e}, \quad (3.4)$$

where  $n_e$  is the electron density,  $n_i$  is the ion density in the  $i$ 'th charge state, and  $E$  is the photon energy.

Surface barrier diodes with polypropylene filters are used for SXR detectors on Tokapole II. This detector filter combination allows sensitivity down to photon energies of  $\approx 60$  eV. The choice of surface barrier diodes was optimum because of their extremely thin "dead" (undepleted) P layer window.<sup>17</sup> The filters were made by stretching polypropylene sheet. 800 nm of polypropylene has a transmittance of 1% at 80 eV and 25% at 120 eV. In practice, if the filters were too thin (or had holes), the detector's enhanced sensitivity to VUV produced an obvious  $n_e$  dependence in the signals; if the filters were too thick, the signal dropped to an unusably low level.

The temperature dependence of the composite detector depends on the filter, dead layer, and gold contact layer thickness as well as the temperature dependence of the source. In an impurity doping experiment, in which another parameter of known  $T_e$  scaling was compared with the SXR signal, Groebner and Dexter<sup>15</sup> found that

$$\text{SXR} \sim e^{-280/T_e}.$$

(3.5)

The signal is also expected to be proportional to  $n_e$  and  $n_i$ .

The detectors are always operated in "current mode" in which the output is simply terminated with a 5-100 k $\Omega$  resistor and run into an amplifier. No bias voltage is normally applied to the diodes, and they are operated at room temperature.

The detector array consists of seven detectors located on the outer wall and several other detectors which can be placed on any swivel port where they can be tilted  $\pm 25^\circ$  (figure 3-8). The toroidal location of the side array, and of available swivel ports is shown in figure 3-9. The side array detectors viewed a spot of  $\approx 3$ cm diameter on the midcylinder, while the tiltable detectors had a spot size of  $\approx 0.5$ cm. The frequency response is limited by the large diode capacitance  $\approx 200$  pF, due to the narrow depleted region for the unbiased diodes. Typically a frequency response of a few hundred kHz could be achieved on the central chord signals, while the response of the edge chord signals was never greater than 100 kHz. The low frequency response (or equivalently signal to noise ratio) of detectors 1 and 7 (and sometimes 2 and 6) made them unusable for fluctuation studies.

#### D. Electric Field Probes

FIG. 3-8. SXR chords. Seven fixed detectors are available on the side array, and other detectors can be placed on swivel ports which can be tilted over the range shown.

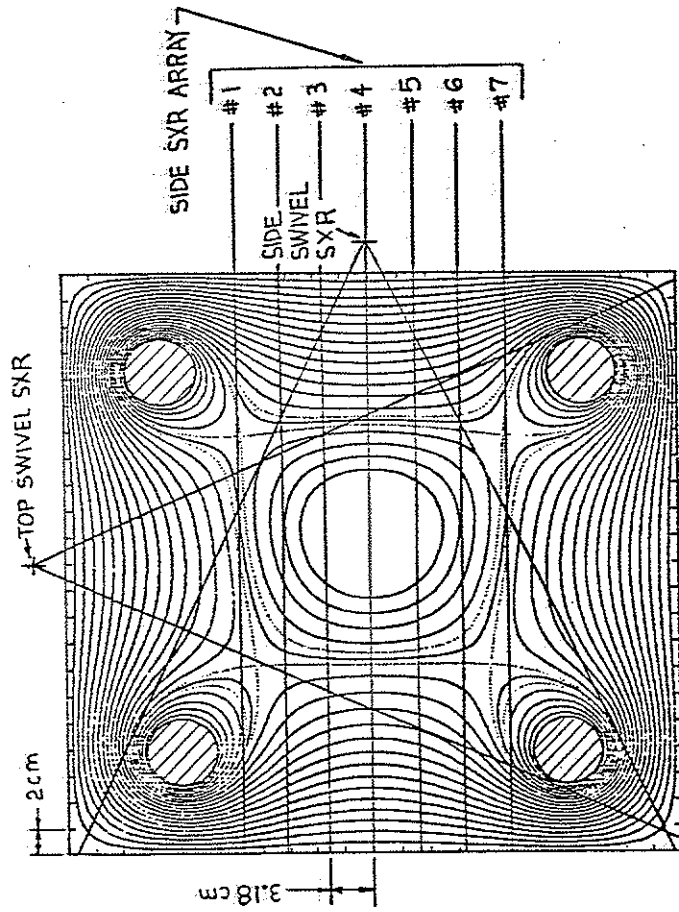
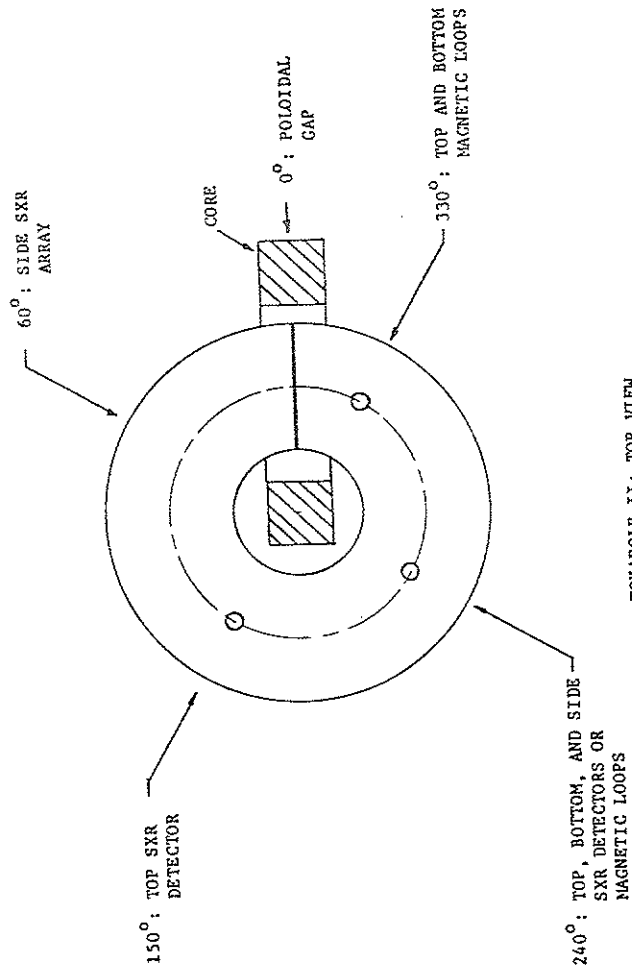


FIG. 3-9. Toroidal location of SXR array and other diagnostics. The toroidal azimuth is defined relative to the location of the poloidal gap.



TOKAPOLE II: TOP VIEW

These probes consisted of a single loop of wire of uniform width encased in a 1/4" S.S. tube. When a probe of this type is inserted vertically from the machine top or bottom, and oriented with the plane of the loop parallel to the toroidal direction, it intercepts an amount of poloidal magnetic flux proportional to the total poloidal magnetic flux,  $\phi_{\text{inside}}$ , between the machine wall and the probe tip (assuming toroidal symmetry). An imaginary toroidal loop passing through the probe's tip then links the transformer core and  $\phi_{\text{inside}}$ . Thus, the voltage along this loop is

$$V_{\text{loop}} = -(\dot{\phi}_{\text{core}} - \alpha \dot{\phi}_{\text{probe}}) = V_{\text{pg}} - \alpha V_{\text{probe}} \quad (3.6)$$

where  $\alpha$  is a constant which depends on the coil's area.  $\alpha$  can be determined experimentally from the fact that  $V_{\text{loop}}$  on the midplane in vacuum =  $V_{\text{pg}}/2$ .

Rapid changes in the plasma position, inductance, or current can accompany the instabilities studied. An electric field probe responds to the subsequent, fast, changes in the flux with voltage spike. Using a simple circuit model<sup>18</sup>,

$$V_{\text{probe}} = (L_{\text{plasma}} I_{\text{plasma}})' + (L_{\text{ring}} I_{\text{ring}})' \quad (3.7)$$

Changes in parameters within the plasma current channel affect the ring inductance and current only as images and are therefore of higher order so that



$$V_{\text{probe}} = (L_{\text{plasma}} I_{\text{plasma}})^{-1/2}$$

(3.8)

References for Chapter 3

- <sup>1</sup>A.P. Biddle, R.N. Dexter, R.J. Groebner, D.J. Holly, B. Lipschultz, M.W. Phillips, S.C. Prager, and J.C. Sprott, Nucl. Fusion, 19, 1509 (1979).
- <sup>2</sup>J.C. Sprott, University of Wisconsin-PLP 744 (1978).
- <sup>3</sup>R.J. Groebner, Ph.D. Thesis, University of Wisconsin (1979).
- <sup>4</sup>M. Nagami et al., Nucl. Fusion, 20, 1325 (1980).
- <sup>5</sup>M. Keilhacker et al., in Plasma Physics and Controlled Nuclear Fusion Research (Proc. 8th Int. Conf. Brussels, 1980), 2, IAEA, Vienna, 351 (1981).
- <sup>6</sup>D. Meade, et al., in Plasma Physics and Controlled Nuclear Fusion Research (Proc. 8th Int. Conf. Brussels, 1980), 1, IAEA, Vienna, 665 (1981).
- <sup>7</sup>DIVA Group, Nucl. Fusion, 18, 1619 (1978).
- <sup>8</sup>P. Wagner, et al., Phys. Rev. Letts., 49, 1408 (1982).
- <sup>9</sup>T.H. Osborne, University of Wisconsin-PLP 830 (1980).
- <sup>10</sup>B. Lipschultz, Ph.D. Thesis, University of Wisconsin (1979).
- <sup>11</sup>S. von Goeler, in Diagnostics for Fusion Experiments (Proc. of the Course, Varenna 1978), Pergamon Press, 79 (1979).
- <sup>12</sup>N.R. Sauthoff, S. von Goeler, W. Stodiek, Nucl. Fusion, 18, 1445 (1978).
- <sup>13</sup>R.J. Groebner, Ph.D. Thesis, University of Wisconsin (1979).
- <sup>14</sup>W.R. Wing, in Plasma Diagnostics and Data Acquisition Systems (Proc. of the Course, Varenna 1975), Editrice Compositori, Bologna, 324 (1975).
- <sup>15</sup>R.J. Groebner and R.N. Dexter, University of Wisconsin-PLP 770 (1978).
- <sup>16</sup>G.M. McCracken and P.E. Stott, Nucl. Fusion, 19, 889 (1979).
- <sup>17</sup>G. Knoll, Radiation Detection and Measurement, John Wiley & Sons, chap. 11 (1979).

## CHAPTER 4

INTRODUCTION TO RESULTS

The plasma behavior in different operational regimes, as characterized by the parameter  $\langle q \rangle$ , is summarized in figure 4-1.  $\langle q \rangle$  is the  $q$  at the edge of a uniform current density circular plasma with the same current and roughly the same cross sectional area as the actual discharge.  $\langle q \rangle$  is derived from the circuit parameters<sup>1</sup> as follows. Assuming the current in the plasma is a filament down the vacuum vessel minor axis, and that the rings are symmetrically placed and carry equal currents, then the radial position of the poloidal field null is given by

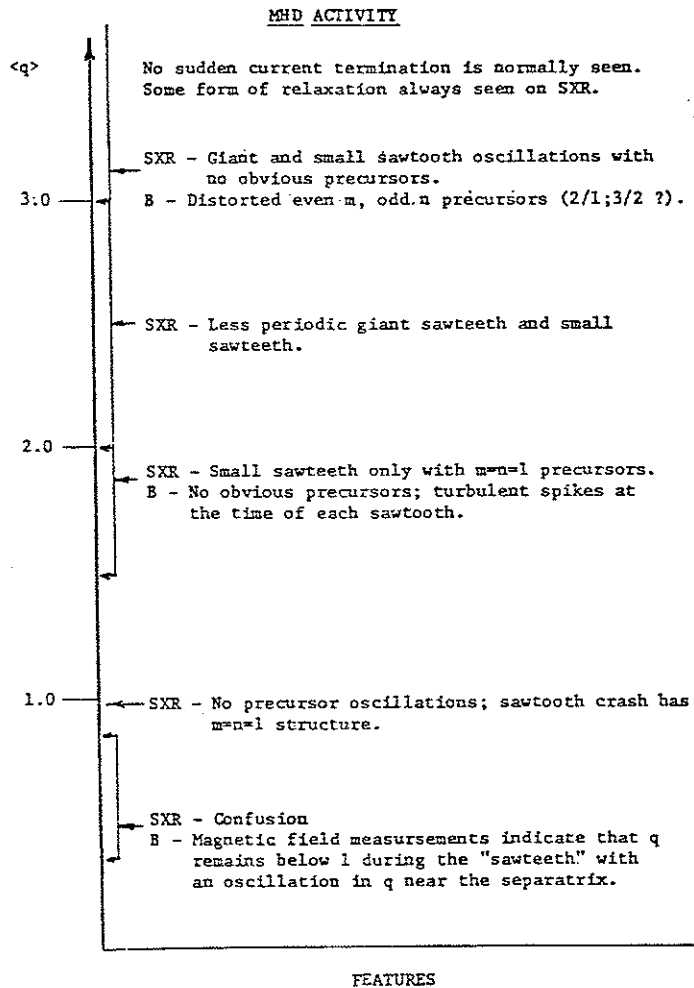
$$a = 17.4(I_p/I_{Rings})^{0.25} \text{ (cm)}, \quad (4.1)$$

where the poloidal field of the rings is assumed to vary as  $r^3$  (strictly true only near the vacuum poloidal field null).  $\langle q \rangle$  is defined as the edge  $q$  value of a uniform current density cylindrical plasma carrying current  $I_p$ , with the same area as a square of half diagonal  $a$ :

$$\langle q \rangle = a^2 B_\phi(T)/I_p \text{ (kA)}. \quad (4.2)$$

$\langle q \rangle$  is close to the central  $q$  values if the current density is sufficiently flat (as exists for the very low  $q$  case), and gives a

FIG. 4-1. General characteristics of MHD activity parameterized by  $\langle q \rangle$ . Above  $\langle q \rangle = 1.5$  the damped form of  $V_{pg}$  is used, while below  $\langle q \rangle = 1$  the quarter sine wave form of  $V_{pg}$  is used.



value that is close to the actual  $q$  at about 80% of the minor radius in the more peaked cases (e.g. the better confined high  $B_\phi$  case).

All plasmas with  $\langle q \rangle < 1$  were obtained with the quarter sine wave driving voltage while all those with  $\langle q \rangle > 1.5$  used the damped  $V_{PG}$  with power crowbar. Tokamak discharges with  $q$  values as low as 0.5 over most of the current channel within the separatrix can be formed for 3-4 ms. These discharges show sawtooth oscillations on the SXR signals, but magnetic probe measurements indicate the central  $q$  values, instead of relaxing to 1, as would be expected for internal disruptions, remain nearly fixed. The  $q=1$  surface for this case is very near the separatrix, and there is a small oscillation in  $q$  near the  $q=1$  surface which is time correlated with the SXR sawtooth oscillations. These discharges have poor energy confinement ( $\tau_E < 50\mu s$ ), and so, would require a large ohmic heating power input to be sustained. The discharge length is thus limited severely by the available volt-seconds of the iron core. The 3-D nonlinear resistive MHD code, HIB,<sup>2</sup> provided by the Princeton Plasma Physics Laboratory has been employed in an attempt to reconcile the very low  $q$  data with the resistive tearing mode theory. This has not yet provided an understanding of the very low  $q$  results.

If  $\langle q \rangle = 1$ , sawtooth oscillations are observed which show no precursor oscillations; instead, the disruption (sawtooth crash) itself has an  $m=n=1$  helical structure. A helical structure in the

sawtooth crash is consistent with the classic Kadomtsev model, and may be a unique example of the continued applicability of this picture through the nonlinear phase of the 1/1 disruption.

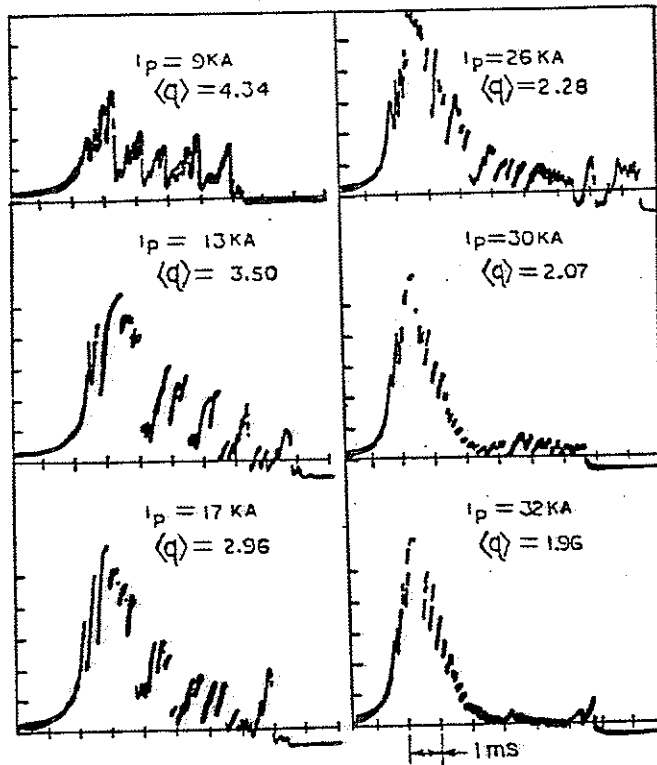
As  $\langle q \rangle$  is decreased from 4 to 2 in an  $I_p$  scan at constant  $B_\phi$ , the characteristic of the sawtooth oscillations, as viewed on chord 4 (central) of the side SXR array, changes greatly (figure 4-2).

At low  $I_p$ , 3 or 4 small sawteeth of period 100-200 $\mu$ s are superimposed on giant sawteeth of period = lms. This uniform combination of large and small sawteeth is obtained whenever  $\langle q \rangle > 3.0$ , and is independent of the plasma density. Precursor oscillations of even m and odd n character are observed on magnetic loops for both the giant and small sawtooth oscillations. An odd m mode with twice the frequency of the even m odd n mode appears just before the disruption. This is consistent with the standard 2/1 disruption model; the superimposed odd m mode may be a coupled 3/2. Except at very low density,  $I_p$  is not terminated in a disruption.

As  $I_p$  is increased with  $B_\phi$  constant, the giant sawteeth become less regular. Below  $\langle q \rangle = 2$ , only small sawtooth oscillations are observed. These sawteeth show very little magnetic precursor, but instead, show a strong 1/1 precursor on the SXR. Fits to an MHD equilibrium code<sup>3</sup> indicate that the q=2 surface is very near the separatrix for this case. This suggests that the 2/1 disruption has been eliminated, leaving only the internal 1/1 mode, perhaps as a result of the proximity of the q=2 surface and the separatrix.

FIG. 4-2. Change in the character of the sawtooth oscillations as  $I_p$  is increased at constant  $B_\phi$ . At high  $\langle q \rangle$  both large and small sawtooth oscillations are seen, while at low  $\langle q \rangle$  only small sawtooth oscillations are seen.

These discharges have relatively good energy confinement time ( $\tau=600\mu\text{s}$ ), similar to the  $\langle q \rangle=3.0$  case.



References for Chapter 4

- <sup>1</sup>J.C. Sprott, University of Wisconsin-PLP 889 (1983).
- <sup>2</sup>R. Izzo, et al., Phys. Fluids, 26, 2240 (1983).
- <sup>3</sup>M.W. Phillips, University of Wisconsin-PLP 765 (1978).

## CHAPTER 5

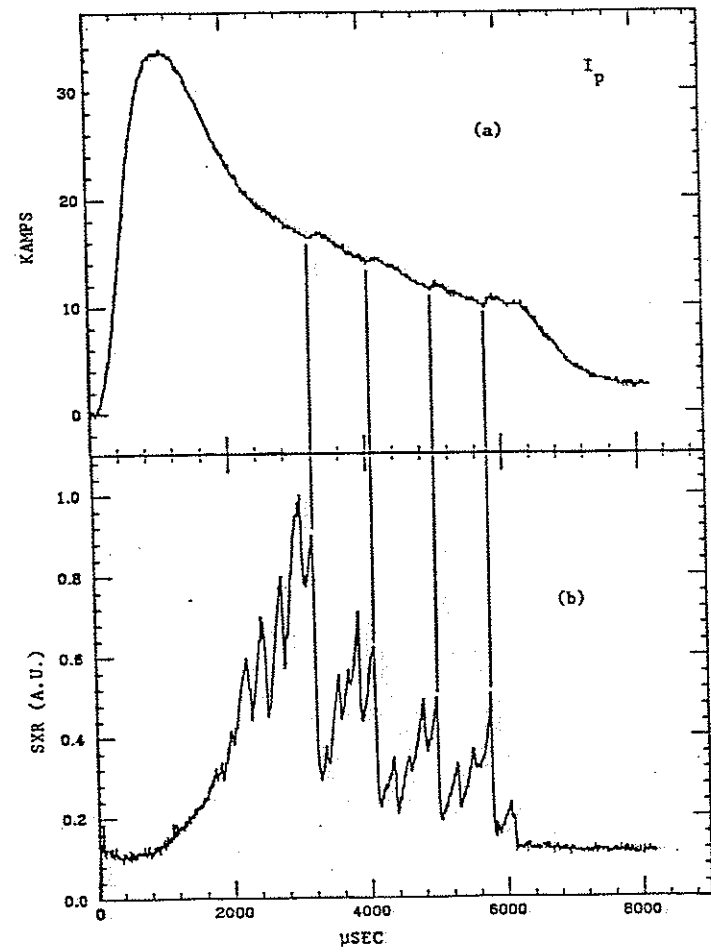
DATA AND ANALYSIS FOR  $\langle q \rangle = 3.0$ 

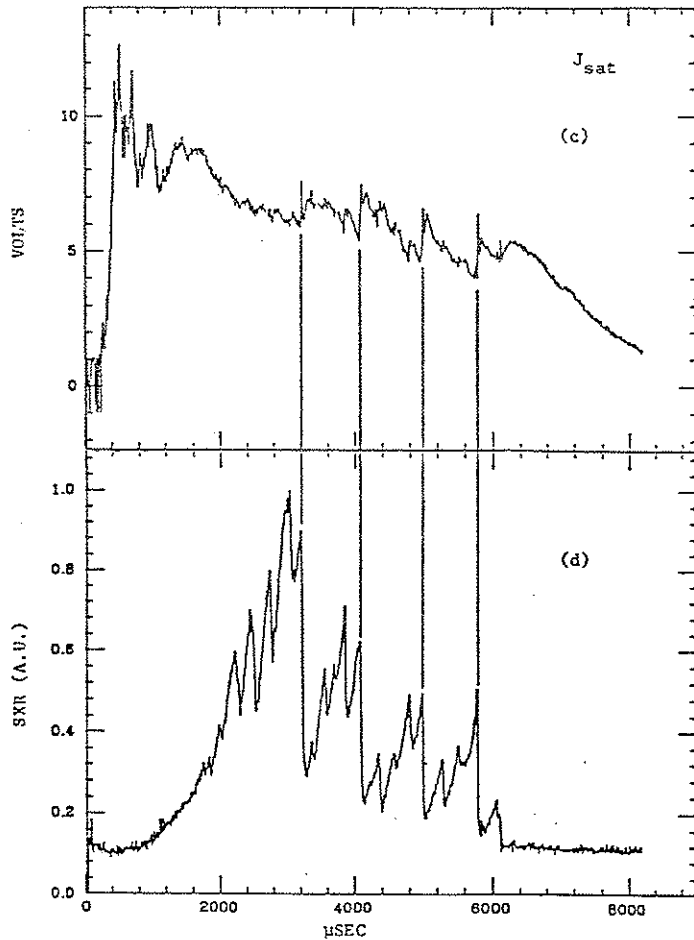
The sawtooth oscillations observed for this case seem to be associated with a 2/1 mode that is observed on magnetic pick up loops located near the separatrix. The SXR data show some precursor activity that may include odd and even modes, but cannot be attributed to a 1/1 mode. Fits of the inversion radius of the sawtooth oscillations, the position in major radius of the peak in the SXR emissivity, and the gross plasma parameters to an MHD equilibrium code are consistent with an inversion radius near the  $q=2$  surface; it is difficult to fit this data under the assumption that the inversion radius is at the  $q=1$  surface. These facts suggest that the sawtooth oscillations observed for this case are 2/1 related disruptions. The fact that the plasma current is not terminated in this case could be the result of the small major radius shift predicted for a flattening of the current density profile coupled with the lack of a material boundary near the separatrix.

A. Soft X-Ray Data

At  $\langle q \rangle = 3$ , the SXR signal shows giant sawtooth oscillations with a period of about 1 ms; superimposed on the large sawteeth are several small sawteeth with a period of about 200  $\mu$ s (figure 5-1b).

FIG. 5-1. Large sawtooth oscillations (b,d) correlated with (a) upward bumps in  $I_p$ , and (c) sharp inverted sawtooth oscillations in the average pressure outside the separatrix.





Coincident with the rapid drops in the SXR signal, there is an upward bump in  $I_p$  (figure 5-1a), and a fast upward jump in the pressure outside the separatrix, as read by a probe that is proportional to the volume average of  $n_e(T_e)^{1/2}$  over this region<sup>1</sup> (figure 5-1c).

The SXR signals for a giant sawtooth are shown in figure 5-2, while those for a small sawtooth are shown in figure 5-3. Signals from 3 detectors spaced  $90^\circ$  apart toroidally ( $60^\circ$  is the location of the side array), show an apparent lack of symmetry in both the large (figure 5-2b) and small sawteeth (figure 5-3b). Typically, models for the disruption,<sup>2</sup> and the experimental results<sup>3</sup> indicate that the drop in the SXR emissivity should be nearly  $m=n=0$ , and should propagate inward in minor radius, with an inversion near (but sometimes inside) the  $q=2$  surface. Some major disruptions on PLT,<sup>3</sup> however, show an asymmetric drop in the SXR emission which is similar in character to the one observed on Tokapole II. On PLT, the disruption appears to propagate inwards from the  $q = 2$  surface, but SXR chords above the midcylinder fall more rapidly than chords below. Chords on the bottom near the inversion radius initially drop more rapidly than the corresponding chord on the top, then increase again, before finally falling sometime after the top chord (figure 5-4). The authors of reference 3 felt that this asymmetry could not be due to a motion of the plasma center because the upper chords showed no drop corresponding to the upward bump of the lower chords. Instead, they attributed the asymmetry to some type of



FIG. 5-2. Large sawtooth on (a) side array and (b) toroidally spaced SXR detectors. The detector at side  $60^\circ$  is tilted  $9.6^\circ$  down; the detector at top  $150^\circ$  is tilted  $2.6^\circ$  in toward the major axis; the detector at side  $240^\circ$  is tilted  $9.6^\circ$  up. The toroidally spaced detectors show an apparent asymmetry in the disruption.

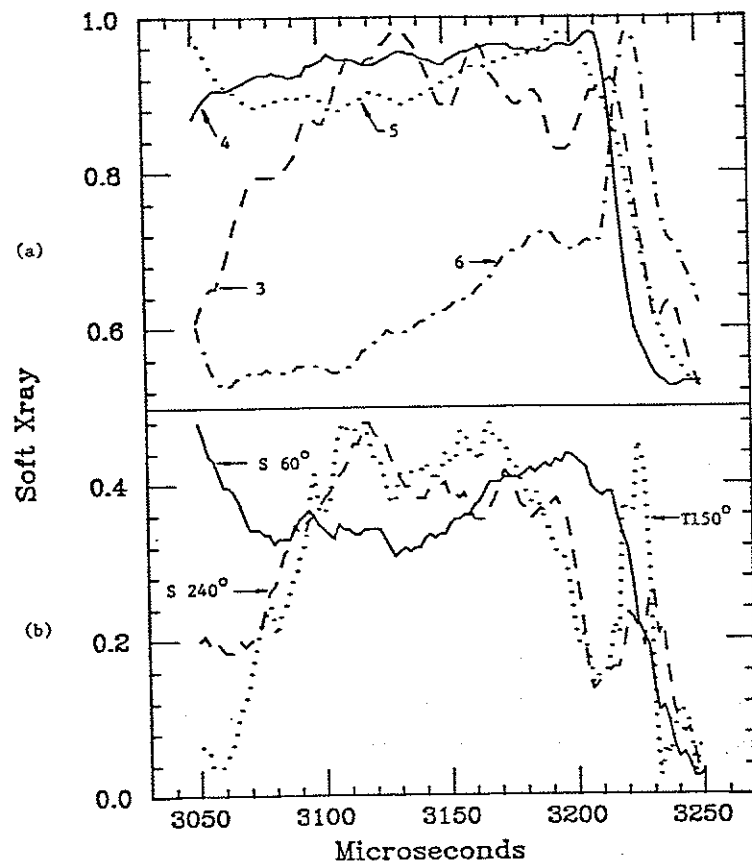


FIG. 5-3. Small sawtooth on (a) side array and (b) toroidally spaced SXR detectors. The detector at side  $60^\circ$  is tilted  $9.6^\circ$  down; the detector at top  $150^\circ$  is tilted  $2.6^\circ$  in toward the major axis; the detector at side  $240^\circ$  is tilted  $9.6^\circ$  up. The toroidally spaced detectors show an apparent asymmetry in the disruption. The side array signals (a) show possible precursor oscillations: a low frequency, possibly even  $m$  mode between  $2600\mu\text{s}$  and  $2700\mu\text{s}$ , and a high frequency, possibly odd  $m$  mode between  $2700\mu\text{s}$  and the disruption.

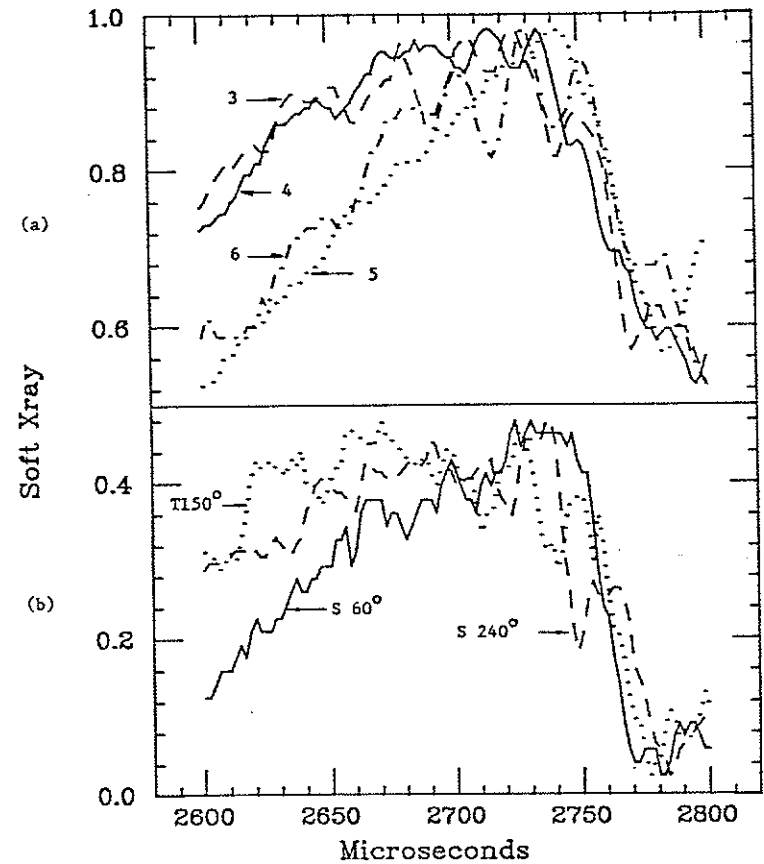
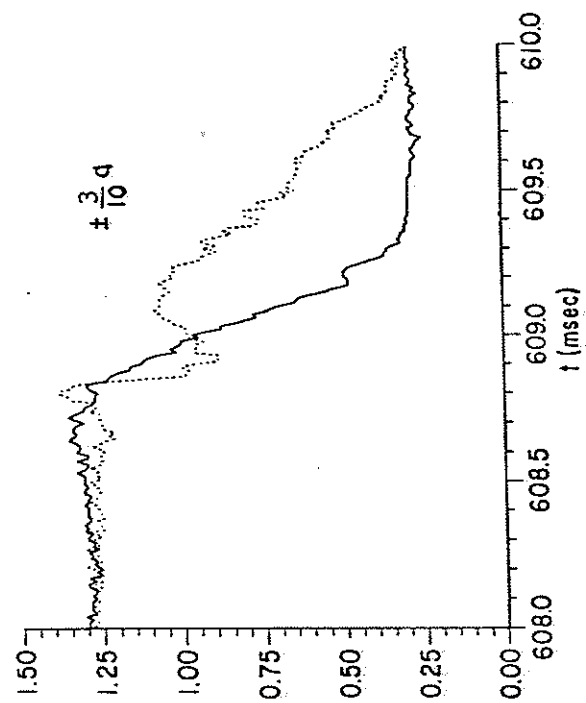


FIG. 5-4. Asymmetry in a  $2/1$  disruption on PLT.<sup>3</sup> The signals are from chords located on opposite sides of the midplane at  $3/10$  of the minor radius to the limiter which defines the plasma boundary.



mode coupling effect, possibly between 1/1 and 2/1 mode (both of which were observed with nearly the same frequency).

The chords shown in figure 5-2b and 5-3b are somewhat inside the inversion radius for the sawteeth. The upward jump in the top 150° and side 240° signals could be due to the increase in temperature of the outer regions of the plasma which lie along the line of sight of the detectors. Since the side 60° detector is pointed down 9.6° while side 240° is pointed up 9.6°, the lack of an upward bump in the side 60° signal may be due to the fact that the peak of the SXR emission usually indicates that the plasma sits 1-2cm below the midplane. If the upward jump in the top 150° and side 240° signals is due to the plasma center being below the midplane, then the time difference between the first drop of side 240° at 3180μs in figure 5-2b, and the drop of side 60° at 3200μs may then be attributed to propagation of the disruption inward in minor radius. This interpretation is somewhat borne out from the side array signals, especially for the small sawtooth of figure 5-3a. In this figure, if the center of the plasma is assumed to be near but somewhat above chord 5, then the propagation of the first large drop in the signals in the order 3-6-4-5 near 2730μs is consistent with inward propagation.

Some precursor oscillations can be seen on chords 3, 4, and 6 in figure 5-3a. From 2600μs to 2700μs a mode with period ≈50μs is seen, that seems to be in phase for the detectors. Between 2700μs and the time of the disruption at 2730μs, a mode with period of

≈20μs is seen. This higher frequency mode flips phase between chords 3 and 4, and again between chords 4 and 6. As described in the section B, the magnetic coil signals show an even m, odd n precursor, with perhaps an odd m even n mode at twice the frequency superimposed. The low frequency mode just described is consistent with the even m magnetic precursor. The inversion of the higher frequency mode across chord 5 is consistent with the presence of an odd m island; the second inversion between 3 and 4 could be that which would be expected across the localized island itself. The structure of these oscillations cannot be consistent with a growing 1/1 mode.

#### B. Magnetic Precursor Oscillations

The central chord SXR signal, and the signal to a coil which is oriented to pick up the poloidal field component along a major radius are shown in figure 5-5. This coil was located on the midcylinder, 11cm from the midplane. The frequency components of the magnetic pick up loop signal below 10 kHz have been filtered out; the high frequency response of the coil is limited to 300kHz. An expansion of the fourth spike of figure 5-5b, shows the growth of the magnetic oscillations just before the SXR drop (figure 5-6). In figure 5-6c,d coils located 11cm above the midplane 180° away in toroidal angle from the coil in 5-6b, and a coil located 11cm below the midplane at the same toroidal angle as 5-6b, show the even m odd n character of the precursor oscillations.

FIG. 5-5. Bursts of oscillations on magnetic field pick up loops at every SXR sawtooth: (a) large and small sawtooth oscillations on the central chord detector (4) of the side SXR array; (b) the signal from a poloidal magnetic field pick up loop located 11cm above the midplane on the midcylinder.

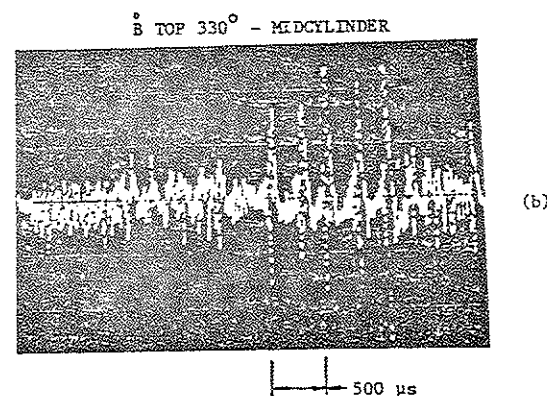
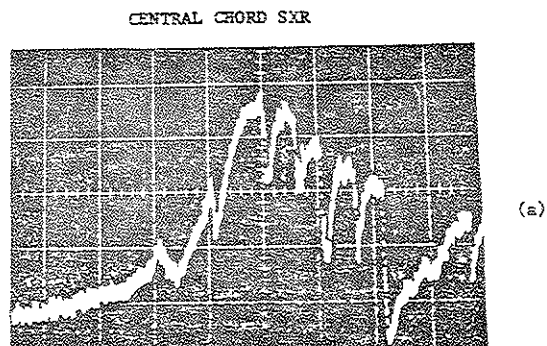
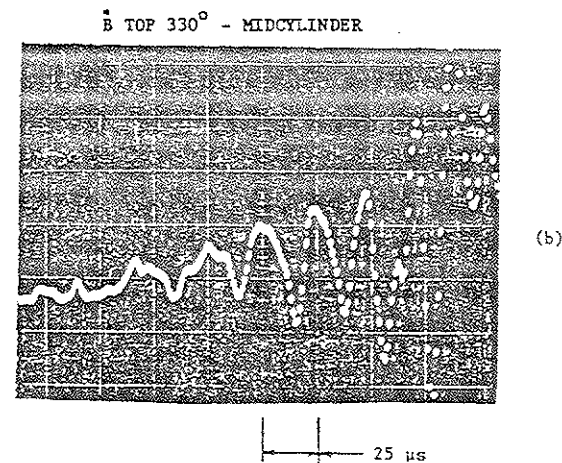
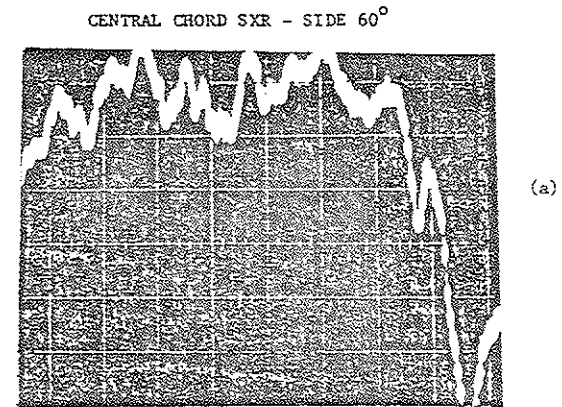
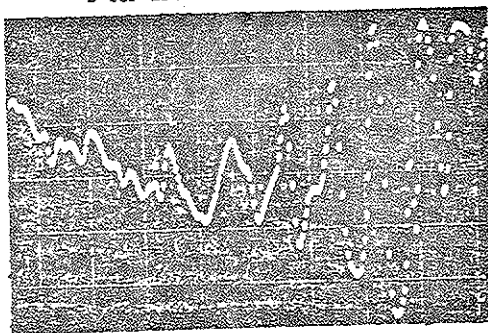


FIG. 5-6. Basic even  $m$  odd  $n$  structure of the magnetic precursor oscillations: (a) expansion of the SXR signal for the sawtooth that occurs 750 $\mu$ s after the time at the center of figure 5-5; (b) expansion of figure 5-5b for this sawtooth; (c) signal from a poloidal magnetic field pick up loop located on the midcylinder 11cm above the midplane 180 $^\circ$  away in toroidal angle from the loop in (b); (d) signal from a poloidal magnetic field pick up loop located on the midcylinder 11cm below the midplane at the same toroidal angle as (b).

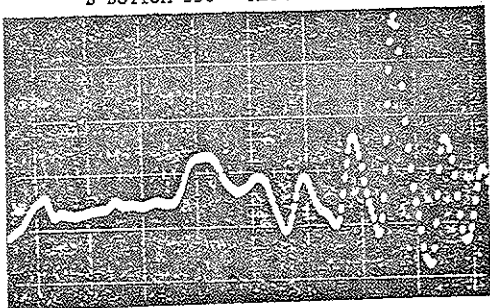


B TOP 150° - MIDCYLINDER



(c)

B BOTTOM 330° - MIDCYLINDER



(d)

A close examination of the precursor oscillations just before the disruption (figure 5-7) shows a distortion of the modes that suggests the presence of an additional component at twice the frequency. If the precursor oscillations are the result of a rigid toroidal rotation of phase locked helical modes, this distortion is consistent with the presence of an odd  $m$  even  $n$  mode of twice the toroidal mode number of the primary even  $m$  odd  $n$  mode. This type of mode locking has been observed on other tokamaks.<sup>4,5</sup>

To analyze the precursor oscillations in more detail, a simulation was performed using the HIB<sup>6</sup> resistive MHD code output (this code is discussed in detail in chapter 8). The magnetic surfaces for a code run, that spontaneously produced a large  $2/1$  and small  $3/2$  island during the course of the  $1/1$  mode evolution in Tokapole flux geometry, are shown in figure 5-8a. To simulate the signals to the pick up coils, the poloidal field component along the major radius at the coil positions was computed as a function of the toroidal angle. In order to produce an observable  $n=2$  perturbation, it was necessary to multiply the  $n=2$  components by a factor of 10; the magnetic surfaces which result show a large ergodic region (figure 5-8b). The simulated coil signals are shown in figure 5-9, and are in qualitative agreement with the observed precursor distortion.

The phase relation between the  $n=1$  and  $n=2$  modes is determined by the fact that all the island o-points are aligned on the outside of the midcylinder on the midplane. This alignment is a feature

FIG. 5-7. Distortion of magnetic precursor oscillations just before the disruption of figure 5-6.

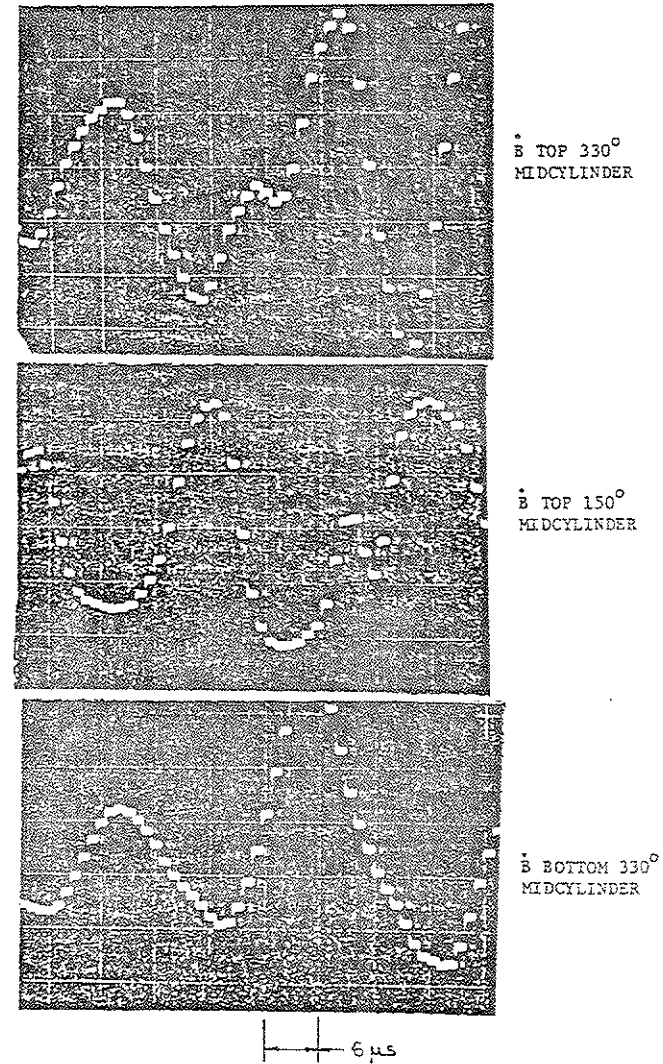




FIG. 5-8. Magnetic surfaces from resistive MHD code run used to simulate the magnetic precursor oscillations in figure 5-6: (a) as they appeared during the code run; (b) when the  $n=2$  components are artificially amplified by a factor of 10.

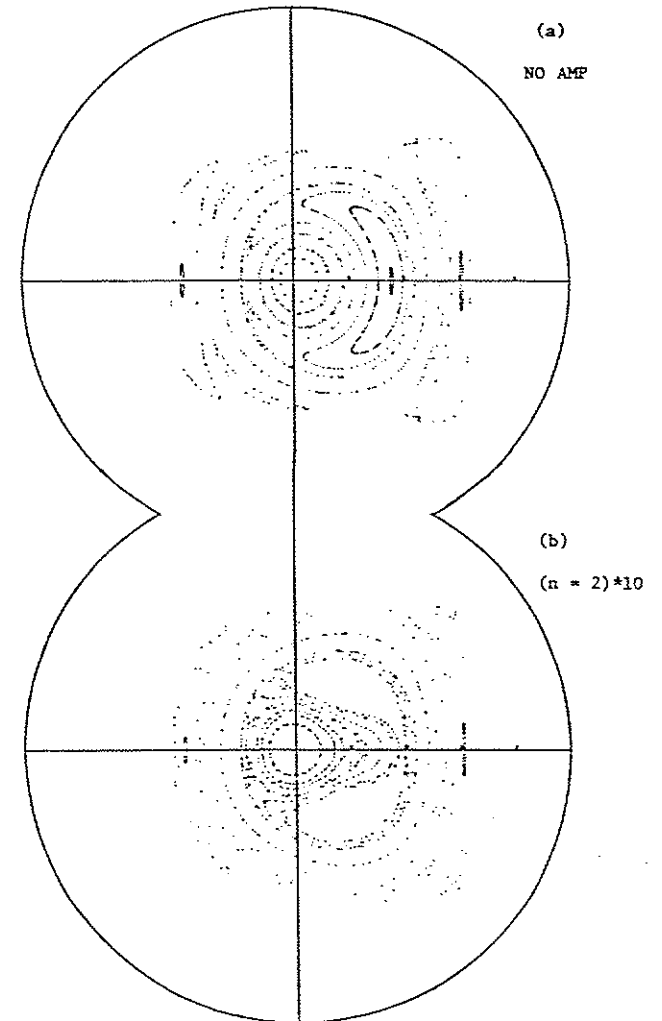
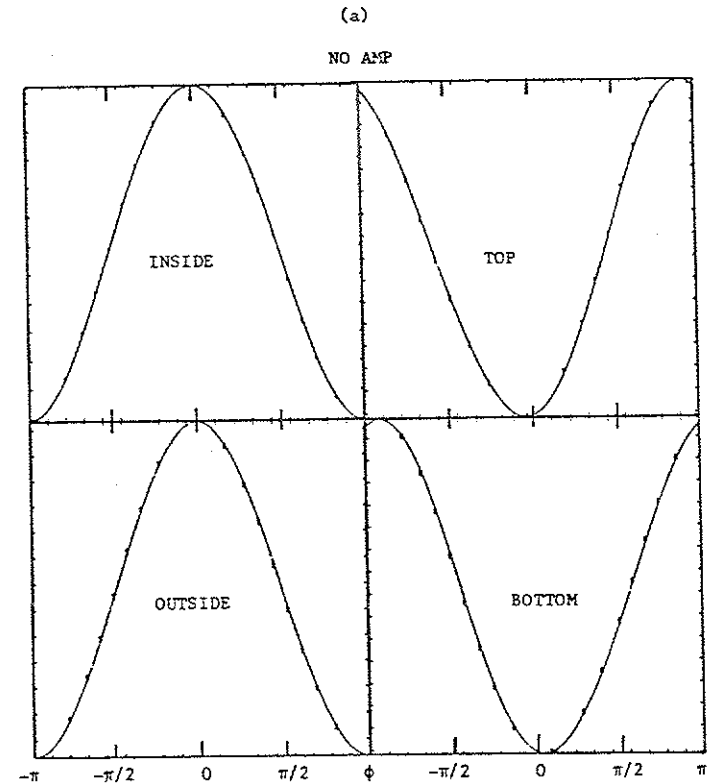
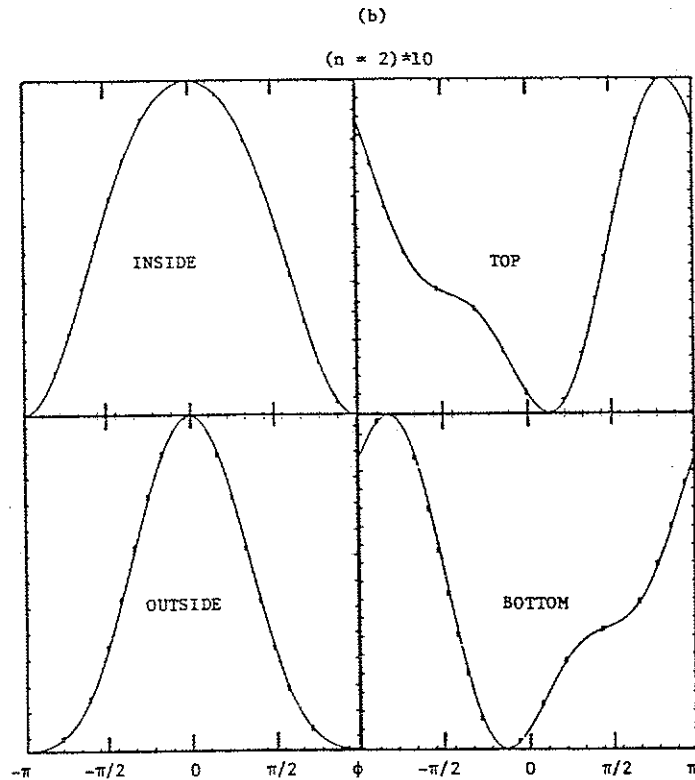


FIG. 5-9. Simulated magnetic precursor oscillations show qualitative agreement with experiment (figure 5-7) if the  $n=2$  components are amplified by a factor of 10, (b); but show nearly a pure  $2/1$  oscillation if no artificial amplification is used (a). The oscillations have an amplitude of about 1% and are plotted with respect to toroidal angle,  $\phi$ , which is equivalent to time for a uniform rotation.





commonly observed in other experiments,<sup>5,6</sup> and results from the fact that the perturbations to the equilibrium current, that produce the magnetic islands, attract each other, and this positioning locates them as close together as possible.<sup>5</sup> With this position of the alignment point, the direction of toroidal rotation, inferred from the distortion of the precursor oscillations, would be observed for a poloidal rotation in the electron diamagnetic drift direction.

### C. Current Termination in Tokapole II Disruptions

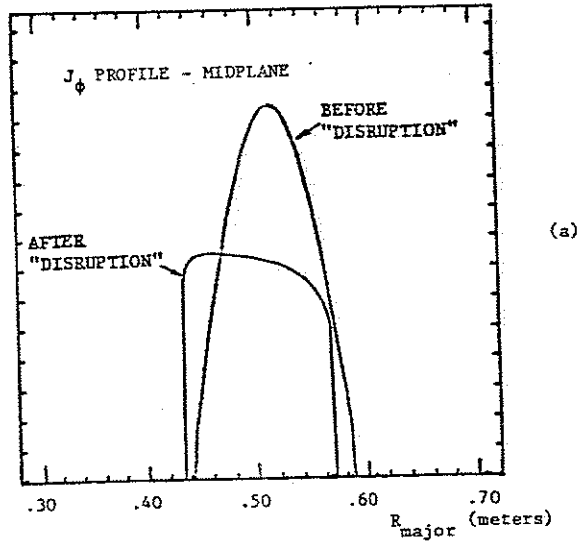
As mentioned in chapter 2, perhaps the principal cause of termination of the plasma current during a disruption is the large inductance and  $\langle\beta\rangle$  drop, that shifts the plasma inwards in major radius. The subsequent interaction of hot plasma with limiter or wall surfaces causes a large impurity influx. The radiated energy loss from these impurities can be substantial. Also, the charge exchange loss of hot plasma can be large. These effects result in a more resistive plasma with poorer energy confinement, that often cannot be sustained by the ohmic heating power input. Loss of the current results. The fact that no current termination is seen in Tokapole II disruptions may be the result of the lack of a physical boundary near the plasma current channel.

The major axis shift in Tokapole II is small even for a very large change in the plasma inductance and  $\langle\beta\rangle$ . An MHD equilibrium code<sup>7</sup> was used to simulate the effects of the disruption. This was

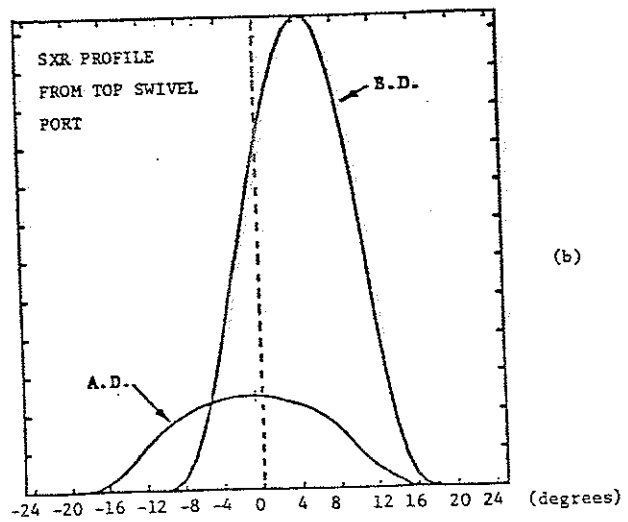
done by starting with an equilibrium that matched the  $I_p$ ,  $I_{rings}$ ,  $B_\phi$ , and position of the peak of the SXR profile as determined from a tiltable detector on the midcylinder. The current density and pressure profiles were then flattened greatly, keeping  $I_p$  constant, to simulate the effects of the disruption (figure 5-10). The change in the equilibrium that this "disruption" caused is shown in figure 5-11. The shift in major radius is only 2cm, and does not result in contact between the plasma within the separatrix and the baffle plate. The small major axis shift is probably the result of image currents induced in the inner rings; in addition a divertor vertical field is inherently less susceptible to these shifts.<sup>8</sup>

The current termination that is observed in  $\langle q \rangle = 3$  plasmas at low density might be related to the large number of "run away" electrons which seem to be present in these discharges.<sup>9</sup> Run away electrons occur if the collision frequency is not sufficiently high to moderate the electron velocity in the toroidal electric field. The ergodic magnetic field region, which forms during the instability, would cause a rapid transport of these electrons out from the plasma center where their orbits are presumably well confined to the edge region where they may be lost. Large bursts of hard x-rays accompany the current termination in low density discharges. If a significant portion of  $I_p$  was carried by these electrons, their loss could represent a substantial current drop. In addition, for plasmas with a large component of run away electrons, the temperature of the background plasma can be much

FIG. 5-10. Simulated changes in the toroidal current density,  $J_\phi$ , and SXR profile, as viewed from a tiltable detector on the top midcylinder, used to test the equilibrium shift that would occur during a disruption. The total plasma current is held constant in the  $J_\phi$  change.

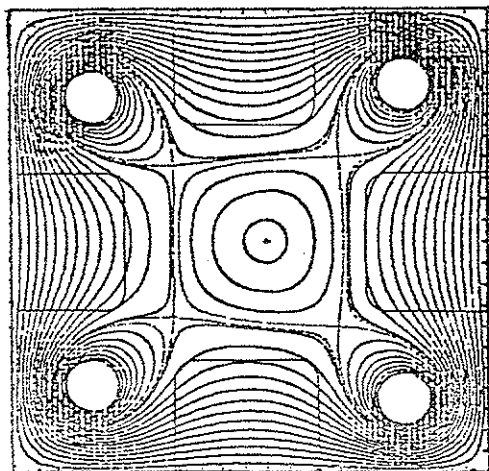


(a)

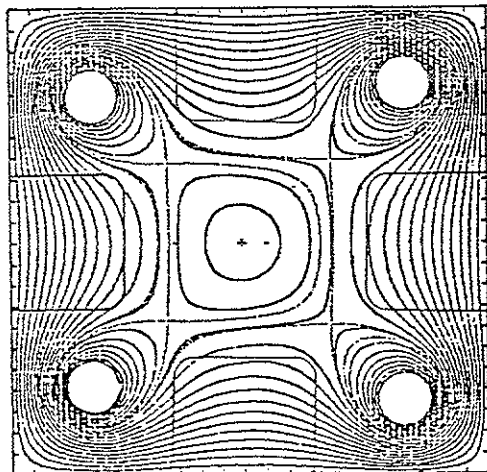


(b)

FIG. 5-11. Simulated shift in equilibrium due to current density and pressure profile flattening in a disruption (figure 5-10). The shift of the magnetic axis is 1.94 cm.



BEFORE  
"DISRUPTION"



AFTER  
"DISRUPTION"

2 CM

lower than what would be expected from the plasma conductivity.<sup>10</sup> Also, large impurity influx may result from impact of the high energy electrons. A factor of 3 increase in the visible light intensity was observed at the time of the disruption compared to a 30% increase in a disruption that did not terminate the current. These conditions would leave a cold low conductivity plasma with large impurity content after the loss of the runaway electrons that might produce complete current termination.

#### D. Transport Across the Equilibrium X-Points During Disruption

A Langmuir probe<sup>11</sup> was used in a preliminary attempt to see if the equilibrium separatrix was somehow involved in the disruption. The probe was biased positive to collect saturated ion current, and a scan was taken over the points shown in figure 5-12. The loss of plasma (or perhaps runaway electrons) propagates rapidly into the flux region surrounding the ring (figure 5-13c,d). This suggests that this region of flux space may be involved in the reconnection during the disruption. Points in the flux region outside the separatrix show a more rapid rise the closer they are in physical space to the x-point region, even though they are approximately on the same flux surface (figure 5-13a,b), which may again indicate some connection between the x-point and the reconnection process.

FIG. 5-12. Position of points in the Langmuir probe scan to test for rapid transport across the separatrix in a disruption.

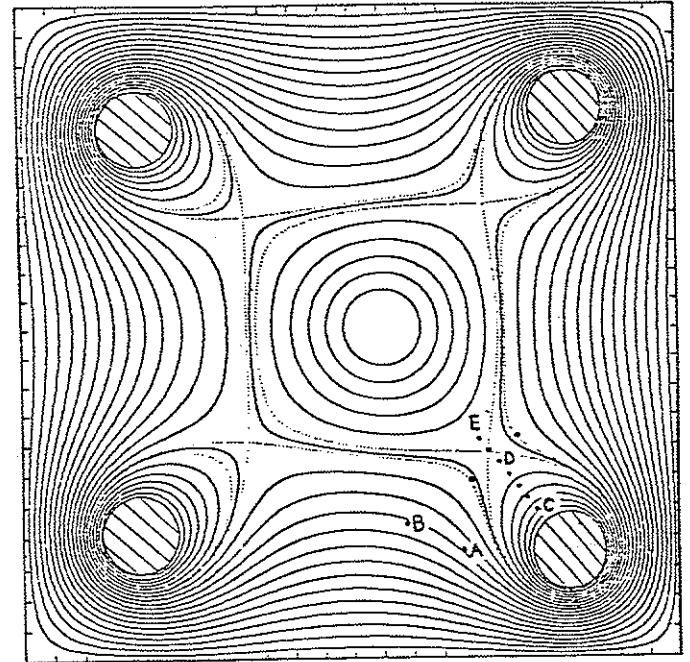
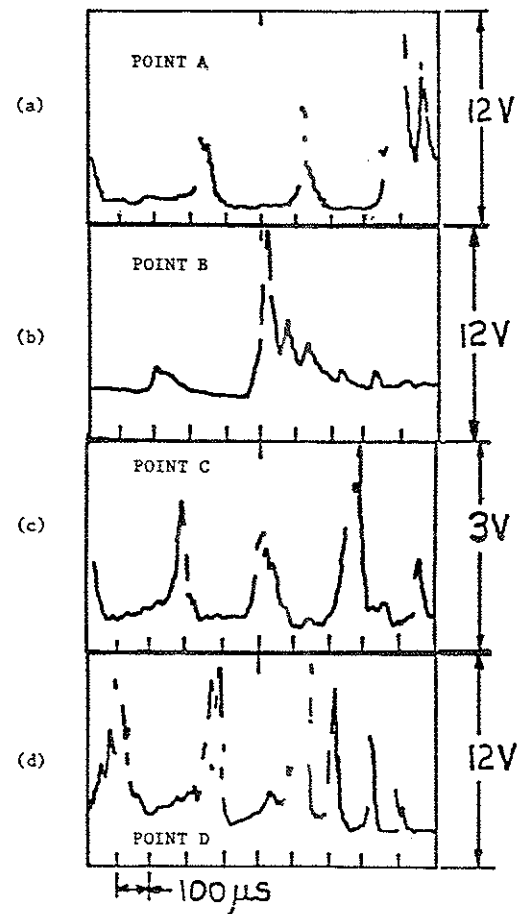


FIG. 5-13. Fast spikes in the signal to a Langmuir probe biased to collect ion saturation current occur for points A, C, and D located near the x-point, while point B located further from the x-point has a more rounded character especially for the small sawtooth. Note the difference in scale for point C.





References for Chapter 5

- <sup>1</sup>R.J. Groebner, Ph.D. Thesis, University of Wisconsin, (1979).
- <sup>2</sup>H.R. Hicks, J.A. Holmes, V.E. Lynch, B.A. Carreras, ORNL Report TM-7733 (1981).
- <sup>3</sup>N.R. Sauthoff, S. von Goeler, W. Stodiek, Nucl. Fusion, 18, 1445 (1978).
- <sup>4</sup>Equipe TFR, Nucl. Fusion, 17, 1283 (1977).
- <sup>5</sup>P. Karger, et al., in Plasma Physics and Controlled Thermonuclear Fusion Research (Proc. 6th Int. Conf. Berchtesgarden, 1976), 1, IAEA, Vienna 267 (1976).
- <sup>6</sup>R. Izzo, et al., Phys. Fluids, 26, 2240 (1983).
- <sup>7</sup>M.W. Phillips, University of Wisconsin-PLP 765 (1978).
- <sup>8</sup>H. Okabayashi, E. Maeda, H. Takahasi, M. Reusch, PPPL Report - 1707 (1980).
- <sup>9</sup>R.N. Dexter, private communication.
- <sup>10</sup>V.S. Vlasenkov, V.M. Leonov, V.G. Merezkin, V.S. Mukhovatov, Nucl. Fusion, 13, 509 (1973).
- <sup>11</sup>F.F. Chen, in Plasma Diagnostic Techniques, Academic Press, New York, 113 (1965).

## CHAPTER 6

DATA AND ANALYSIS FOR  $\langle q \rangle < 2.0$ 

For  $\langle q \rangle < 2.0$  only small sawtooth oscillations are seen. A strong  $m=u=1$  precursor oscillation is observed on the SXR signals for this case, and no clear precursor is observed on the magnetic signals. These observations suggest that these sawtooth oscillations are disruptions associated with the 1/1 mode. Fits to an MHD equilibrium code are made by locating the inversion radius of the sawteeth just inside the  $q=1$  surface, using the location in major radius of the peak of the SXR emissivity profile as an indication of the center of the discharge, and including the gross plasma parameters. They indicate that the  $q=2$  surface is very near the separatrix. The lack of 2/1 related disruptions in this case may be due to this location, and the presence of plasma current or hot plasma outside the separatrix.

A. SXR

Precursor oscillations can be seen on several sawtooth oscillations in figure 6-1. The overall rapid drop of the signal is due to a density loss that can be reduced by more careful gas puffing. A growing odd  $m$  oscillation can be seen on chords 3 and 5 of the side SXR array in figure 6-2a. The central chord signal is hard to interpret because of line averaging effects. In figure

FIG. 6-1. SXR signal for chord 5 of the side array shows only small sawtooth oscillations for  $\langle q \rangle < 2$ .

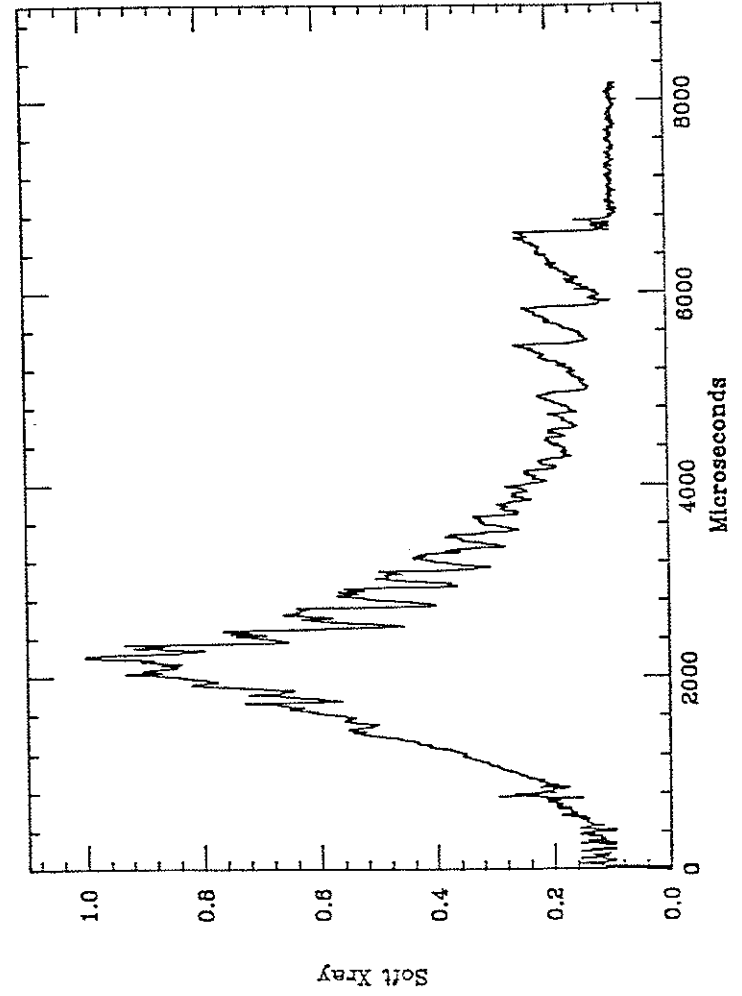
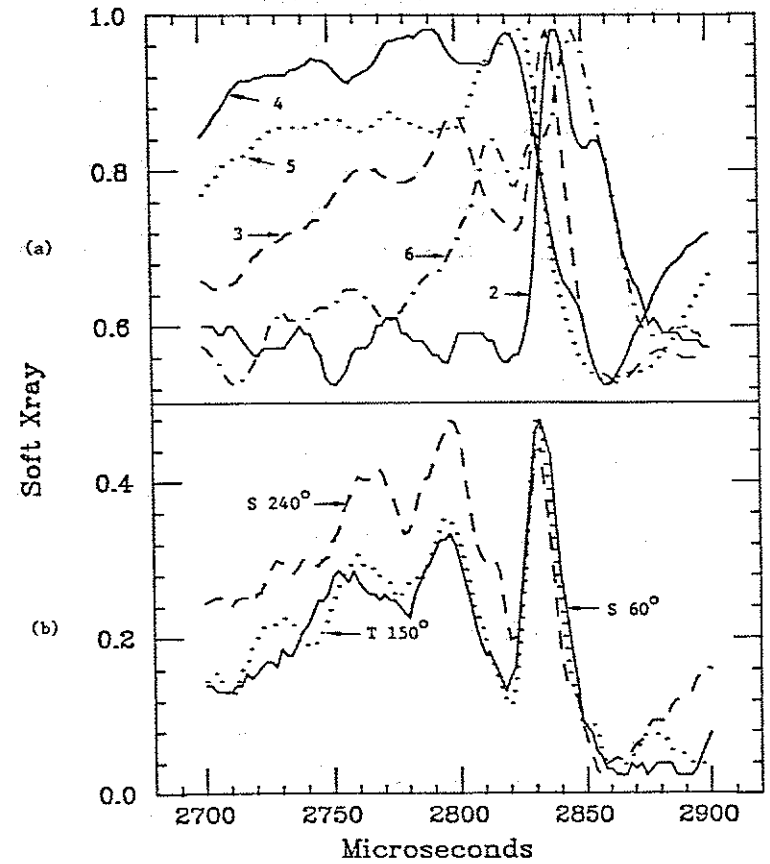


FIG. 6-2.  $m=n=1$  structure of SXR precursor oscillations is indicated from signals to toroidally displaced detectors (b). The side  $60^\circ$  detector is tilted up  $12^\circ$ ; the top  $150^\circ$  detector is tilted  $2^\circ$  inward toward the major axis; the side  $240^\circ$  detector is tilted  $12^\circ$  down. The fact that these detectors are in phase is consistent with a mode that is of constant amplitude on a field line at the  $q=1$  surface in Tokapole II.



6-2b the signals from 3 detectors spaced  $90^\circ$  apart in toroidal angle clearly show the growing precursor oscillations. These detectors were tilted to match the pitch of an  $m=n=1$  field line (Figure 6-3), and the fact that all the precursors are in phase indicates an  $m=n=1$  mode; reversing  $B_\phi$  inverts the precursor oscillations seen on the detector at top  $150^\circ$ .

A growth rate for the  $m=n=1$  mode estimated from figure 6-2b gives:  $\gamma_{\text{exp}} = 2.1 \times 10^{-2} \mu\text{s}$ . This value compares well to an estimate based on the single helicity resistive MHD value<sup>1</sup> of  $\gamma_0 = 2 \times 10^{-2} \mu\text{s}$  computed from

$$\gamma_0 = (2\pi r_w q' S)^{2/3} / \tau_R, \quad (6.1)$$

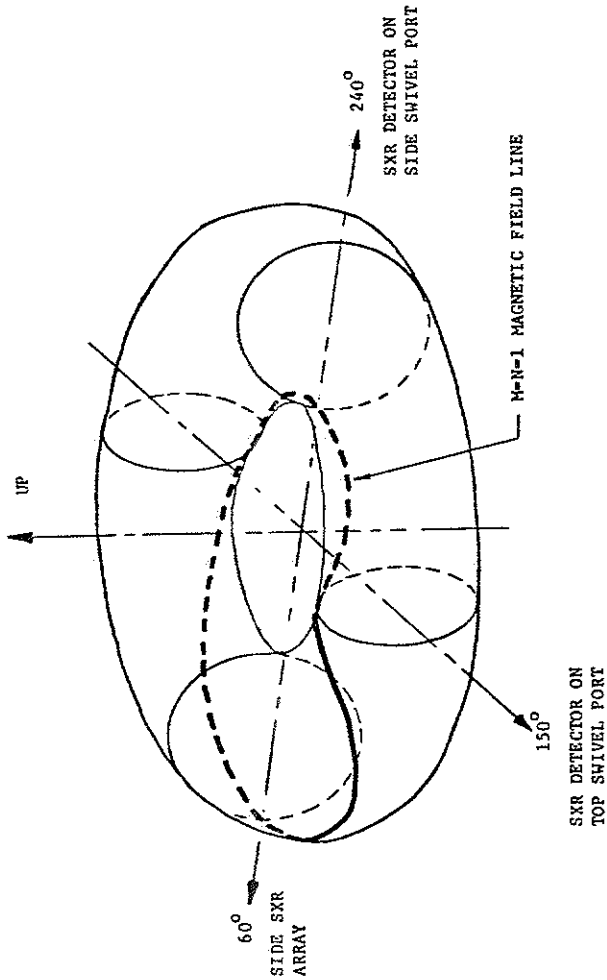
where  $r_w$  is the wall radius (for the numbers given here this was taken as the separatrix radius),  $q'$  is  $dq/dr$  at the  $q=1$  surface, and  $S$  is the magnetic Reynolds number,

$$S = \tau_R / \tau_{\text{HP}} = \left( \frac{r_w^2}{\eta} \right) \left( \frac{R_0 \rho^{1/2}}{B_\phi} \right)^{-1}, \quad (6.2)$$

where  $\rho$  is the mass density. The period of the sawteeth computed from the semiempirical formula,<sup>2</sup>

$$\tau_{\text{st}} = 3 \tau_R^{3/7} \tau_{\text{HP}}^{2/7} \tau_n^{2/7}, \quad (6.3)$$

FIG. 6-3. Pitch of an  $m=n=1$  field line in Tokapole II.



where  $\tau_h = 3nT_e/2\eta j^2$  is a characteristic ohmic heating time, gives  $\tau_{st} = 370\mu s$ , compared to an experimental value of  $200\mu s$ . Equation 6.3 is determined by combining a resistive diffusion equation for the poloidal magnetic field, with a zero dimensional thermal energy balance equation to determine  $q$  and  $\eta$  as a function of time during the ramping up phase of the sawtooth. The thermal energy balance equation includes ohmic heating and lumps the thermal losses into a  $-E/\tau_p$  term.  $q$  and  $\eta$  are then inserted into equation 6.1 to give the growth rate of the mode as a function of time. Ignoring the fact that the presence of a large magnetic island could modify the processes mentioned above, this growth rate is used to compute the size of a 1/1 island as a function of time. The disruption is assumed to occur when the island width reaches the minor radius of the original  $q=1$  surface. Equation 6.3 matches the period of the sawtooth oscillations in most tokamaks, operating over a wide range of parameters, very well.

The diamagnetic frequency was computed from a SXR estimate of the  $I_e$  profile, assuming that electric field effects were negligible.<sup>3,4</sup> The frequency of the precursor oscillation is often found to agree with estimates of the diamagnetic frequency,<sup>5</sup> which may represent a real part of the frequency of the mode that is predicted by a kinetic theory treatment.<sup>6</sup> Computing the precursor period in this way gives a value of  $35\mu s$  compared to the experimental value of about  $30\mu s$ .

### B. Magnetic Oscillations

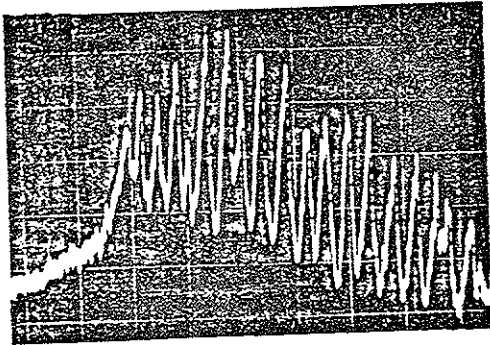
Under the same operating conditions as shown in figure 5-5 except for  $I_p$ , no magnetic precursors are seen for the  $\langle q \rangle < 2$  case. In figure 6-4a chord 4 of the SXR side array is shown. In figure 6-4b the signal to a poloidal magnetic field probe for the same sawtooth as 6-4a is shown. The tip of the probe was 11cm below the midplane and on the midcylinder. Again the frequencies below 10 kHz are filtered out, and the upper frequency response is 300 kHz. Figure 6-5a shows a detail of the SXR sawtooth, the small oscillation seen just before the disruption is probably the 1/1 mode. The corresponding probe signal is shown in figure 6-5b; very little magnetic precursor is seen.

### C. $q < 2$ and the Lack of 2/1 Disruptions

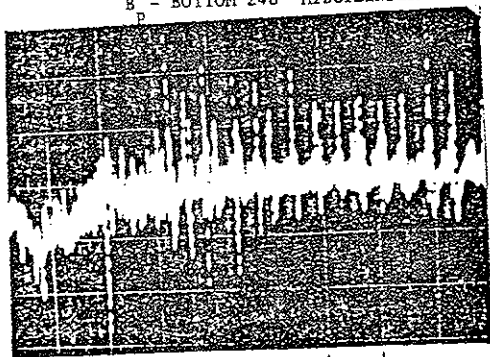
The large 1/1 precursor oscillations seen for this case, and the lack of observable 2/1 magnetic precursors, suggest that the elimination of the large sawtooth oscillations as  $I_p$  is increased (figure 4-2) may be the result of the stabilization or elimination of the 2/1 mode, and hence the disruption associated with this mode. Other tokamaks<sup>7,8,9</sup> operated below  $q_{edge}=2$  observe a positive spike on the driving voltage as  $q_{edge}$  passes through 2, subsequently no 2/1 oscillations or associated disruptions are seen; however 1/1 internal disruptions are still observed. In the tokamaks operated below  $q_{edge}=2$ , a conducting boundary was close to

FIG. 6-4. Bursts of oscillations on magnetic field pick up loops at every SXR sawtooth: (a) sawtooth oscillations on the central chord detector (4) of the side SXR array; (b) the signal from a poloidal magnetic field pick up loop located 11cm below the midplane on the midcylinder.

CENTRAL CHORD SXR - SIDE 60°



(a)

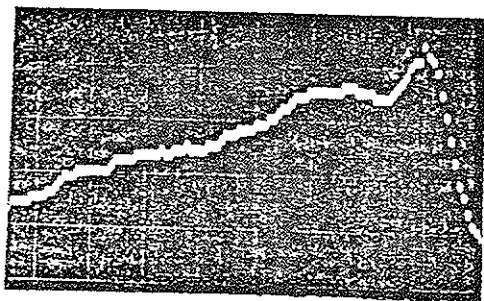
 $\vec{B}_p$  - BOTTOM 240° MIDCYLINDER

(b)

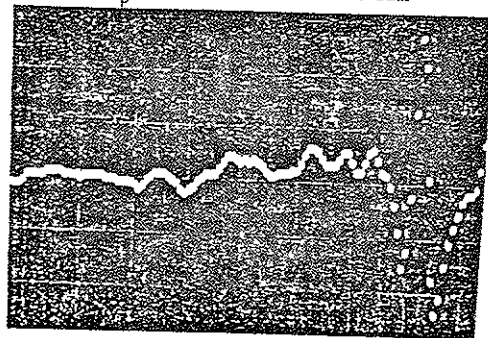
500  $\mu$ s

FIG. 6-5. No clear precursor oscillations are seen on the poloidal magnetic field pick up loops (b) for the sawtooth oscillations (a).

CENTRAL CHORD SXR - SIDE 60°



(a)

 $B_p$  - BOTTOM 240° MIDCYLINDER

(b)

12.5  $\mu$ s

the plasma edge. In Tokapole II, no conducting boundary exists near the separatrix; however, as  $I_p$  is increased, the  $q=2$  surface moves closer to the separatrix.

The  $q$  profile for this case was estimated using an MHD equilibrium code<sup>10</sup> matched to the plasma conditions. The inputs to the code were  $I_p$  and  $I_{rings}$  as determined by the current monitor circuitry,<sup>11</sup>  $B_\phi$  determined from electronically integrating the toroidal gap voltage, and the position of the inversion radii for the sawtooth oscillations. It was assumed that the SXR inversion radius corresponded to the  $q=1$  surface. A single parameter in the code determined the degree to which the plasma current was peaked; this parameter was adjusted until the inversion radius of the sawteeth matched the  $q=1$  surface. The  $\langle \beta \rangle$  values of these plasmas are so low that thermal pressure does not appreciably affect the equilibrium. The equilibrium determined in this way is shown in figure 6-6. The  $q$  profile for this case is shown in figure 6-7; the  $q=2$  surface is very near the separatrix.

Because the SXR signals are chordal averages, a chord passing through the  $q=1$  surface sees mostly plasma for which the temperature goes up during the disruption. In order for the SXR signal to show a drop, its chord must pass somewhat to the inside of the  $q=1$  surface. This effect would, however, tend to lower the  $q$  profile even more, resulting in a  $q=2$  surface even closer to the separatrix.



FIG. 6-6. Poloidal flux plot obtained from fit of  $q=1$  surface determined from the position of the sawtooth inversion and gross plasma parameters. The angles shown in the figure are the position of the  $q=1$  surface; the inversion radius of the sawtooth oscillations was  $\pm 14^\circ$  from the side, and  $18^\circ$  out and  $5^\circ$  in from the top.

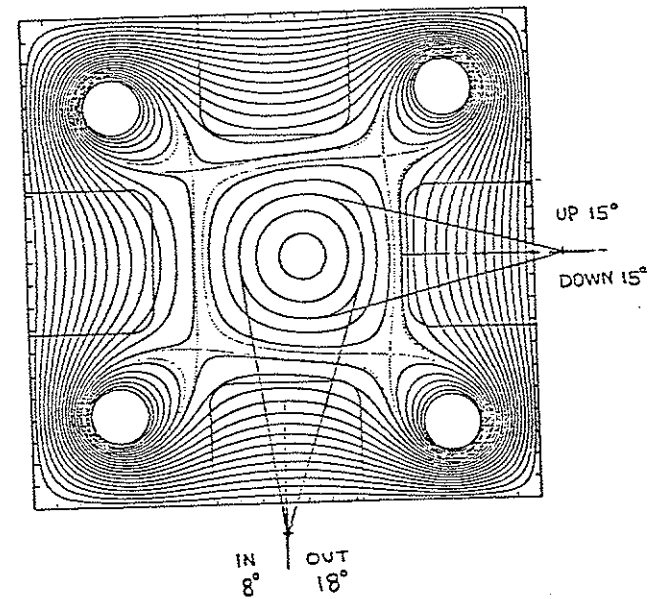
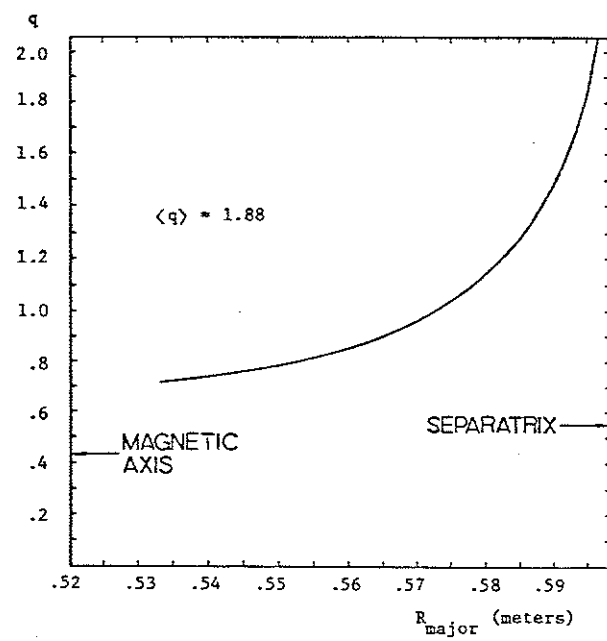


FIG. 6-7.  $q$  profile obtained from the flux plot of figure 6-6 gives a position for the  $q=2$  surface that is, near the separatrix.



Although a large 1/1 component is seen in the SXR and no obvious 2/1 mode is observed on the magnetic signals, perhaps the disruption is actually the result of an unobserved  $m > 1$  mode. In other tokamaks, a 1/1 mode is often seen in association with the predominant 2/1 mode before a disruption.<sup>11,12</sup> In such cases the inversion radius for the SXR sawtooth is usually at the  $q=2$  surface or between the  $q=1$  and  $q=2$  surfaces. A careful examination of chords 2 and 6 in figure 6-2a suggests the presence of an additional mode at large minor radius; however, if these disruptions are associated with an  $m > 1$  mode it would be very difficult to match the inner inversion radius as viewed from the bottom SXR detector. This is because, in order to move the inversion radius to a higher  $q$ , the current profile must be substantially flattened, shifting the minor axis inwards in major radius. For these plasma conditions, it is rather likely that these disruptions are the result of a simple 1/1 mode.

No detailed attempt has been made to understand the reason for the apparent elimination of the 2/1 disruption for the high  $I_p$  good confinement discharges. One possibility is that, in the vicinity of the separatrix, the 2/1 mode is linearly stable, or saturates at a low level. Linear stability seems unlikely since, for small island widths, the stability is dominated by local effects near the reconnection layer where the geometry of the flux surfaces is relatively unimportant. The current density gradient near the separatrix is relatively steep even for the case without the baffle

plates inserted; thus, the mode would be expected to be destabilized by moving the  $q=2$  surface closer to the separatrix as seen in other machines. A calculation in Tokapole II geometry would be necessary, however, to test linear stability. Near the separatrix the magnetic shear scale length,  $(d\ln q/dr)^{-1}$ , could be small compared to the reconnection layer width. This is a possibility not normally included in resistive MHD theory. Since the mode draws on flux between the  $q=2$  surface and the separatrix during the reconnection, if the  $q=2$  surface is sufficiently close to the separatrix, then the flux supply will be exhausted while the 2/1 island is still small. What happens at this point is somewhat uncertain; if the 2/1 perturbation continues to grow, the outer surfaces of the island will probably become ergodic. This situation will be discussed in more detail in chapter 8 in the context of the 1/1 mode. The HIB<sup>13</sup> code could be used to test the consequences of this possibility. Still another interesting possibility is that the region near the separatrix is always ergodic. This might be due to some nonaxisymmetric error in the placement of the divertor rings (a fairly likely possibility), or the close proximity of many low order mode rational surfaces in this region might lead to overlap of several small islands and ergodization. The experimental results of Yoshida, et al., indicate that the 2/1 disruption can be suppressed with a 3/1 external winding that ergodizes the 2/1 island magnetic surfaces.<sup>14</sup>

The question remains as to how the the  $q=2$  surface gets to the separatrix, since the  $q=2$  surface probably moves from the center outwards as the current is increased. The current ramp up in Tokapole II is rapid relative to other tokamaks, because of the large initial driving voltages. Rapid current ramp up seems to be one avenue to  $q_{\text{edge}} < 2$  in other devices.<sup>7,14</sup> Independent control of the rate of the current rise and the plateau value was not possible during the course of this research.

References for Chapter 6

- <sup>1</sup>B.V. Waddell, M.N. Rosenbluth, D.A. Monticello, R.B. White, Nucl. Fusion, 16, 528 (1976).
- <sup>2</sup>K. McGuire, D. Robinson, Nucl. Fusion, 19 505 (1979).
- <sup>3</sup>N.S. Brickhouse, private communication.
- <sup>4</sup>F.L. Hinton and R.D. Hazeltine, Reviews of Modern Phys., 48, 239 (1976).
- <sup>5</sup>C.L. Jahns, M. Soler, B.V. Waddell, J.D. Callen, H.R. Hicks, Nucl. Fusion, 18, 609 (1978).
- <sup>6</sup>J.F. Drake, UCLA Report PPG-335, (1978).
- <sup>7</sup>DIVA Group, Nucl. Fusion, 20, 271 (1980).
- <sup>8</sup>T. Edlington, J.L. Luxon, T.N. Todd, D.C. Robinson, in Plasma Physics and Controlled Thermonuclear Fusion Research (Proc. 9th Int. Conf. Baltimore 1982),
- <sup>9</sup>M.W. Phillips, University of Wisconsin-PLP 765 (1978).
- <sup>10</sup>J.C. Sprott, University of Wisconsin-PLP 889 (1983).
- <sup>11</sup>Equipe TFR, Nucl. Fusion, 17, 1283 (1977).
- <sup>12</sup>N.R. Sauthoff, S. von Goeler, W. Stodiek, Nucl. Fusion, 18, 1445 (1978).
- <sup>13</sup>R. Izzo, et al., Phys. Fluids, 26, 2240 (1983).
- <sup>14</sup>Z. Yoshida, et al., in Plasma Physics and Controlled Thermonuclear Fusion Research (Proc. 9th Int. Conf. Baltimore 1982), 3, 273 (1982).

## CHAPTER 7

DATA AND ANALYSIS FOR  $\langle q \rangle = 1.0^1$ 

The sawtooth oscillations in the  $\langle q \rangle = 1.0$  discharges do not show obvious precursor oscillations on either magnetic pick up loops or SXR detectors. However, the crash of the sawtooth itself exhibits phase shifts between different SXR detectors that have an  $m=n=1$  structure. In most other tokamaks in which this question has been addressed, the sawtooth crash of the 1/1 disruption was poloidally and toroidally symmetric ( $n=m=0$ ). A helical phase shift of the sawtooth crash is consistent with what would be expected in the Kadomtsev model of the disruption in which only the 1/1 mode is involved. The symmetry of the disruption in other devices may be the result of the formation of an ergodic region produced by the interaction of a number of higher order modes driven by the current spike (equation 2.12) at the reconnection point of the 1/1. The low S value of  $\langle q \rangle = 1.0$  discharges in Tokapole II may limit the current density gradient at this spike, and allow a nearly pure 1/1 mode to continue through the nonlinear phase of the instability.

A. Soft X-Ray Data

As mentioned in chapter 3, the  $\langle q \rangle < 1$  cases are operated with the quarter sine wave  $v_{pg}$ . This is necessary because the energy confinement of these discharges is low,  $\tau_E < 50\mu s$ . A typical

overall SXR trace for this case is shown in figure 7-1a for chord 4, and in figure 7-1b for chord 2. Precursor oscillations are not observed; however, the crash of the sawtooth itself propagates in a helical  $m=n=1$  structure following the field line pitch. For 18 of 45 sawteeth studied, the sawtooth crash propagated upwards at side  $60^\circ$  array; in other words, the sawtooth falls first at the bottom detector, then at the central chord, and finally at the top detector (figure 7-2a). The maximum time delay between detectors is about 45  $\mu s$ . For these sawteeth the relative phase of tiltable SXR detectors at top  $150^\circ$  ( $90^\circ$  away from the side array in toroidal angle) and side  $240^\circ$  ( $180^\circ$  away in toroidal angle) indicated that the crash propagated inward in major radius at top  $150^\circ$  and downward at side  $240^\circ$  (figure 7-2b). This is consistent with an  $m=n=1$  structure following the Tokapole II field line pitch (figure 6-3). Reversing the toroidal field reversed the direction of propagation of the top  $150^\circ$  detector. In one case, the time delay of the side array is much smaller than the 45  $\mu s$  of the previous cases; however, for this case the tilted detector at bottom  $240^\circ$  shows that the crash propagates from in to out, indicating that the time delay is still approximately the same, even though the propagation direction varies from sawtooth to sawtooth. For 3 of the sawteeth studied the direction of propagation was downward on the side  $60^\circ$  array. The other cases appear to propagate in random order with respect to the side array, with the central chord never being the first to crash. The

FIG. 7-1. Typical overall SXR signals for central chord (a) and edge (b) detectors in the side array.

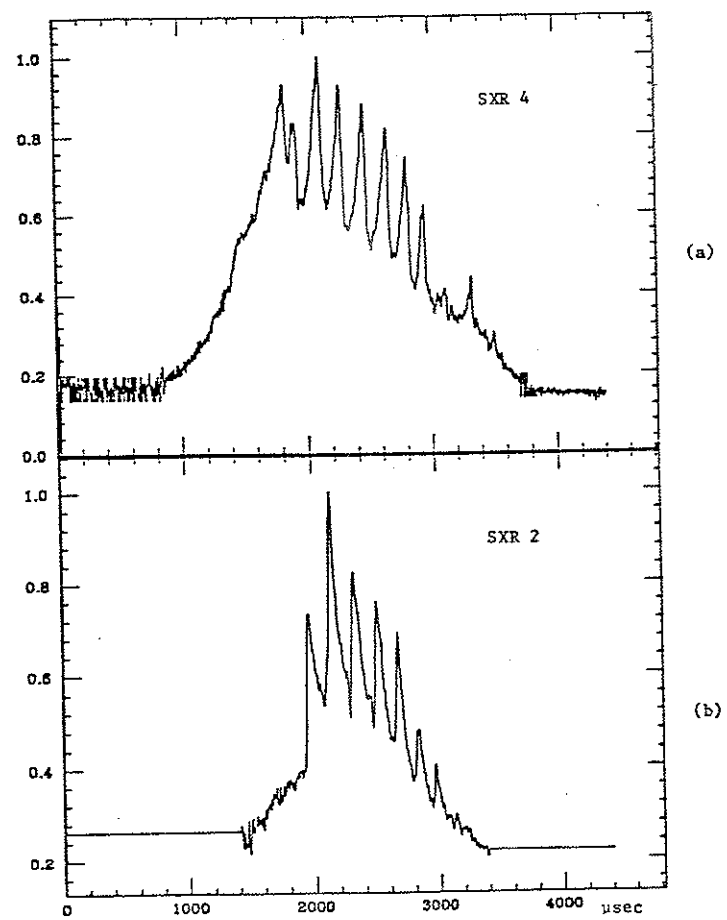
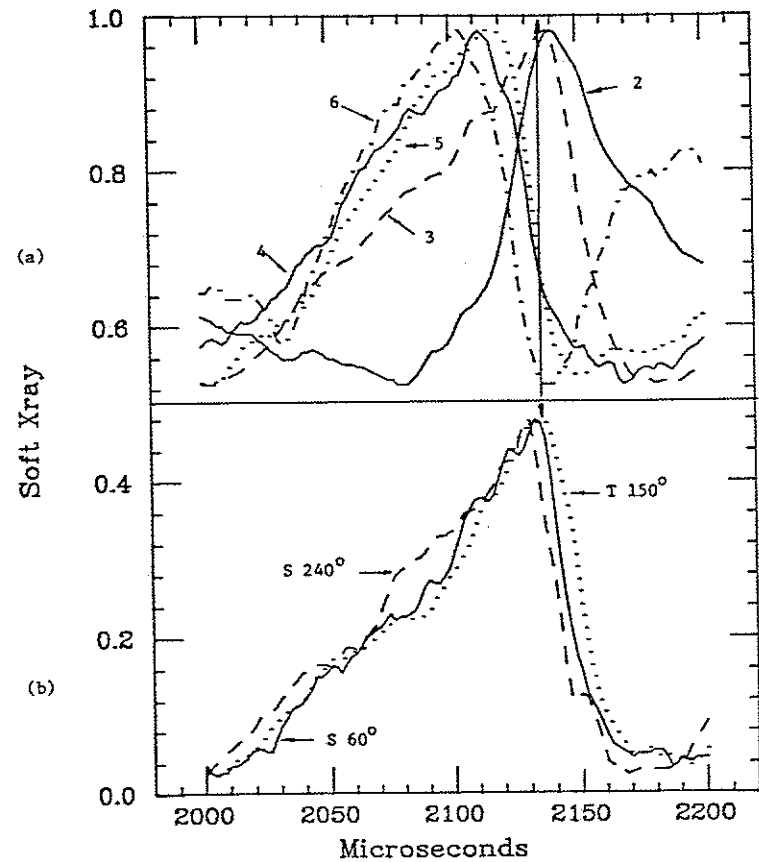


FIG. 7-2. Typical upward propagation of sawtooth crash in the side SXR detector signals (a); phase correlation of signals to toroidally displaced detectors (b) indicate a constant phase of the sawtooth crash along a field line on the  $q=1$  surface (figure 6-3). The side  $60^\circ$  detector is tilted up  $7^\circ$ ; the top  $150^\circ$  detector is tilted  $4^\circ$  inward toward the major axis; the side  $240^\circ$  detector is tilted  $7^\circ$  down.



tendency for the sawtooth to propagate upwards at side  $60^\circ$  occurs even for the reversed  $B_{tor}$  case; possibly, this tendency is the result of field errors, and may relate to the fact that most Tokapole II plasmas sit below the midplane.

### B. Interpretation of Disruption Phase Shift

It does not seem likely that the phase shift described above represents a diffusive process, since the character of the crash is more convective than diffusive. The fall rate of a sawtooth on the side array detectors is similar, rather than progressively more rounded for detectors falling later.

The propagation of the disruption may be the result of the growth of a 1/1 mode without rotation. If for some reason, such as an error in the equilibrium fields, the reconnection point of the magnetic island was preferentially above the midplane at the location of the side SXR array, then the chords below the midplane would be looking through flux surfaces on which the temperature drops first due to reconnection (figure 7-3). Since the hot central part of the plasma would be displaced upward in this instability, the upper chords would fall progressively later. An unusual feature of these discharges is that, because of the large driving voltage, the ohmic heating time ( $60\mu s$ ) is comparable to the sawtooth period ( $200\mu s$ ) and the disruption time ( $40\mu s$ ). This might explain the observation that the lower chords begin to rise again before the upper chords drop.

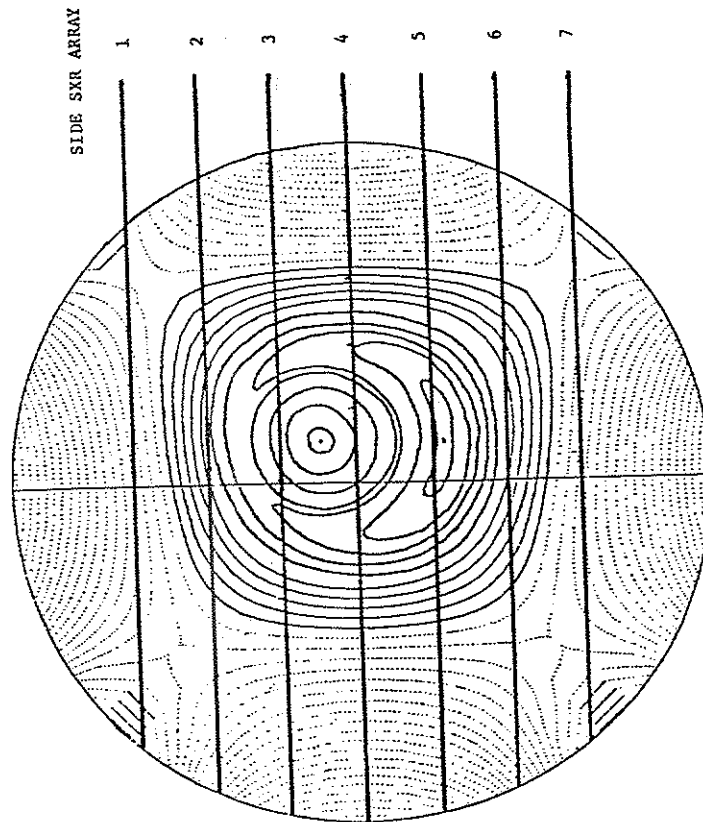
FIG. 7-3. Growth of a 1/1 island may produce the observed propagation of the sawtooth crash. SXR chords of the side array are shown superimposed on a resistive MHD code result in which a 1/1 island occurred.



The helical structure of the 1/1 disruption in Tokapole II may be a unique example of the classic Kadomtsev flip<sup>2</sup> as described in chapter 2. In other experiments<sup>3</sup> the disruption itself is toroidally and poloidally symmetric ( $m=n=0$ ), although the precursor oscillations exhibit the 1/1 structure. An alternate theory,<sup>4,5</sup> that accounts for 0/0 structure of the disruption, is based on the fact that the singular current that is generated by the reconnection can drive other higher order tearing modes.<sup>6</sup> The overlap of these higher order islands produces an ergodic region that first forms near the island separatrix and then propagates symmetrically inward and outward. The current density gradient which drives these higher order modes can be estimated from equations 2.11-2.13.

$$\frac{j_s}{\delta} = \frac{v_A^* B^*}{a \eta} = -S \frac{J_\phi}{a} \quad (7.1)$$

Since the  $S$  value for the  $\langle q \rangle \approx 1$  discharges is approximately 5000, while for large tokamaks  $S$  can be as large as  $10^6$ , the current density gradient of the reconnection induced current is expected to be a factor of 200 smaller than in large tokamaks. This may inhibit the production of the axisymmetric turbulent region and allow the 1/1 structure of the mode to persist through the nonlinear stage. In an NIB run for a very low  $q$  plasma with  $S=5000$  and spatially constant resistivity, although some smaller island



chains were formed along the 1/1 island separatrix, the mode continued to grow in the classic Kadomtsev fashion until the topology was flipped (figure 7-5).

The lack of rotation for this case may be the result of the small temperature gradient as inferred from the SXR profile. Estimates of the diamagnetic frequency<sup>7</sup> give values close to the 40 $\mu$ s disruption time.

References for Chapter 7

- <sup>1</sup>T.H. Osborne and N.S. Brickhouse, University of Wisconsin-PLP 908, (1983).
- <sup>2</sup>B.B. Kadomtsev, Sov. J. Plasma Phys., 1, 389 (1975).
- <sup>3</sup>G.L. Jahns, M. Soler, B.V. Waddell, J.D. Callen, H.R. Hicks, Nucl. Fusion, 18, 609 (1978).
- <sup>5</sup>M. Dubois, and A. Samain, Nucl. Fusion, 20, 1101 (1980).
- <sup>6</sup>M. Dubois, A.L. Pecquet, C. Reverdin, Nucl. Fusion, 23, 147 (1983).
- <sup>7</sup>N.S. Brickhouse, private communication.

## CHAPTER 8

DATA AND ANALYSIS FOR  $\langle q \rangle < 1.0$ 

Discharges with central  $q$  values as low as 0.5 are routinely obtained. Although these discharges exhibit sawtooth oscillations, the central  $q$  values do not relax to 1. In the usual Kadomtsev picture in which reconnection of helical flux proceeds to the original magnetic axis, the central  $q$  values would be expected to relax to 1 during the disruption. This result might be explained if the growth of the  $1/1$  mode saturated before the reconnection was complete. Although the poloidal divertor geometry appears to provide a topological constraint that would limit the growth of the  $1/1$  mode if the  $q=1$  surface is located near the separatrix, resistive MHD code results do not agree with this model. Some resistive MHD code runs show an apparent saturation of the instability. However, this saturation occurred well after the interaction of the mode with magnetic flux outside the separatrix began. If reconnection in the experimentally observed disruptions had proceeded to the extent obtained for these code runs, the experimentally determined  $q$  values after saturation would have been near 1. Another resistive MHD code run developed in the usual way, with the island  $o$ -point becoming the magnetic axis. The factors which determine the extent to which the instability will proceed have not yet been determined.

A.  $q < 1$  Discharge General Characteristics

For  $B_\phi < 3\text{kG}$  and the quarter sine wave form of  $V_{pg}$ , discharges with central  $q$  values as low as 0.4 are readily produced. The time evolution of the  $q$  profile for such a discharge is shown in figure 8-1. For almost all of the  $\langle q \rangle < 1$  discharges, the  $q$  profiles, determined from the probe measurements, are flat across most of the region within the separatrix, turning up sharply at the separatrix (where formally  $q \rightarrow \infty$ ). Although central  $q$  values as low as 0.5 have been observed, the most common value was 0.7.

Table 8-1 summarizes the characteristics of the discharges for which the magnetic probe data was taken to determine  $q$ . Low  $q$  discharges were obtained for both D, inverse D, and square cross sections. There appears to be no preferred shape of the  $q$  profile at the time when  $q$  goes through 1;  $q$  profiles that increased with minor radius, decreased with minor radius, or were more or less flat were observed. The time at which the first sawtooth occurs is usually between the time when  $q$  goes through 1 and the time when  $q$  reaches its minimum value.

There is a tendency for the sawtooth period to become smaller as  $B_\phi$  is lowered, with  $V_{pg}$ , and density held constant. The period of the sawteeth can drop from  $200\mu\text{s}$  to  $50\mu\text{s}$  as  $B_\phi$  is decreased by less than a factor of 2. Based on the scaling  $B_\phi \sim I_p$ , obtained for this type of scan, and described in more detail in section F, the

FIG. 8-1. Typical time evolution of  $q$  profile as the plasma current increases.

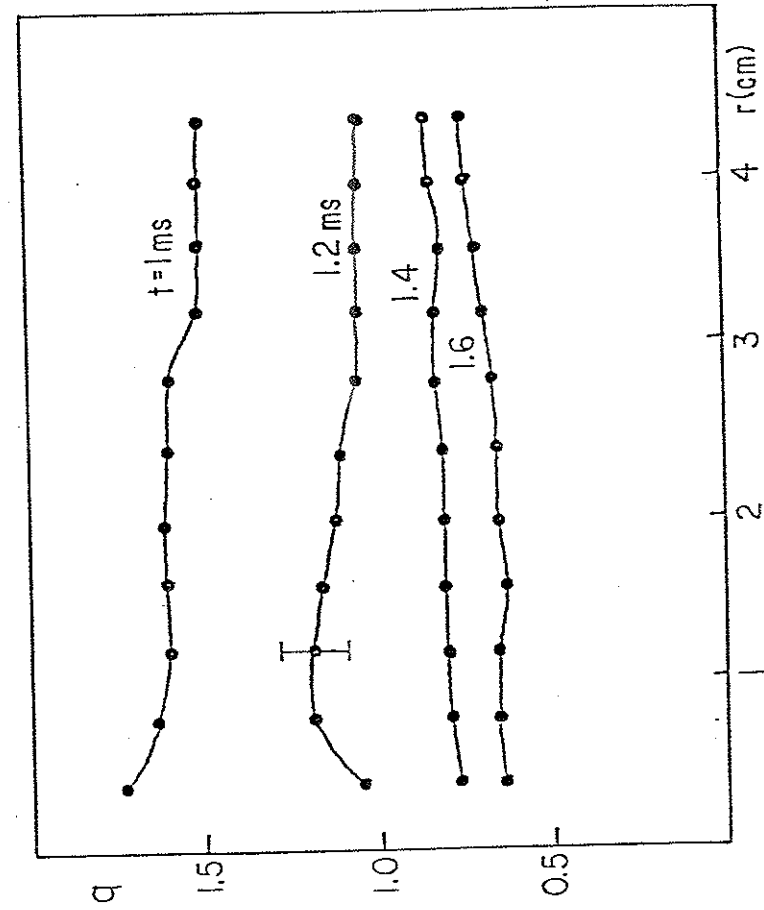


Table 8-1. Low q discharge characteristics. Column 1 indicates whether the plasma cross section shape was an inverse D (ID), square (S) or D;  $q_{min}$  is the minimum q value attained in the plasma;  $t_1$  is the time after the poloidal field capacitor bank was fired that q passed through 1;  $t_2$  is the time at which the first sawtooth crash occurred; column 6 indicates if the q profile was flat (F), had a minimum at the minor axis (P), or had a maximum at the magnetic axis (I);  $t_4$  is the time at which the plasma reached its minimum q value.

Table 8-1

Case		$q_m$	$t_1$	$t_2$	$t_3$	
2/15/80	ID	1.0	1350 $\mu$ s	1400 $\mu$ s		F
3/7/80	ID	0.6	1450 $\mu$ s	1500 $\mu$ s	F	1600 $\mu$ s
3/9/80*	ID	0.6	1800 $\mu$ s	2150 $\mu$ s	P	2200 $\mu$ s
4/15/80	S	0.7	1600 $\mu$ s	1750 $\mu$ s	P	1800 $\mu$ s
4/20/80*	D	1.0	1600 $\mu$ s	1700 $\mu$ s		I
8/4/80	S	0.7				
9/2/80	D	0.5				
2/21/81	D	0.6	1350 $\mu$ s	1650 $\mu$ s	P	1900 $\mu$ s
7/31/81	ID	0.7				
11/10/81	S	0.8	1850 $\mu$ s	2000 $\mu$ s	F	2200 $\mu$ s

\*Limiter plates inserted.

sawtooth period (equation 6.3) should be a very weak function of  $B_\phi$ ,

$$\tau_{st} \sim B_\phi^{0.1} . \quad (8.1)$$

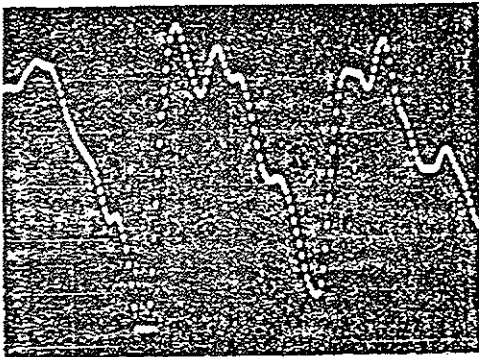
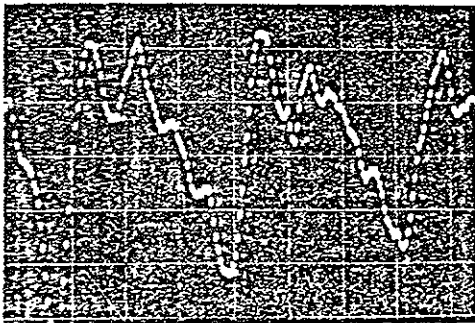
Also, as  $B_\phi$  is lowered, the sawtooth crash becomes progressively more rounded off. At very low  $B_\phi$  (roughly  $q < 0.5$ ), instead of sawteeth, a highly distorted 1/1 mode is observed on unintegrated magnetic pickup loops (figure 8-2). This transition to an oscillating helical mode at very low  $q$  is similar to observations on DIVA.<sup>3</sup> Integration of the signals in figure 8-2 produces a scallop like magnetic field signal.

The shortening of the sawtooth period greatly beyond what would be predicted from equation 8.1, and the gradual rounding of the sawtooth crash, with the appearance of a nearly pure 1/1 mode at  $q < 0.5$ , may indicate that a fundamental change in the nature of the mode occurs as  $B_\phi$  is lowered, which might be consistent with the observation that  $q$  does not relax to 1 during the sawtooth.

#### B. Connection of Sawtooth Oscillations to $q=1$

No direct observation of a helical structure has been made in the  $q=0.7$  discharges for which the magnetic probe determinations of  $q$  were done. Several facts, however, suggest a connection between the sawtooth oscillations and the 1/1 mode. In the  $\langle q \rangle = 1$  case (chapter 7), the sawtooth crash itself shows a 1/1 helical

FIG. 8-2. Distorted 1/1 mode observed on poloidal magnetic field pick up loops at  $q < 0.5$ .

$\vec{B}_p$  TOP 330°

 $\vec{B}_p$  TOP 150°


 20  $\mu$ s

structure. For  $q < 0.5$ , the distorted 1/1 mode is observed on magnetic pickup loops. The association of a 1/1 helical mode in cases with  $q$  above and below 0.7 suggests that the sawtooth oscillations in the  $q=0.7$  cases are related to a 1/1 mode as well.

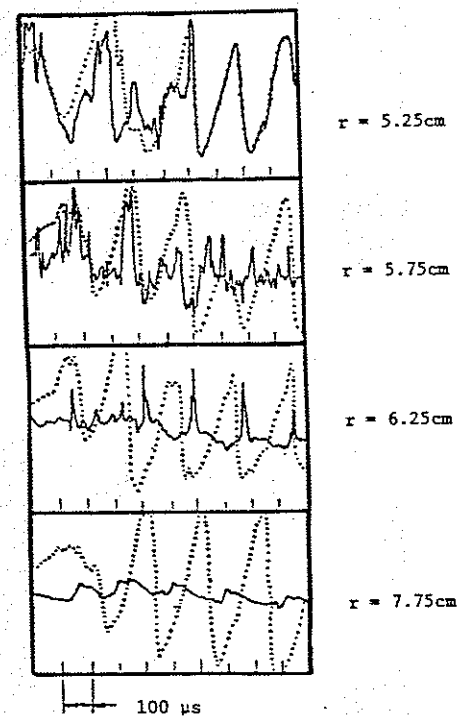
The position of the inversion radius of the sawtooth oscillations occurs near the  $q=1$  surface; this also suggests an association with a 1/1 mode. Figure 8-3 shows the results of a Langmuir probe scan along the midplane, for the case of 7/31/81 (Table 8-1). This probe is sensitive to  $n_e(T_e)^{1/2}$ , and shows an inversion within 1 cm of the  $q=1$  surface. The inversion radius as determined from a scan with a SXR detector is about 2 cm inside the radius determined from the Langmuir probe scan; this is probably attributable to line averaging effects. The accuracy of this data is not sufficient, however, to distinguish an inversion at the  $q=1$  surface from one at a  $q > 1$  surface (e.g.  $q=2$ ), between the  $q=1$  surface and the separatrix.

Another datum suggestive of a correlation between  $q=1$  and the sawtooth oscillations for the  $q=0.7$  cases is that the first sawtooth normally occurs sometime after the  $q=1$  surface enters the plasma, but before  $q$  reaches its minimum value (table 8-1).

### C. q Oscillations During a Sawtooth

During sawtooth activity as observed on the SXR arrays, similar signals are seen on magnetic probes. A typical poloidal field signal from a magnetic pickup loop on the midplane near the

FIG. 8-3. Sawtooth oscillations observed on a Langmuir probe biased to collect ion saturation current show an inversion near the  $q=1$  surface. The minor radii shown are measured from the magnetic axis of the flux plot at the sawtooth peak determined from the magnetic probe measurements shown in figure 8-8; the  $q=1$  for this case (figure 8-7) is at  $r = 6\text{cm}$ .





separatrix is shown in figure 8-4; sawtooth oscillations of  $\approx 15\%$  of the peak value can be seen. The poloidal field data was first analyzed to produce the maximum possible change in  $q$  during a sawtooth, independent of the absolute phase relation of the sawtooth oscillations between different points in the data grid. This was done by using the poloidal magnetic field values, for a given grid point, at times that were within one sawtooth period of a chosen time, for which the magnitude of the poloidal field was a maximum and a minimum. The flux plots obtained in this way for the case of 7/31/81 are shown in figure 8-5. The  $q$  profiles determined from this analysis (figure 8-6) show that the maximum possible  $q$  during the sawtooth oscillation is still significantly less than 1.

As mentioned in section B, there is indirect evidence of a correlation between a 1/1 perturbation and the instabilities observed at  $q=0.7$ ; also, the time scales for the disruptive phase of the sawteeth in these discharges (10 to 20 $\mu$ s) is consistent with estimates based on the resistive MHD model (equation 2.16). These facts suggest that low mode number, resistive MHD is applicable to the sawtooth oscillations in the  $q=0.7$  case. If the sawtooth oscillations were the result of a 1/1 mode in which the reconnection proceeded to the original magnetic axis, then the current density would have been flattened and  $q$  raised to 1 everywhere.<sup>4</sup> Moreover, if  $q$  was somehow relaxing to 1 during the instability, it seems unlikely that  $q$  could return to values of 0.7 during the sawtooth ramp up. This return to low  $q$  would take an

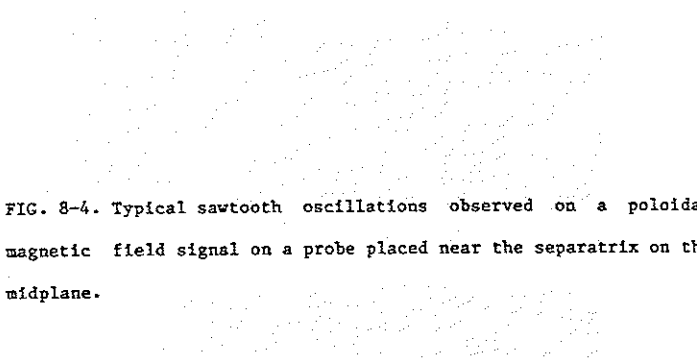


FIG. 8-4. Typical sawtooth oscillations observed on a poloidal magnetic field signal on a probe placed near the separatrix on the midplane.

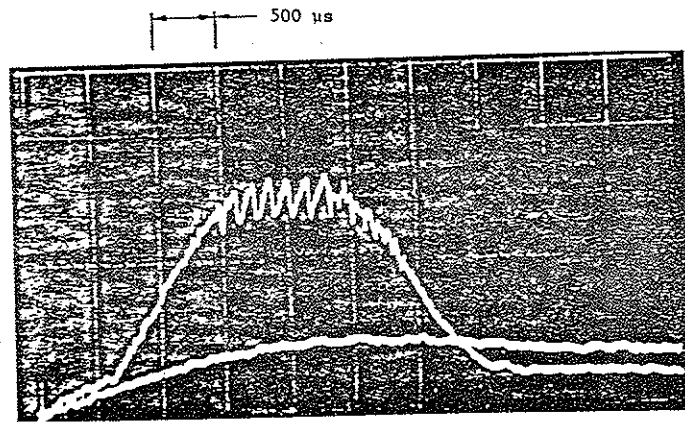


FIG. 8-5. Flux plots determined from the magnetic probe data in which the value of the poloidal field at each point in the data grid is taken at a time such that the sawtooth oscillation makes the magnitude of the field a maximum (a), and a minimum (b).

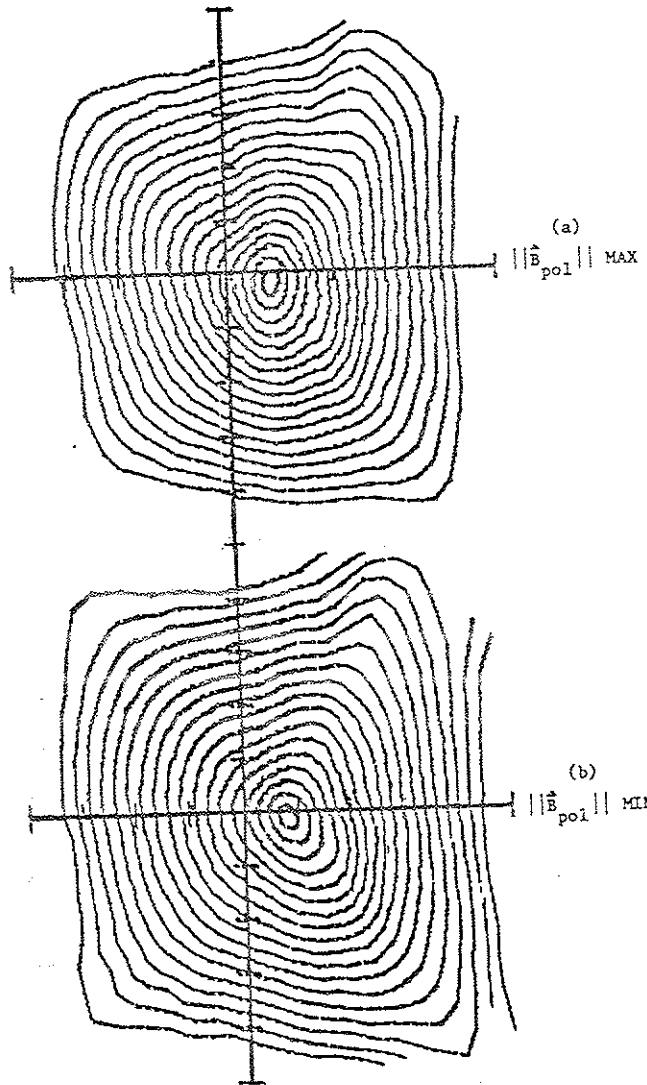
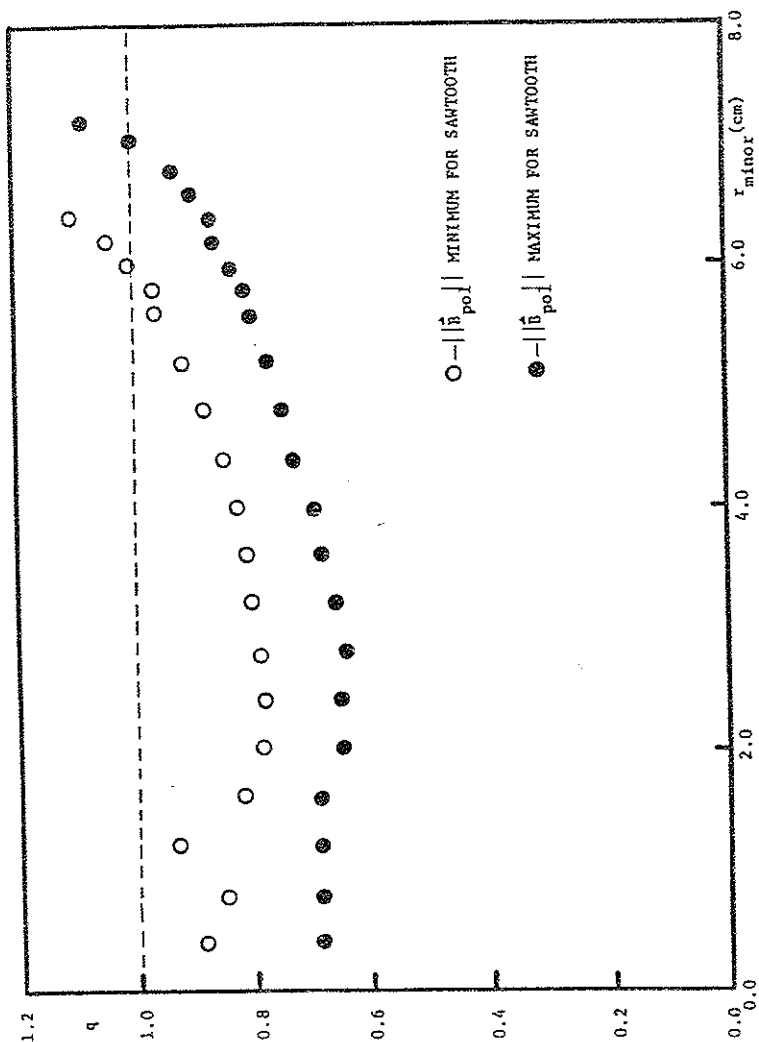


FIG. 8-6.  $q$  profiles determined from the magnetic probe data in which the value of the poloidal field at each point in the data grid is taken at a time such that the sawtooth oscillation makes the magnitude of the field a maximum (a), and a minimum (b). These represent the maximum  $q$  oscillation that can be obtained from the data due to the sawtooth oscillations.



L/R time, which is determined from circuit parameters<sup>5</sup> to be  $\approx 2\text{ms}$ , while the sawtooth period is only  $\approx 100\mu\text{s}$ .

In order to establish a correlation of the sawtooth phase between data grid points, a phase reference signal was also taken. In one case the midplane SXR was used as a phase reference, while in all others the poloidal magnetic field on the midplane at 8 cm from the machine midcylinder was used. A magnetic signal was used for phase reference because, at the time, only a very low signal to noise ratio was available on the SXR signals, and also because the magnetic relaxations seemed to be less perturbed by the presence of the probe (this was thought to be a consequence of the fact that the usual tearing mode picture predicted that the instability was fundamentally magnetic).

The  $q$  profile, obtained using the poloidal magnetic field at the separatrix as the phase reference, for the case of 7/31/81 shows no oscillation for the central values, with a small oscillation localized to the region near the separatrix (figure 8-7). The  $q$  values for sawtooth peak are plotted at the minor radius at which the same flux value occurred in the plot for the sawtooth valley. The flux plots generated at the sawtooth valley and peak, relative to this phase reference signal, are shown in figure 8-8a and 8-8b respectively. If the current density profile was flattened by the disruption, as would be expected for a 1/1 mode that flipped the magnetic topology, the equilibrium obtained after the disruption should have been shifted inwards in major

FIG. 6-7.  $q$  profiles at a sawtooth peak and valley relative to a phase reference signal show only an oscillation in the edge  $q$  values.

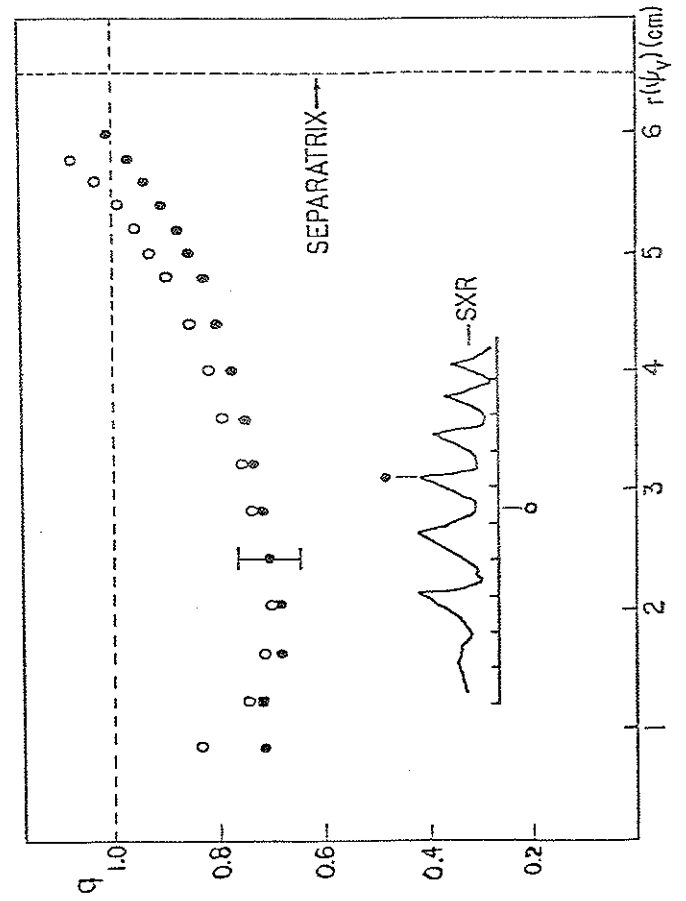
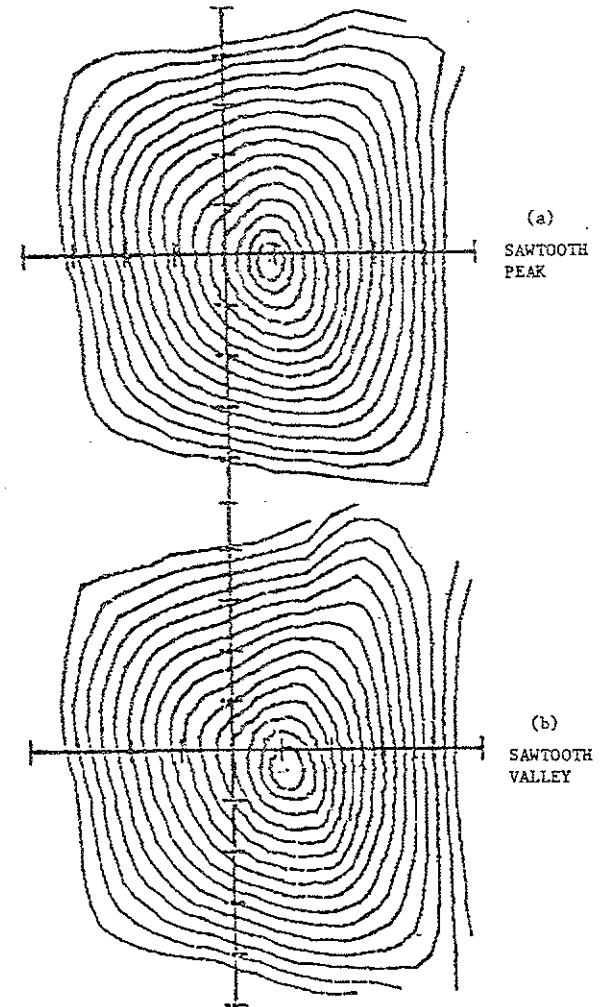


FIG. 8-8. Flux plots at a sawtooth valley (b) relative to a phase reference signal show a slight outward shift and a more inverse D shape than those for the peak (a).



radius because of the decrease in plasma inductance; instead, the flux plot at the sawtooth peak (figure 8-8a) is located at a somewhat smaller minor radius than the valley (figure 8-8b). These features repeat on subsequent sawtooth oscillations.

The phase-correlated  $q$  profiles of figure 8-7 do not reflect the maximum possible change in the central  $q$  values shown in figure 8-6, because the sawtooth peaks and valleys on the phase reference signal may not coincide with the beginning and end of the disruption. The times chosen for the phase-correlated  $q$  profiles and flux plots then would represent an intermediate phase in the development of the instability. The sawtooth crash on other tokamaks is axisymmetric.<sup>1,2</sup> The SXR data for the  $\langle q \rangle = 1$  case described in chapter 7, however, indicate non-axisymmetric temperature relaxations. No correlation has, as yet, been made between the degree of toroidal asymmetry and other parameters (although there is some indication that the sawteeth become less toroidally symmetric as the sawtooth period is shortened). Toroidal symmetry of the sawtooth oscillations was not checked for every case in which magnetic probe data was time-correlated with a phase reference signal. In those cases for which a check was made a phase shift in the sawtooth crash on the order of that observed in the  $\langle q \rangle = 1$  case cannot be ruled out.

If the plasma is not axisymmetric at the time when the flux surfaces and  $q$  values are determined by the techniques of chapter 3, the flux surfaces will not coincide with the magnetic surfaces

(surfaces in which the field lines lie), nor will the  $q$  values determined in this way represent the actual  $q$  values for the magnetic surfaces as defined by equation 2.2. Under the assumptions of long toroidal wavelength, low  $\beta$ , resistive MHD discussed in the appendix to this thesis, the poloidal magnetic field data obtained at one toroidal azimuth and time-correlated with the phase reference signal can still provide information on the development of the current density profile during the instability.

As noted in the appendix,  $\vec{B}$  can always be written as,

$$\vec{B} = R_0 \nabla \psi \times \nabla \phi + \vec{b}_{3\perp} + R B_\phi \nabla \phi, \quad (8.2)$$

where  $\perp$  denotes the components in the poloidal plane. The time for the propagation of a compressional Alfvén wave in  $B_\phi$  across the poloidal cross section is short compared to the growth times of the instabilities. This limits perturbations of  $B_\phi$  to be of order  $\epsilon^2 = (a/R_0)^2$ , and keeps the toroidal field divergence free to order  $\epsilon^3$ . Because of this fact,  $\vec{b}_{3\perp}$  will be maintained  $O(\epsilon^3)$  throughout the development of the instability, so that the poloidal field can be written as,

$$\vec{B}_\perp = R_0 \nabla \psi \times \nabla \phi + O(\epsilon^3 B_\phi). \quad (8.3)$$

When a helical perturbation is present,  $\phi$  in the above equation is

a function of  $\phi$ ; however, the  $\phi$  derivatives of  $\psi$  do not enter equation 8.3 so that at a given toroidal azimuth,  $\phi_0$ ,

$$\vec{B}_1(\phi_0) = R_0 \nabla \psi(\phi_0) \times \nabla \phi + O(\epsilon^2 B_\phi). \quad (8.4)$$

If the phase reference signal corresponds not only to a particular point in the progress of the reconnection, but also to a particular orientation of the helical perturbation, then  $\psi$  in equation 8.4 is proportional to the flux function defined in chapter 3. The  $\langle q \rangle = 1$  results indicate that there may be a preferred orientation for the helical mode. The toroidal current at  $\phi_0$  is related to  $\psi(\phi_0)$  in the same way as in an axisymmetric toroidal system,

$$\Delta^* \psi = \frac{1}{R} \frac{\partial \psi}{\partial R} - \frac{1}{R^2} \frac{\partial^2 \psi}{\partial R^2} = - \frac{R}{R_0} J_\phi. \quad (8.5)$$

Thus, if the above assumptions apply, the  $q$  profiles obtained with the phase-reference signal (figure 8-7) are those for a toroidally symmetric system with  $J_\phi$  given by  $J_\phi$  at the toroidal azimuth where the measurements were made. If the phase-correlated poloidal field data represents a particular phase in the reconnection but a random orientation of the helical perturbation, then the poloidal field data may not be divergence free. If this is true, then the  $\psi$  contours constructed as specified in chapter 3 are not unique and depend on the choice of a minor axis; and the  $q$  profiles would then

correspond to some average over different orientations of the perturbed current density.

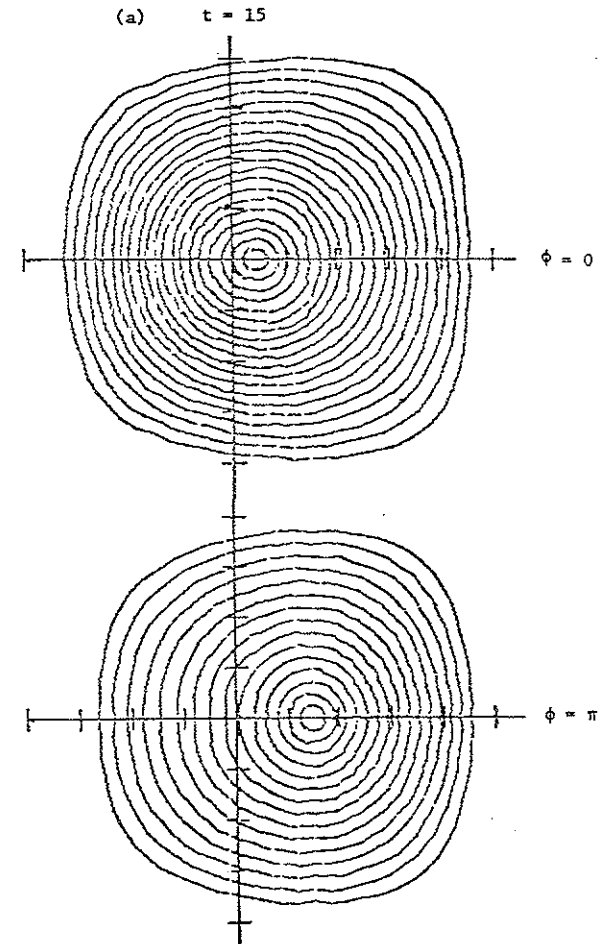
To simulate these phase effects, output of the HIB code that showed a 1/1 disruption was used to generate magnetic field data for input into the program used to produce the  $\psi$  contours and  $q$  profiles. This was done for different fixed orientations of the magnetic island and for a case in which each point in the data grid corresponded to a random orientation of the mode. The results of this simulation (figure 8-9) show that the experimentally measured  $q$  values would have responded to the flattening of the current profile by the 1/1 mode, and that a complete reconnection would have raised the experimentally determined  $q$  values to 1 regardless of the interpretation of the phase information. Also, a fluctuation in the edge  $q$  values can be obtained for different fixed orientations of the magnetic island that is similar to that obtained experimentally (figure 8-7). The shifts of the  $\psi$  surfaces corresponding to this oscillation are also consistent with the observations (figure 8-8).

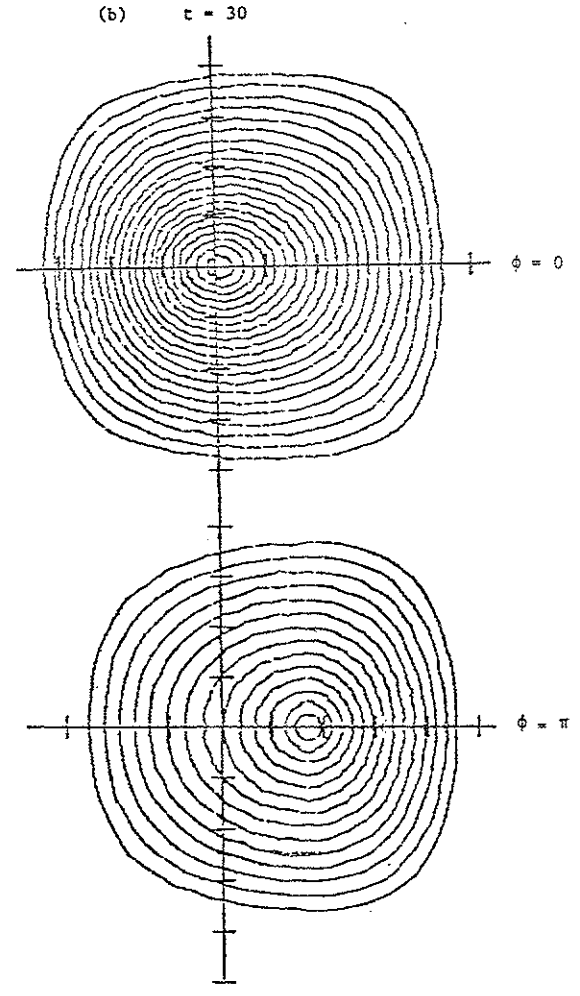
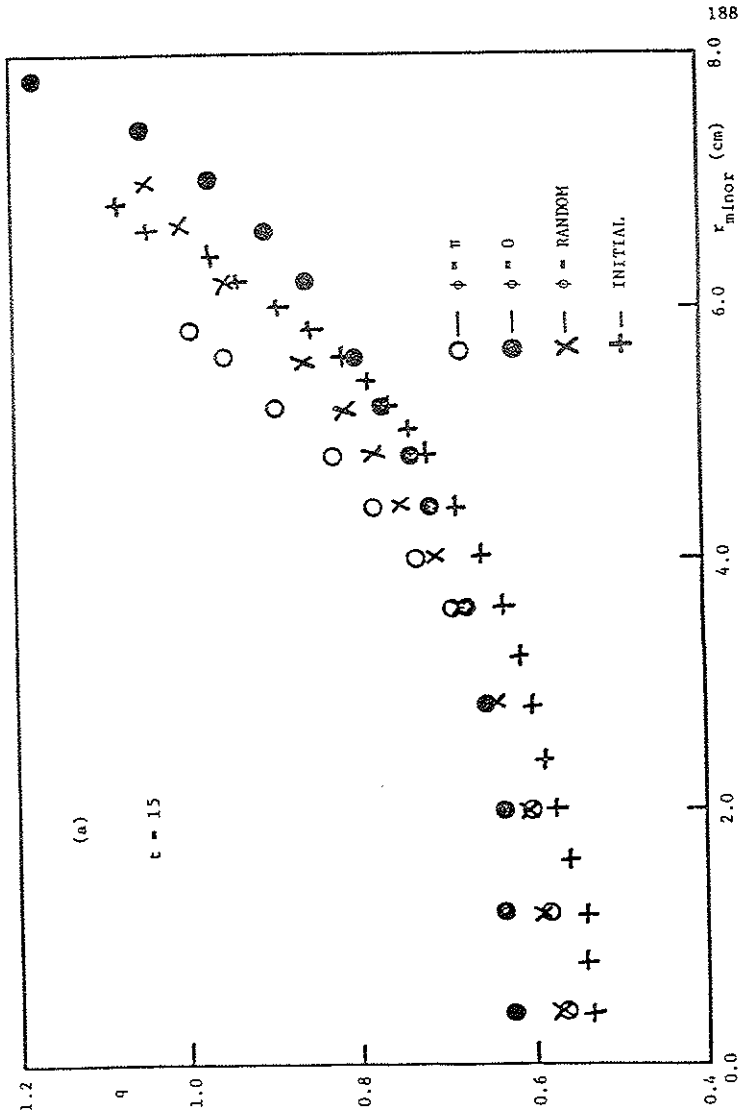
#### D. Heuristic Model for Partial Reconnection

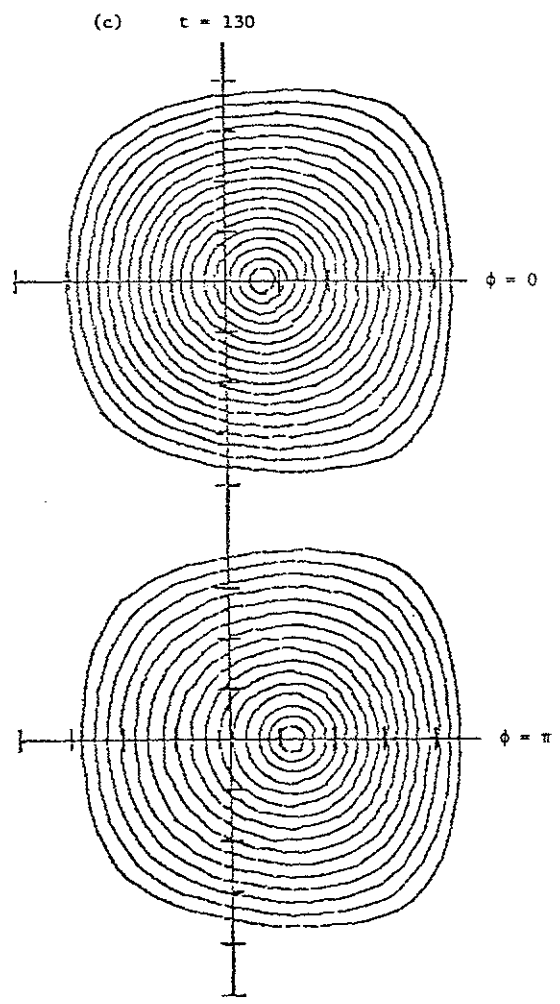
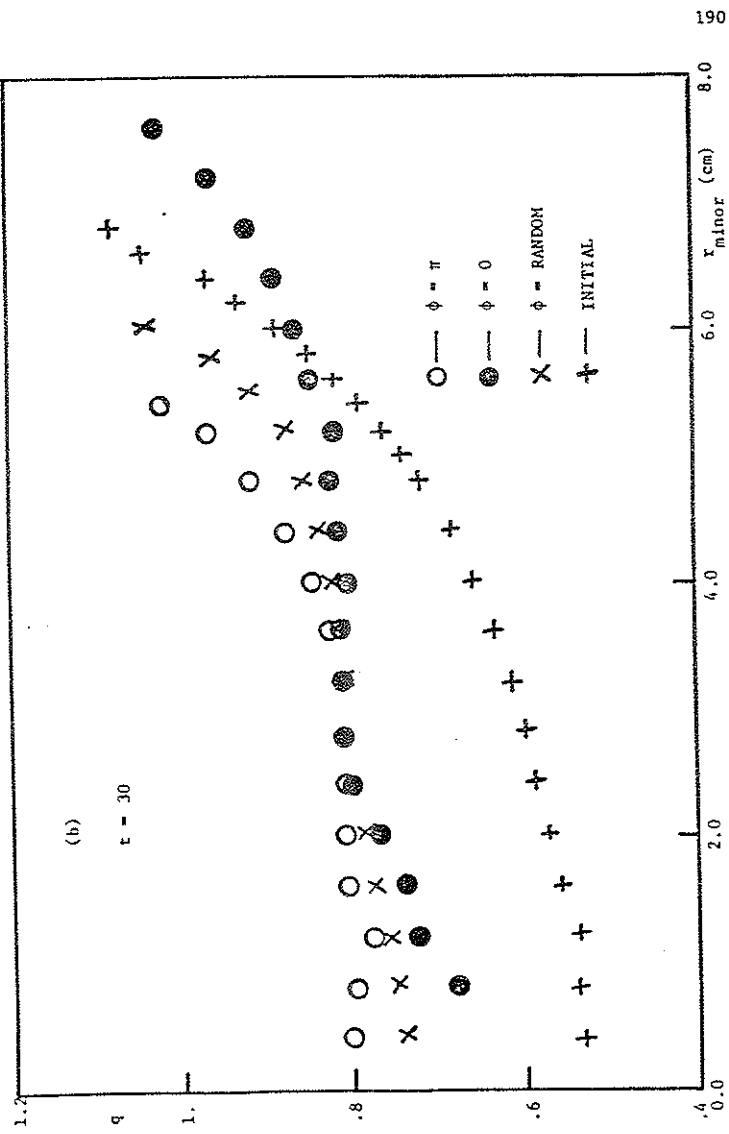
In the standard picture of the disruption associated with the 1/1 mode,<sup>4</sup> the instability flattens the current profile, raising  $q$  above 1 everywhere. As discussed in section B, there are several reasons to believe that the instability for the  $q=0.7$  case may be associated with a 1/1 mode. The  $q$  profile data, however, do not

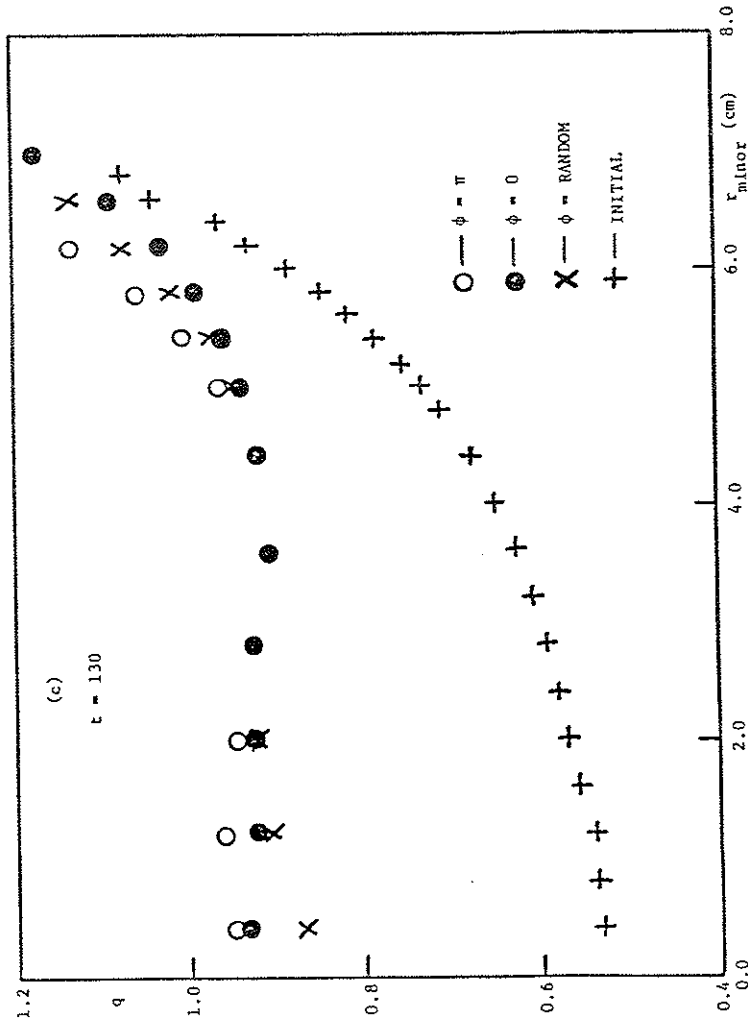


FIG. 8-9. Simulation of the effects of the nonaxisymmetry expected during the development of the 1/1 disruption, using the output of a resistive MHD code run shown in figure (8-14), show that the  $q$  profiles respond to the overall current density change, and that an oscillation in the edge  $q$  values can result from different orientations of the magnetic island. The times correspond to those of the code run. Although the resistive MHD code run did not fully reconnect, the current density was flattened sufficiently to raise  $q$  to near 1. For each time point two flux plots are shown corresponding to having the kinked magnetic axis on the inside ( $\phi = 0$ ) and outside ( $\phi = \pi$ ) of the equilibrium magnetic axis in a particular poloidal plane. "Initial" refers to the initial condition equilibrium.









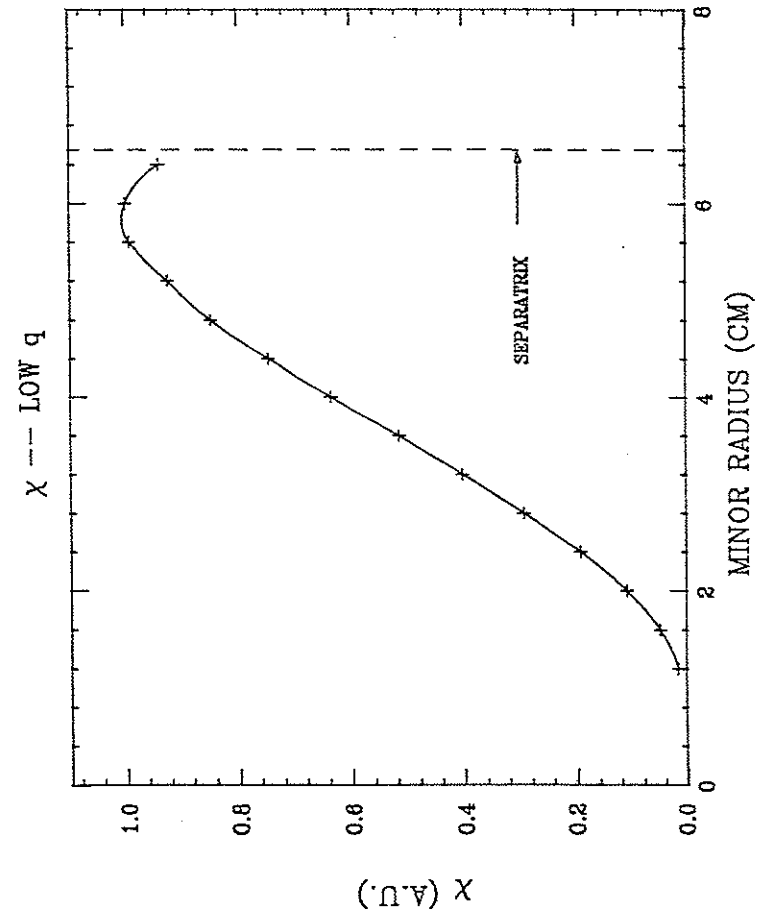
show the expected relaxation to 1.  $q$  would not relax to 1 if the reconnection of flux were limited in extent.

Since the growth of this instability proceeds through flux reconnection, if the  $q=1$  surface is close enough to the separatrix, the flux supply within the separatrix will be exhausted before the 1/1 mode flips the topology. If the separatrix were a conducting boundary, this depletion of the helical flux supply would stop the growth of the magnetic island.

The flux that is reconnected in the 1/1 disruption is the flux through a helical surface that contains a field line on the  $q=1$  surface and the magnetic axis. Because this helical surface wraps once around poloidally in going once around toroidally, the helical flux is just the difference between the poloidal and toroidal flux for any toroidally symmetric system. The helical flux,  $\chi$ , for the case discussed above was computed in this way for the sawtooth peak and is shown in figure 8-10. This figure shows that the helical flux within the separatrix will be exhausted before the instability has flipped the magnetic topology.

If reconnection continues beyond the separatrix, then it is topologically impossible for the simple 1/1 island structure to be maintained. In the classic Kadomtsev model, just after two magnetic surfaces reconnect, a field line on the new surface follows a path that essentially maps out the original two surfaces, except that the field line moves from one surface to the other at the island tips. If one of the original surfaces is inside the

FIG. 8-10. Helical flux function computed from the  $q$  profile at the sawtooth peak in figure 8-7 indicates that insufficient helical flux is available within the separatrix for full reconnection.

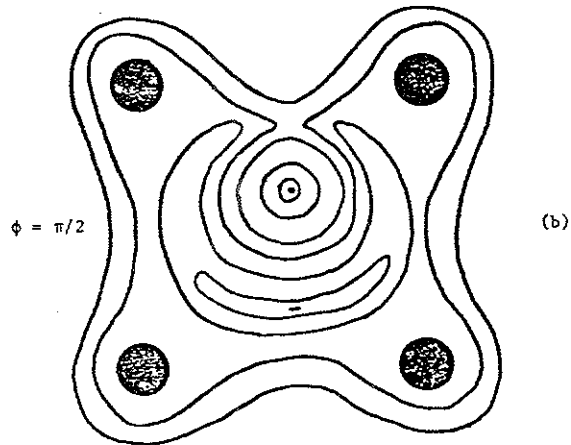
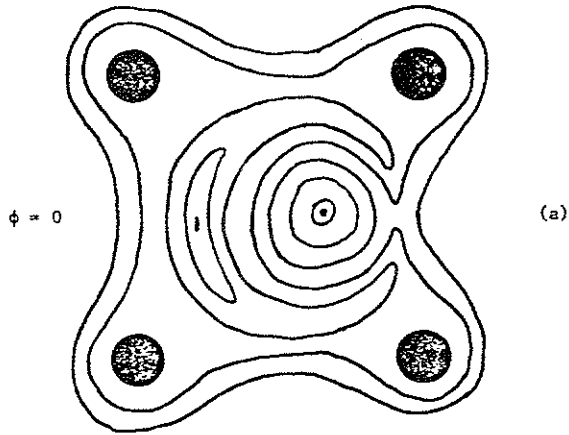


separatrix, and one outside the separatrix, then although it is possible to imagine the surface that might result at one toroidal azimuth, this pattern cannot be mapped around the torus with the helicity of the mode (figure 8-11). A possible resolution of this topological constraint is for the reconnection to proceed beyond the separatrix through the formation of an ergodic field region. This seems reasonable since the equilibrium separatrix could be thought of as an  $n=0$  island structure that might become ergodic through overlap with the  $1/1$  island, as occurs for other incommensurate modes (chapter 2). Obviously the structure of the mode would have to be modified greatly if the reconnection went beyond the separatrix; if this modification was stabilizing, the growth of the mode might be arrested.

#### E. HIB<sup>6</sup> Resistive MHD Code Results

An attempt was made to understand the low  $q$  results, and perhaps verify the possibility that the separatrix acts as a conducting wall to stop the growth of the  $1/1$  mode, within the resistive MHD model. To this end, the nonlinear reduced resistive MHD code, HIB, was provided by the Princeton Plasma Physics Laboratory. In this section  $1/1$  island,  $2/1$  island, etc. will be used to denote the islands that occur on the  $q=1$ ,  $q=2$ , etc. surfaces, respectively. Since the local  $q$ , as defined by equation 2.1, varies on a magnetic surface, so does the pitch of a magnetic island on that surface. Thus, using  $1/1$ ,  $2/1$  etc. is only

FIG. 8-11. Topological impossibility of simple  $1/1$  island growth by reconnection to flux outside the separatrix.



intended to denote the basic structure of the island, not to specify its mode numbers in terms of poloidal and toroidal angle.

A derivation of the set of reduced resistive MHD equations used in the HIB computer code is sketched in the appendix to this thesis. The reduced resistive MHD equations are an expansion of the full set of single fluid resistive MHD equations in the inverse aspect ratio  $\epsilon = a/R_0$ . The lowest order in which toroidal effects enter in the dynamical equations is  $\epsilon^3$  if  $\beta \sim \epsilon^2$ , and  $\epsilon^4$  if  $\beta \sim \epsilon$ . In the Tokapole  $\beta = 0.1\%$  and  $\epsilon = 1/7$ , so the  $\epsilon^3$  equations are applicable; this reduces the number of independent variables involved, and greatly increases the code's efficiency. The unit of time used in the code is the poloidal Alfvén time,  $\tau_{HP}$ . The fastest waves included in the reduced equations travel across the poloidal cross section in  $\tau_{HP}$ . Many of the considerations involved in the choice of an initial condition for the HIB runs were dictated by the time step that had to be used for numerical stability. The size of the time step determines if a run will take a few days or a few weeks, and thus, determines if enough runs can be done to appreciate what aspects of the initial conditions are important. For the chosen initial conditions, approximately 1 minute of computation time on the MFE Cray computer was needed to advance the equations 1 poloidal Alfvén time ( $\approx 0.24\mu\text{s}$ ); usually runs of a few hundred  $\tau_{HP}$  are required to follow the instabilities' development.

An MHD equilibrium code<sup>7</sup> was used to produce the initial condition for HIB. The original version of the equilibrium code did not allow plasma current outside the separatrix; this restriction led to some unanticipated effects in the final results related to the way HIB treats the resistivity profile. A version of the equilibrium code that allowed plasma current outside the separatrix was completed; however, the use of this equilibrium in HIB required a finer computational grid that reduced the code's efficiency, so that no runs have yet been completed.

The choice of a current density profile for the cases with no plasma current outside the separatrix was restricted by several considerations. First, if the current density profile is flat across most of the plasma cross section, then large gradients will be present near the separatrix. Since the  $q=1$  surface is located near the separatrix, it was suspected that this type of profile would produce extraneous results. Secondly, since the code Fourier analyzes in toroidal and poloidal angle (a great advantage over 3-D grids for nearly circular tokamak equilibria) the large gradients near the separatrix, for the square cross section Tokapole flux surfaces, are difficult to resolve unless many radial grids are used. The time step of the computation is restricted by numerical stability considerations to a value of  $\Delta t \sim (\Delta r)^2/S$  so that adding more radial grids can greatly reduce the code's efficiency. Finally, it was felt that the stability of the  $1/1$  mode, in contrast to  $m>1$  modes, was fairly insensitive to the current

density profile, since the free energy that drives the mode exists whenever  $q < 1$ . The question of whether the separatrix acts as a topological constraint might be answered independently of details affected by the exact form of the current density profile (e.g. growth rate). The current density profiles chosen were basically parabolic; the flux plot and current profile used as an initial condition into the code runs are shown in figure 8-12.

Another restriction of HIB is that the conducting boundary must be circular in poloidal cross section. This greatly simplifies the boundary conditions and facilitates the use of Fourier analysis. For all the completed code runs the boundary was placed at a small minor radius so that the divertor rings (which represent other, nonsimply connected conducting boundaries) were not included. By essentially placing surface currents in the wall that remain constant during the code evolution, equilibrium flux lines are allowed to pass through the boundary, but no perturbed radial field is allowed at the wall. The computational domain is shown in figure 8-13.

The  $S$  value for Tokapole low  $q$  discharges is  $\approx 5000$ . There is a great advantage to using a low  $S$  value for the HIB runs. As mentioned above, the time step needed for numerical stability is inversely proportional to  $S$ ; this is set by the parabolic form of the resistive diffusion term in the flux evolution equation. There is, however, the additional effect, mentioned in chapter 7, that the size, and inverse gradient scale length, of the current



FIG. 8-12. Equilibrium and toroidal current density profile used as an initial condition for the HIB code.

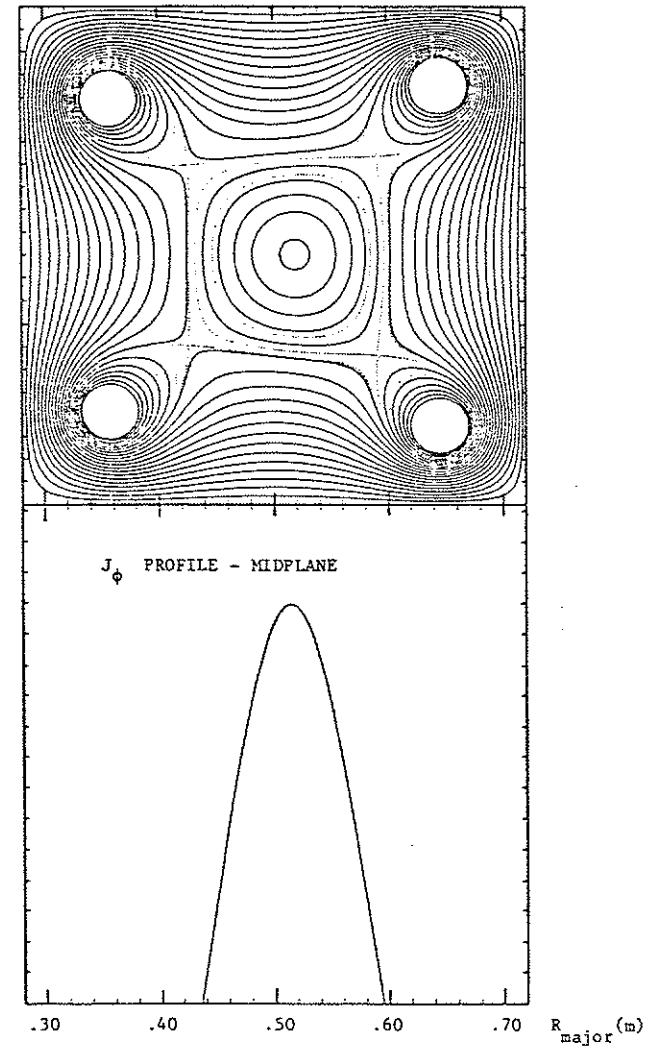
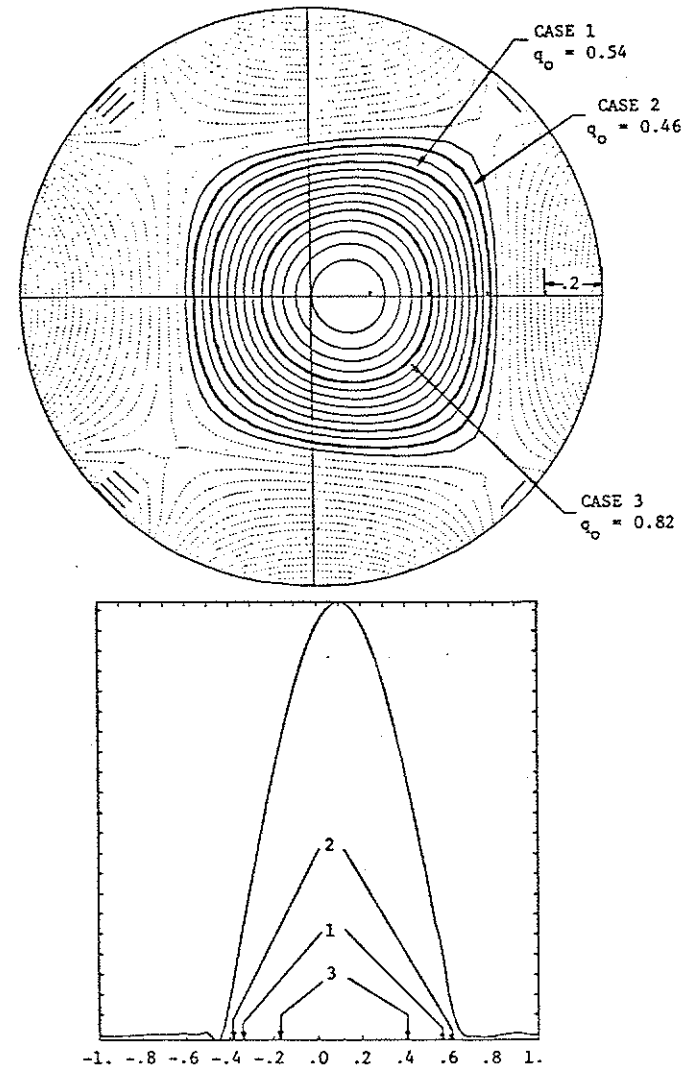


FIG. 8-13. Computational domain used in HIB code runs. The positions of the  $q=1$  surface for the three cases with  $S=1000$  are shown on the flux plot and midplane  $J_\phi$  profile.



generated at the reconnection point is proportional to  $S$ . Such a large localized current spike in a square cross section equilibrium requires many radial grids to resolve properly. This further limits the time step that can be used. A run with an  $S$  of  $10^5$  was attempted but the time step was so restrictive that no progress was made.

For three of the completed runs, an  $S$  of 1000 was used, and the resistivity profile was assumed to vary as  $1/RJ_\phi$ ; one run was completed with  $S$  of 5000 and spacially constant resistivity,  $\eta$ . The choice of  $\eta \sim 1/RJ_\phi$ , in conjunction with the proper boundary condition keeps the current density profile from resistively diffusing. The poloidal flux,  $\phi$ , is defined through

$$\vec{B}_\perp = R_0 \nabla \phi \times \nabla \psi, \quad (8.6)$$

where the  $\perp$  components are those in the poloidal plane. The toroidal current is related to  $\phi$  through  $\vec{J} = \nabla \times \vec{B}$ , or

$$RJ_\phi = -R_0 \Delta^* \phi = -R_0 \left( \nabla_\perp^2 \phi - \frac{1}{R} \frac{\partial \phi}{\partial R} \right). \quad (8.7)$$

$\phi$  satisfies the diffusion/convection equation,

$$\frac{\partial \phi}{\partial t} = -\frac{R}{R_0} \eta J_\phi + \frac{R^2}{R_0^2} \vec{B} \cdot \nabla U, \quad (8.8)$$

where  $U$  is the velocity potential defined through

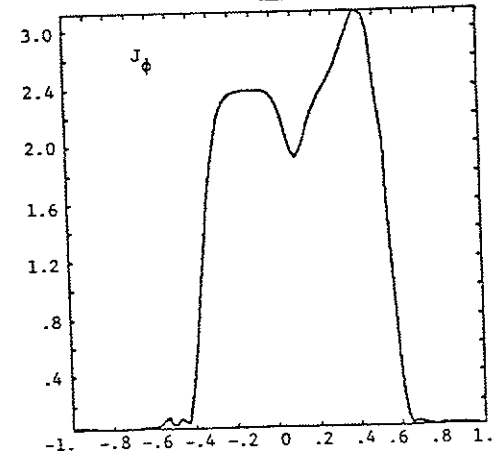
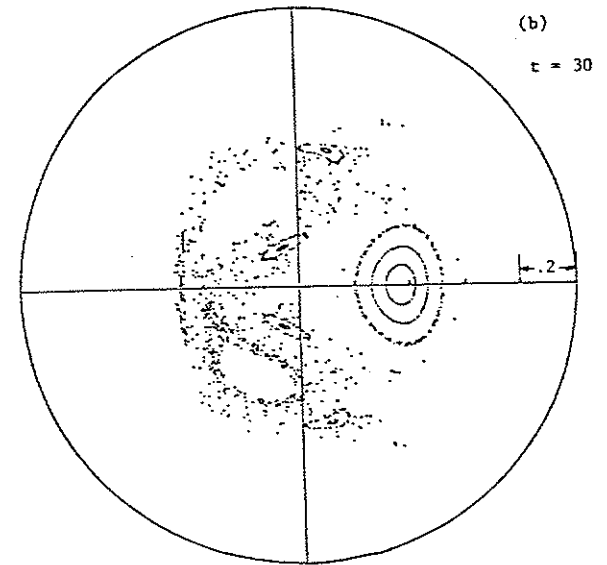
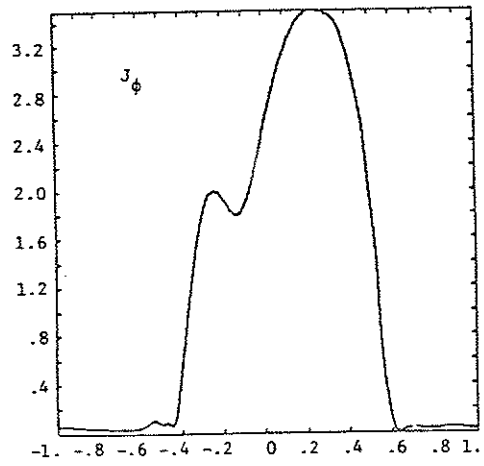
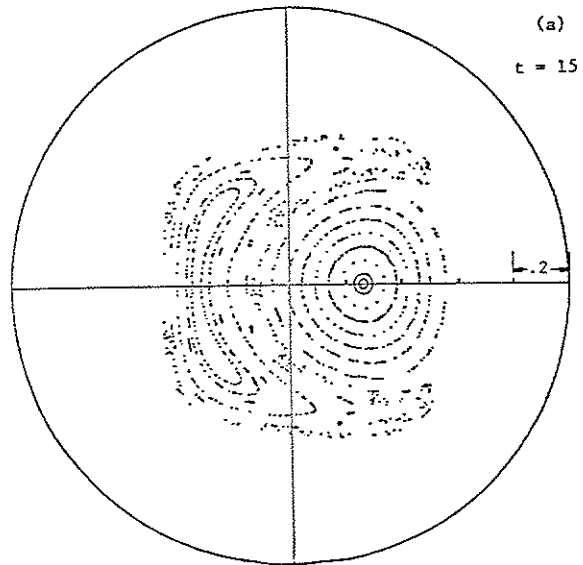
$$\vec{v}_\perp = \frac{R^2}{R_0} \nabla U \times \nabla \phi. \quad (8.9)$$

If  $\eta \sim 1/RJ_\phi$ , then the first term on the right of equation 8.8 is a spacial constant. If the wall boundary condition corresponds to a constant voltage of magnitude  $\eta RJ_\phi$ , then  $\phi = -\eta RJ_\phi t$  at  $U=0$  is a solution to equation 8.8. Flux comes in from the wall at the rate needed to compensate the resistive diffusion, and the shape of  $\phi$ , and thus of  $J_\phi$  from equation 8.7, remains constant. Using equation 6.1, the ratio of the growth time for the  $l=1$  mode to the characteristic resistive diffusion time scales as  $S^{2/3}$ . For  $S$  of 5000 and 1000 this gives a ratio of 292 and 100 respectively. If the scaling were more like  $S^{1/2}$ , as would be predicted from 2.16, the ratios would be 71 and 32 respectively. Unless  $\eta \sim 1/RJ_\phi$ , substantial diffusive change in the  $q$  profiles might occur during the development of the instability.

For  $S$  of 1000, three positions of the  $q=1$  surface were chosen to test the separatrix effects on the mode's growth (figure 8-13). In cases 1 and 2 there is insufficient helical flux between the separatrix and  $q=1$  for the mode to fully reconnect without reaching the separatrix. In case 3 the  $q=1$  surface was located at small minor radius so that full reconnection should have been possible.

The time evolution of the magnetic surfaces for cases 1 and 2 (figure 8-14 and 8-15) showed an apparent saturation of the mode before full reconnection. The saturation occurred well after reconnection to flux outside the separatrix began however, so that the lack of sufficient helical flux for full reconnection within the separatrix does not appear to limit the reconnection. Figure 8-14b and 8-15b show the magnetic surfaces and current density profiles near the saturation point; further in time, the bump in the current density that remains resistively diffuses. As this bump diffuses, new magnetic surfaces are formed which first appear out of the ergodic region near the edge of the remnant of the original magnetic surfaces as magnetic islands. The small  $m=2$  island that can be seen in figure 8-15c has a  $2/3$  structure, which indicates that this surface still has an actual  $q$  value (equation 2.2) of 0.66. The fact that reconnection to flux outside the separatrix occurred is illustrated most clearly by figure 8-15b in which a large gap exists between the remnant of the central flux region and the remnant of the  $1/1$  island. This gap results from the fact that field lines that started in this region wander out of the computational domain to encircle the divertor rings. Eventually this gap is filled in; this might be the result of flux reconnection across the equilibrium separatrix  $x$ -points. The  $q$  profiles that would have been measured experimentally at  $t=130$  for case 1 were determined as mentioned in section C. These showed

FIG. 8-14. Magnetic surfaces and current density profile evolution for case 1 with  $S=1000$ . The times given correspond to poloidal Alfvén times. (a) is near the time reconnection to flux outside the separatrix begins; (b) is near the time the mode saturates; (c) is as the plasma returns to axisymmetry.



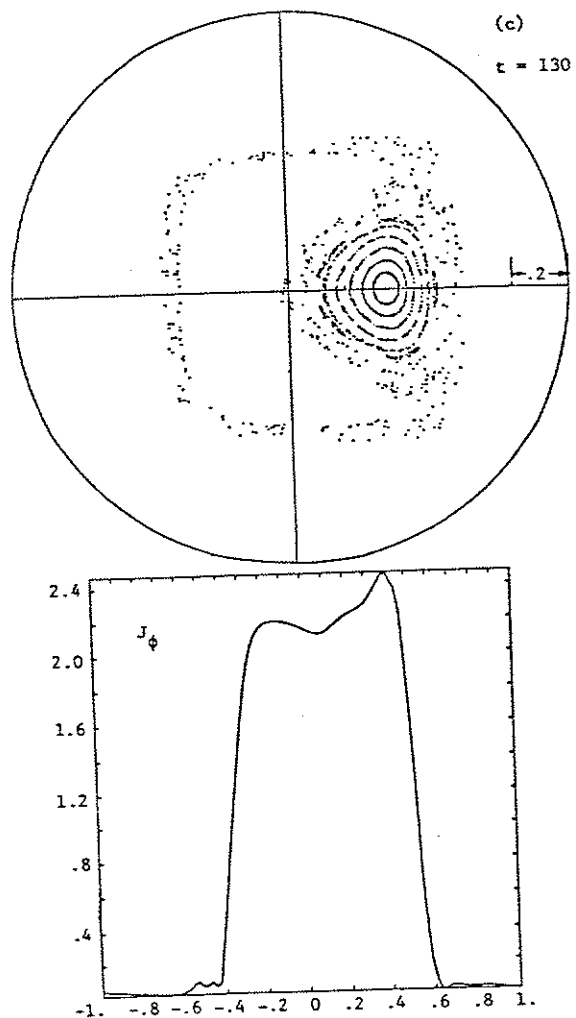
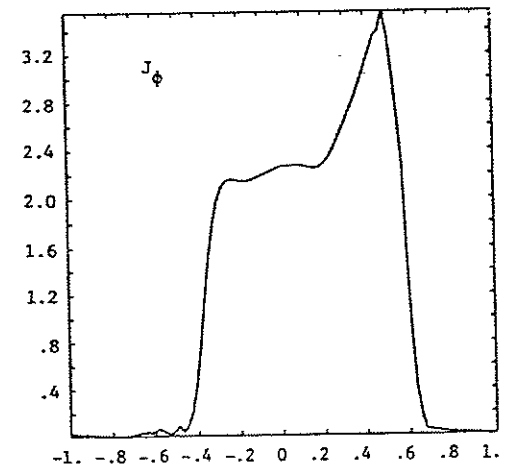
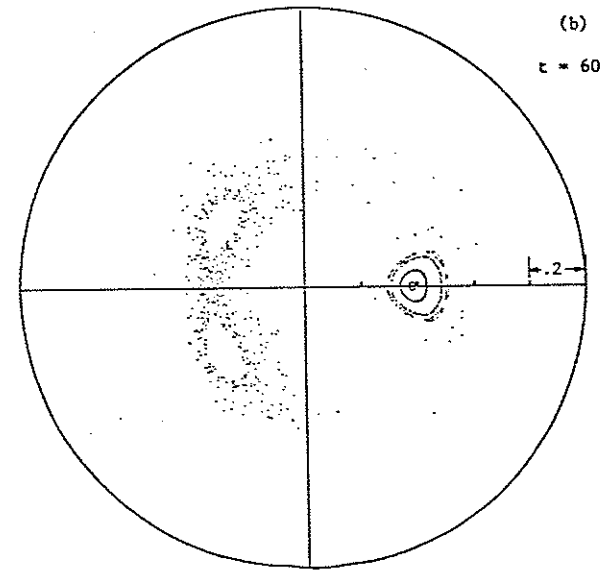
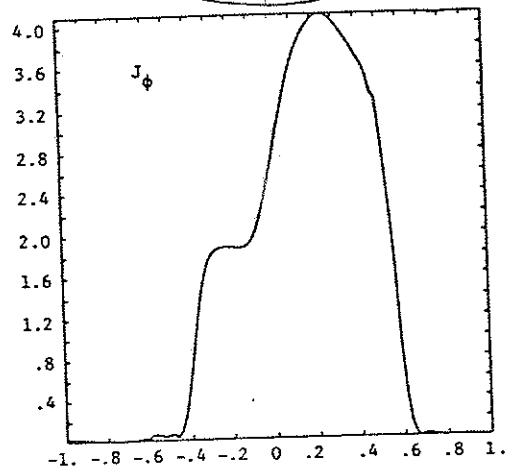
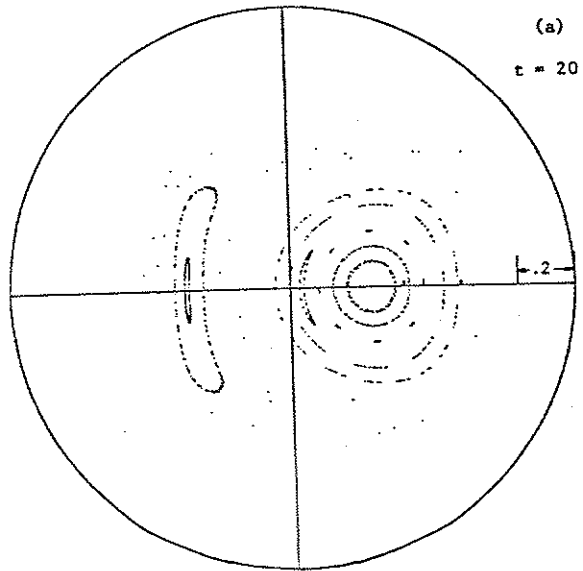
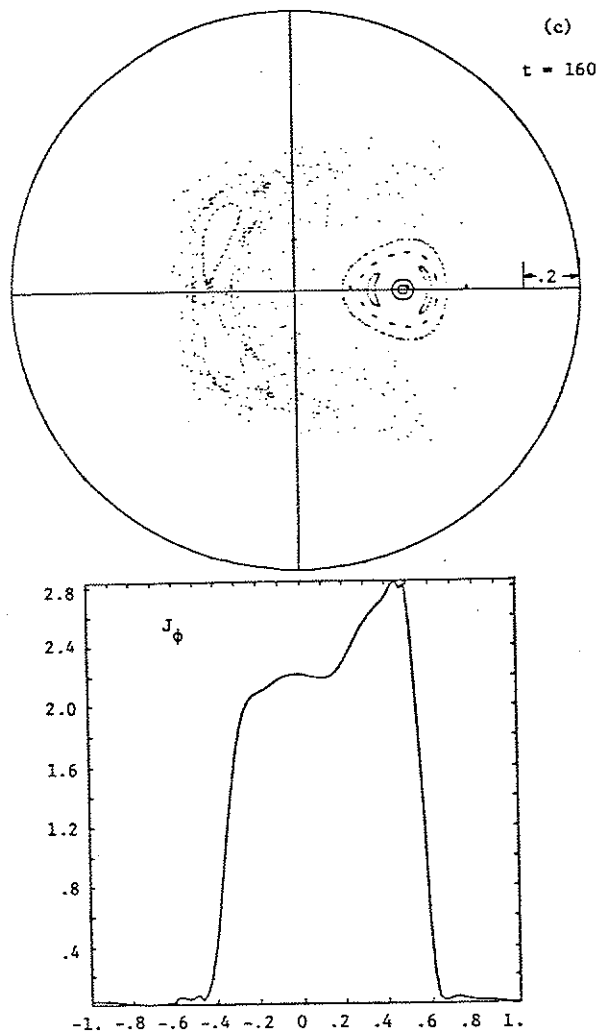


FIG. 8-15. Magnetic surfaces and current density profile evolution for case 2 with  $S=1000$ . The times given correspond to poloidal Alfvén times. (a) is near the time reconnection to flux outside the separatrix begins; (b) is near the time the mode saturates; (c) is as the plasma returns to axisymmetry.





(figure 8-9c) that although the mode seemed to saturate, the  $q$  values were raised to near 1.

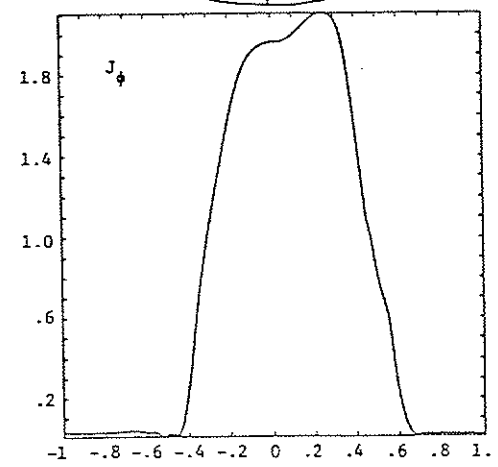
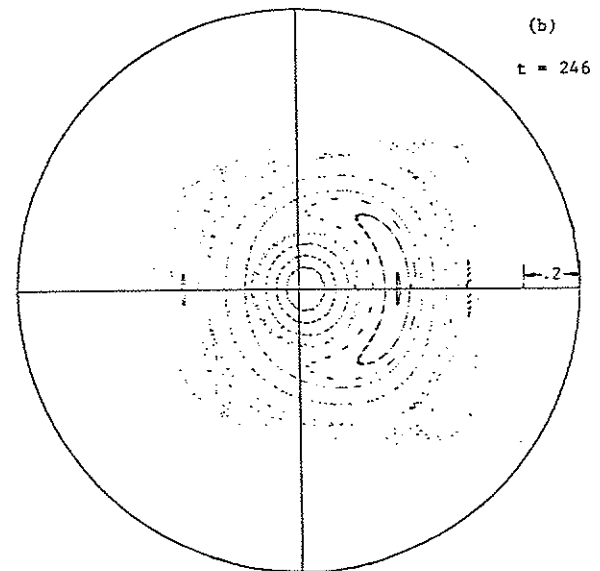
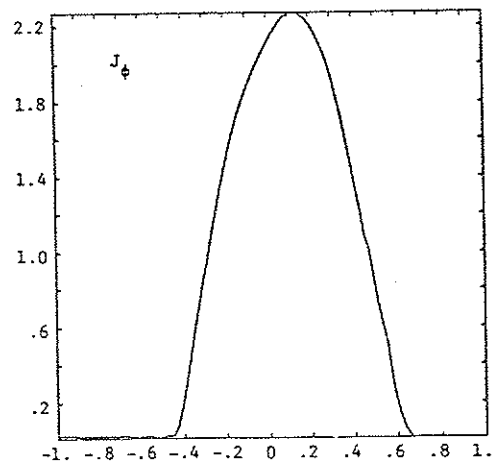
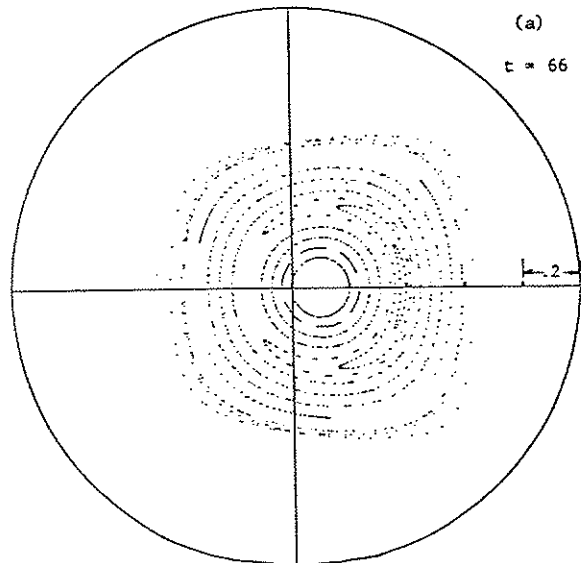
In cases 1 and 2, the 1/1 island visible in the field line mapping plots starts to become ergodic at about the time that reconnection to flux outside the separatrix begins. The ergodicity of the 1/1 island seems to start at its center rather than at its edges. If the ergodicity was the result of overlap of the 1/1 island with the separatrix, or another island, the edges of the island would be expected to become ergodic first. The innermost island magnetic surfaces pinch off near the island magnetic axis to form the two smaller islands seen in figure 8-14b, and the ergodic region propagates outwards from this point. Most of the ergodicity appears to come from an interaction with the  $n=2$ . The two holes in figure 8-14b rotate with the 1/1 structure, indicating that whatever produces them is of nearly the same helicity. An examination of the mode amplitudes, and current perturbation profile plots shows that the additional mode is principally an  $m=n=2$ . The ratio of the  $m=n=1$  Fourier component of the current perturbation to the  $m=n=2$  component goes from 4.3 at  $t=10$  when very little ergodicity is seen, to 1.3 at  $t=25$  when the island is strongly ergodic. It is not clear from these cases if the transformation of the island magnetic surfaces to an ergodic region is directly attributable to interaction of the 1/1 mode with the separatrix, or related to the saturation mechanism.



The third case with  $S=1000$  gave another unexpected result (figure 8-16). Even though enough flux was available within the separatrix, the mode did not fully reconnect. This case was run for 476 poloidal Alfvén times, and the island sizes changed very little after  $t=300$ . A large  $2/1$  island and a small  $3/2$  island are also apparent in the field line maps. The  $2/1$  island began to appear at about  $t=100$ . The mechanism for the saturation is not clear.

The initial condition, for a fourth case with  $\eta$  a spacial constant and  $S=5000$ , placed the  $q=1$  surface again near the separatrix, so that insufficient helical flux was available for reconnection. This case exhibited the classic Kadomtsev flip with the island o-point becoming the magnetic axis (figure 8-17). Since the magnetic surfaces returned to axisymmetry, the final  $q$  profile could be determined from the field line mapping; as expected the  $q$  values are all above 1 (figure 8-18). It is possible that diffusion of the overall current density profile modified the process to allow the reconnection to continue. The gap between the central flux region remnant and the  $1/1$  island does occur for this case; however, this gap is filled in almost as rapidly as the reconnection opens it up. Also, although the outer surfaces of the island show some ergodicity, this disappeared by the time the flip was completed. Somehow, perhaps through reconnection across the separatrix x-points, flux from the region outside the separatrix is getting to the inside to form the island's outer surfaces. Another

FIG. 8-16. Magnetic surfaces and current density profile evolution for case 3 with  $S=1000$ . The times given correspond to poloidal Alfvén times. (b) is near the time the modes saturate. (c) shows the lack of island growth.



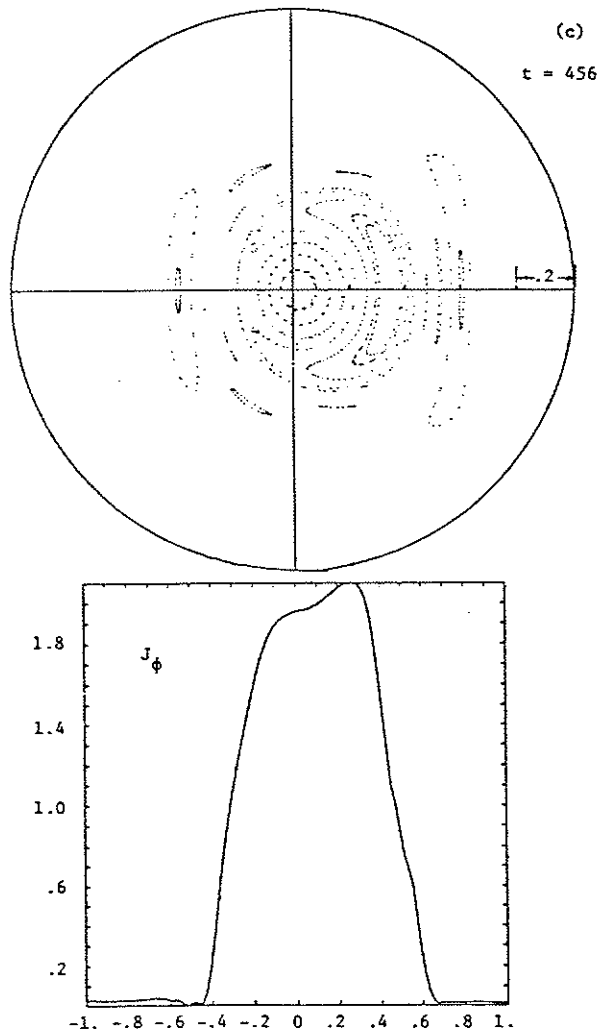
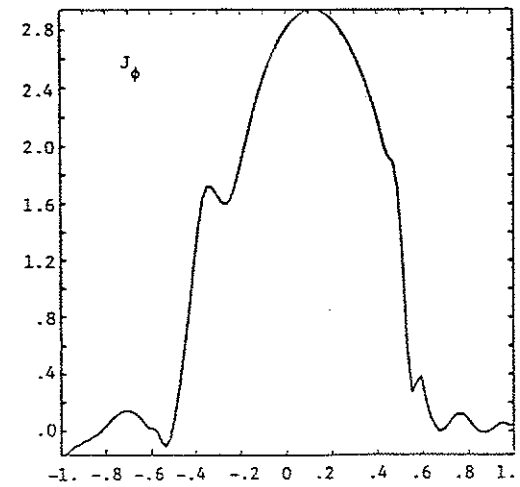
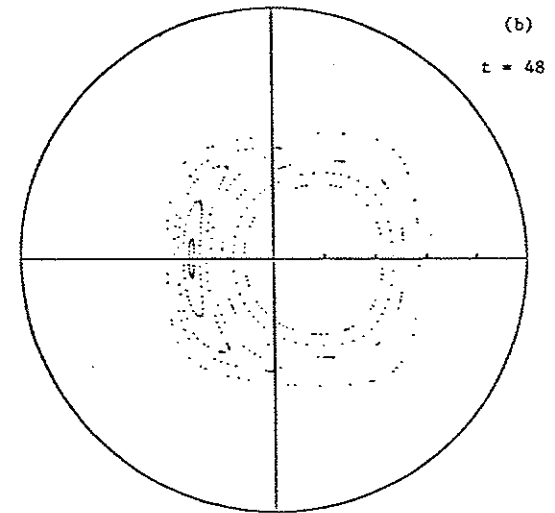
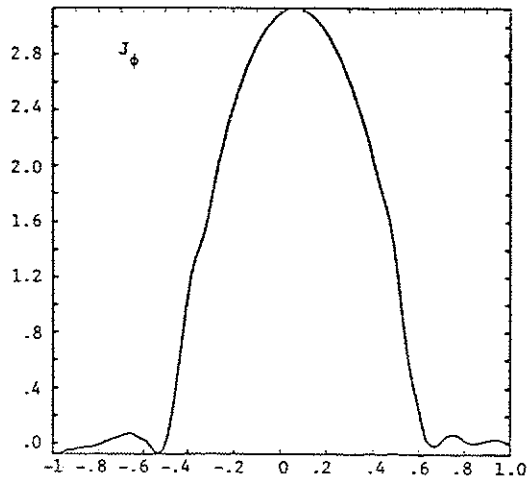
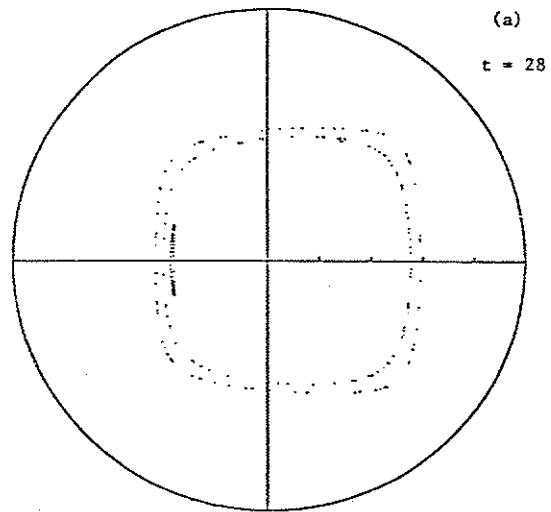


FIG. 8-17. Magnetic surfaces and current density profile evolution for case 4 with  $S=5000$  and constant resistivity show the flip in the magnetic topology that would be expected from the Kadomtsev model. The times given correspond to poloidal Alfvén times. (c) shows reconnection to flux outside the separatrix; (d) shows the return to axisymmetry and total flattening of the current density profile after complete reconnection.



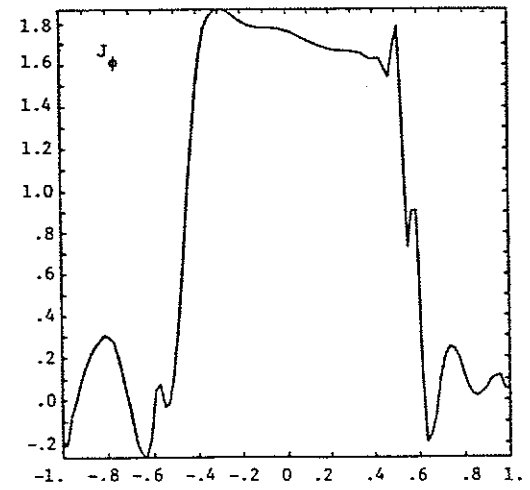
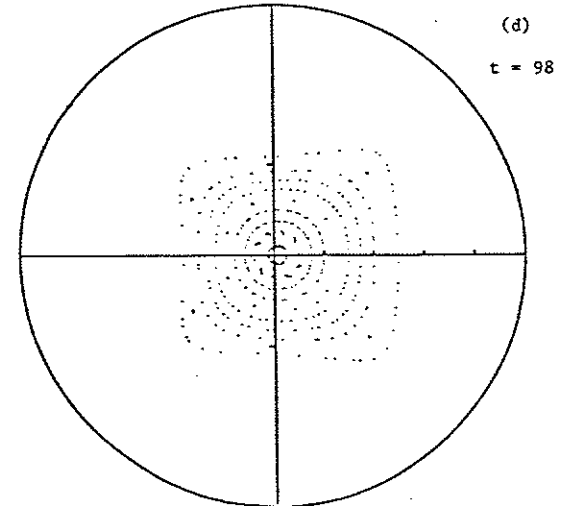
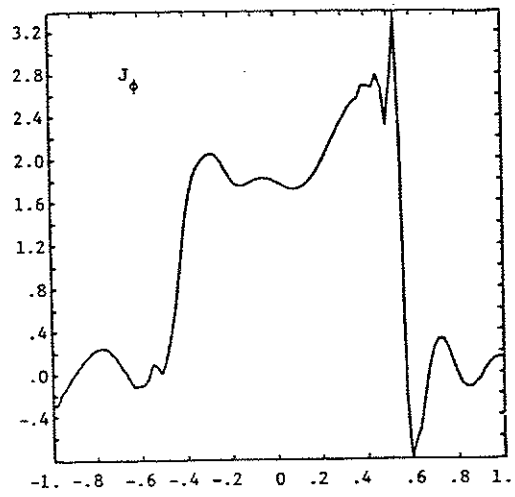
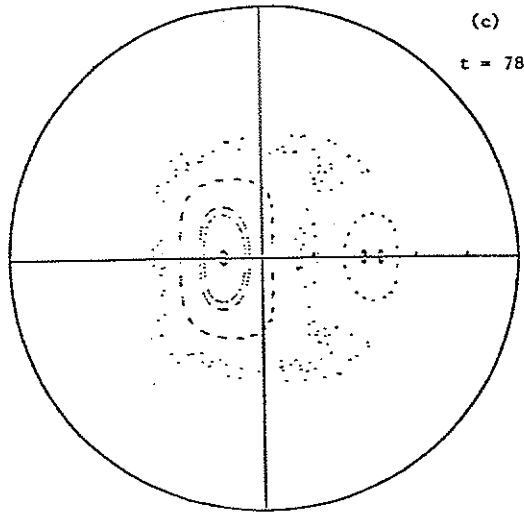
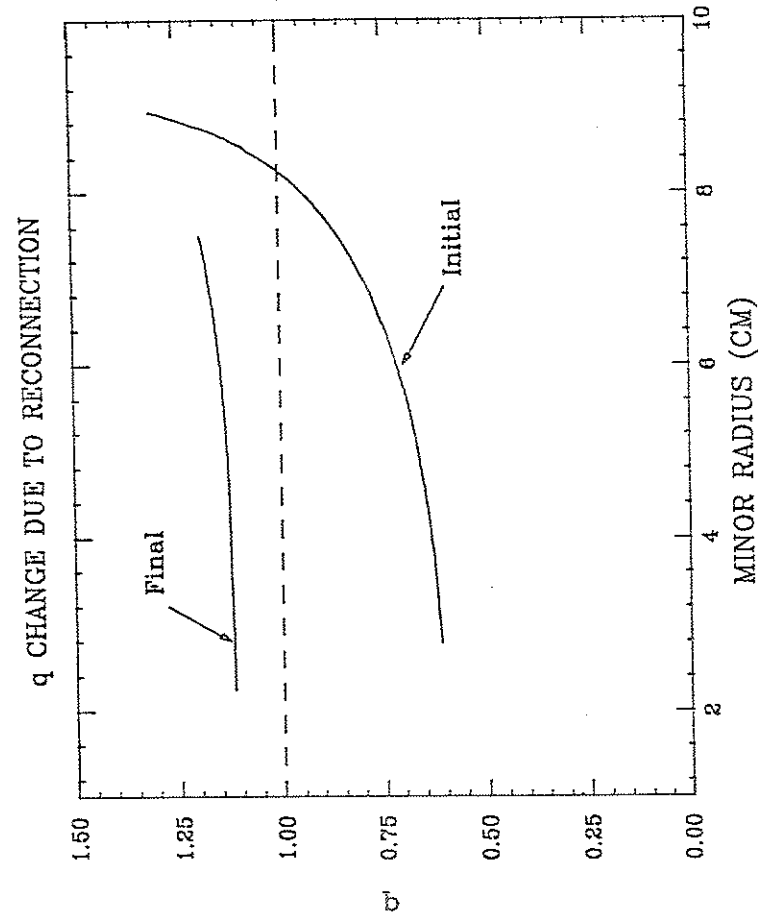


FIG. 8-18. Initial and final  $q$  profiles for the HIB run with  $S=5000$  show the expected relaxation of  $q$  to values greater than 1.



possibility is that resistive diffusion somehow raises the  $q$  values at the edge of the central flux region above 1, thus creating extra helical flux on the inside of the separatrix, allowing the reconnection to continue without involving flux outside the separatrix.<sup>8</sup> The time for this flip to occur was just 200 poloidal Alfvén times, which is 1/25 of the characteristic resistive diffusion time.

#### F. Parameter Scaling and Confinement at Low $q$

The energy confinement time for the  $\langle q \rangle < 1$  discharges is very poor.  $\tau_E \approx 50 \mu s$ , compared to the higher  $q$  discharges,  $\tau_E \approx 600 \mu s$ . The large energy loss in the low  $q$  discharges does not seem to be the result of the sawtooth oscillations. A comparison of an estimate of the change in the central  $T_e$  during the sawtooth ramp up from equation 3.5, to the input ohmic heating power, reveals that the energy confinement is as poor during this stage, as when averaged over several sawteeth. This is in contrast to the DIVA results<sup>3</sup> that show good confinement during the sawtooth ramp up.

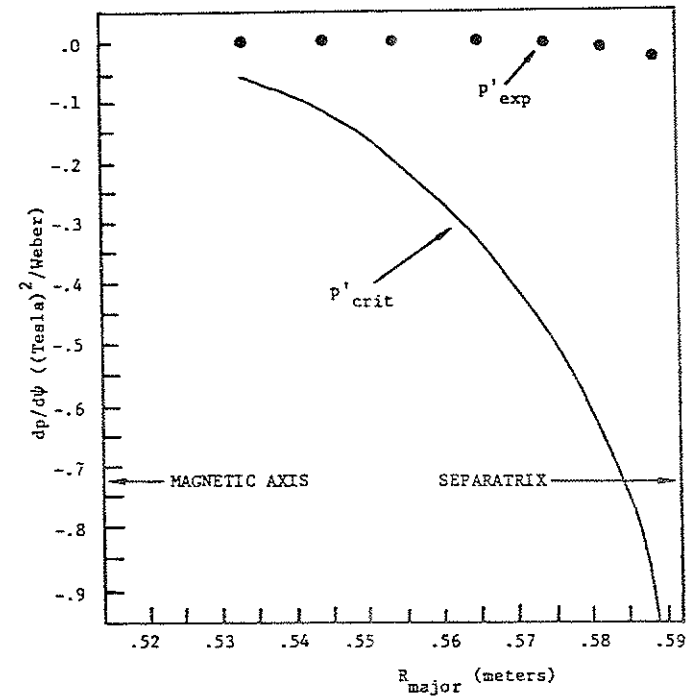
Since  $q$  is less than 1, equation 2.7 indicates that the discharges may be unstable to localized interchange modes if the shear of the magnetic field is small enough. Because the low  $q$  discharges have flat  $q$  profiles, it seemed possible that the poor energy confinement at low  $q$  could be related to interchange mode instability. To determine if the low  $q$  profiles were unstable, the

pressure gradient for marginal stability was computed in Tokapole II geometry from the Mercier stability criteria.<sup>9</sup>

$$\frac{dp/d\psi}{F(2\pi dq/d\psi)^2} \left[ \left[ \psi \left( \frac{\partial J}{\partial \psi} - \frac{dp}{d\psi} \frac{J}{B_p^2} \right) d\psi \right] \left[ \psi \frac{vB^2}{B_p^2} d\psi \right] + \left[ F \frac{dp}{d\psi} \psi \frac{vd\psi}{B_p^2} - 2\pi \frac{dp}{d\psi} F \right] \left[ \psi \frac{vd\psi}{B_p^2} \right] \right] + \frac{1}{4} = 0 \quad (8.10)$$

where the integrals are taken over a flux surface.  $B_p$  is the poloidal field.  $B$  is the total field.  $Jd\psi = dl/B_p$ ,  $F = RB_\phi$  (a constant on a flux surface), and  $v = JF/R^2$ . The critical pressure gradient,  $dp/d\psi$ , was computed from equation 8.10 for an MHD equilibrium with a  $q$  profile that matched the case of 7/31/81. In figure 8-19, this result is compared to  $dp/d\psi$ , computed from a fit of the experimental SXR profile at a sawtooth peak to simulated profiles determined from  $p(\psi)$ . The results indicate that even the modest shear present in the low  $q$  plasmas is sufficient to stabilize localized interchange modes for the very low  $\beta$  values of these discharges. If resistivity is included in a stability analysis of the interchange mode, the stabilizing effect of magnetic shear is weakened because the plasma is no longer locked to field lines. A stability computation in this case is much more difficult and was not done. It is possible that these modes are unstable, especially at the low  $S$  values that occur in the  $q < 1$  discharges.

FIG. 8-19 Pressure gradient predicted for marginal stability to localized interchange modes from an equilibrium with a  $q$  profile and gross plasma parameters that matched the  $q$  profile at the sawtooth peak in figure 8-7 is far larger than the pressure gradient inferred from the SXR profile for these discharges.





The poor energy confinement of the low  $q$  discharges may not be related directly to  $q$ , but may be associated with the large driving voltages. A scan was done in  $B_\phi$  using the quarter sine wave  $V_{pg}$ . During the time that  $V_{pg}$  was large,  $\tau_E$  was poor, independent of  $q$  (figure 8-20). This might, in some way, be associated with the unusual pressure or current profiles that may be created by the large  $V_{pg}$ . A comparison of the SXR profiles for the low  $q$  case, and for the high  $q$  cases after the period of large  $V_{pg}$ , is shown in figure 8-21.<sup>10</sup> This data was taken over several shots and so reproducibility is somewhat uncertain, but the low  $q$  case does indicate a somewhat hollow temperature profile.

Scans were done vs  $V_{pg}$  for various  $B_\phi$  values, with and without the baffle plates inserted. The value of  $I_p$  at 2ms was maximized by varying the density. This time was chosen because it was believed to correspond more closely to the actual time at which  $I_p$  peaked. No obvious saturation was found in  $\langle q \rangle$  values as low as 0.4 were obtained (figure 8-22). Throughout the range of  $V_{pg}$  values,  $I_p/B_\phi$  was found to be nearly independent of  $B_\phi$  (figure 8-23) this indicates a scaling in  $\langle q \rangle$  at  $V_{pg}/2=9.25V$  (typical low  $q$  discharge) of

$$\langle q \rangle = 23 \left( \frac{B_\phi}{I_{rings}} \right)^{1/2} \quad (8.7)$$

where  $B_\phi$  is in tesla and  $I_{rings}$  is the total ring current in kAmps.

FIG. 8-20 Energy confinement time inferred from the external plasma parameters at a time when the poloidal gap voltage is large is independent of  $q$ .

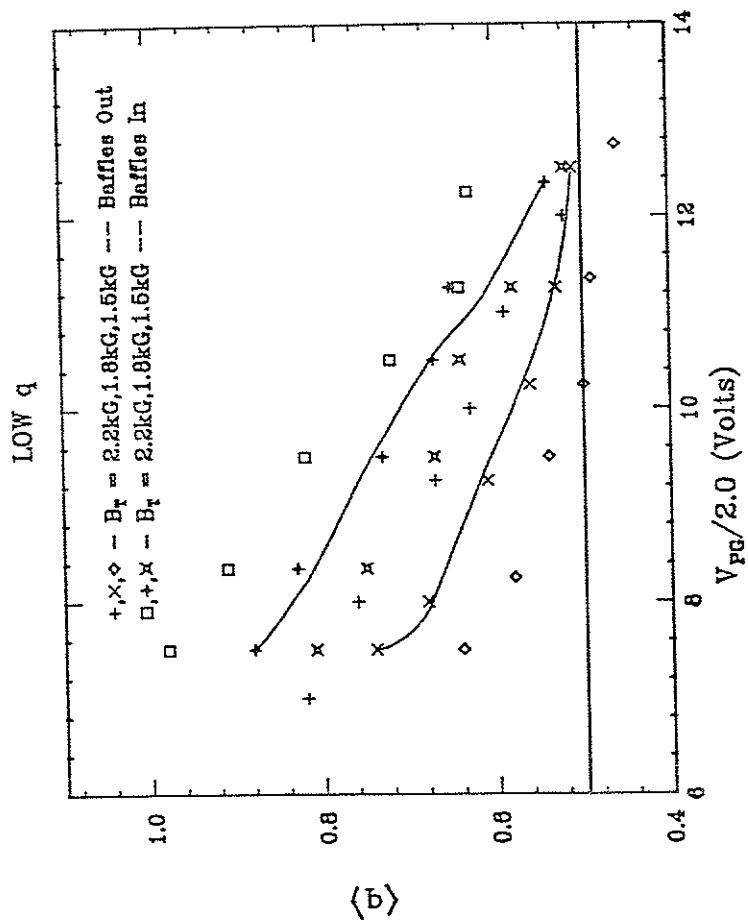
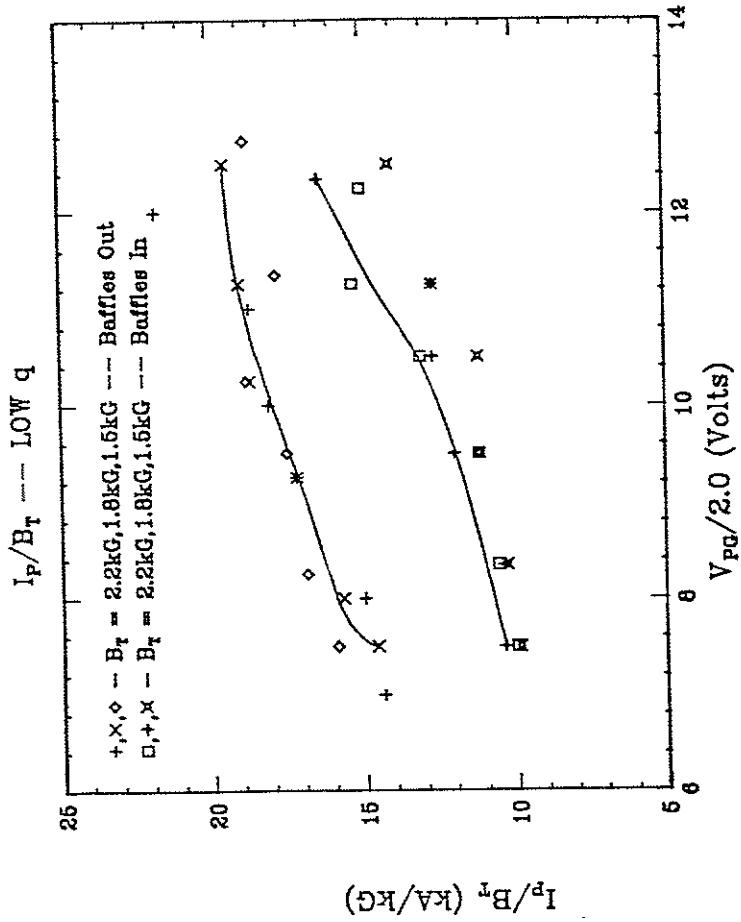


FIG 8-23  $I_p$  is proportional to  $B_\phi$  at a fixed  $V_{pg}$  (and density) except at the higher  $V_{pg}$  values.



If it is assumed that  $V_{pg}/2 = V_{loop}$  which would be true if the peak of  $I_p$  were actually at 2ms. then using the plasma minor radius computed from equation (4.1).  $\eta$  can be computed. The data indicates that  $\eta \sim 1/\langle q \rangle$  for the low  $q$  discharges (figure 8-24).

2/1 island depend on current density profile. The current density profile is determined by the radial dependence of the heating and cooling rates which determine the resistivity profile. Presently, the uncertainty of the  $J_{\phi}$  profiles for the high  $q$  cases is very large. A SXR array, using a single filter for all detectors, would provide an emissivity profile on a single shot. A  $J_{\phi}$  profile inferred from this data might provide enough certainty to justify a detailed theoretical calculation. A code to evaluate the linear stability would use much less computer time than the nonlinear HIB code, and might help identify which profile effects are important. A SXR array with enough spacial resolution to identify the structure of the precursor oscillations for this case (approximately 30 channels across the poloidal cross section will be needed) could provide a large amount of information. Not only could the modes involved be identified, but also the inversion radii of the oscillations could locate the position of the mode rational surfaces and help with current profile determination. With more control over  $v_{pg}$ , it might be possible to vary the  $J_{\phi}$  profile and affect the development of the instabilities. By extending the baffle plates, it will be possible to test the conjecture that the fact that the plates do not reach the separatrix prevents the termination of  $I_p$  in the disruption.

The case with  $1.5 < \langle q \rangle < 2$  could represent the elimination of the 2/1 disruption, without the aid of a conducting wall near the plasma surface. The  $q$  values for this case should be determined

more carefully. This could be done by combining the profile and sawtooth inversion radii data from a single filter SXR array with external measurements of  $B_{pol}$  with probes, as input into an MHD equilibrium code. An improved SXR array may also be useful in identifying modes other than the 1/1 that are suggested by the existing data. A calculation of the linear stability of the 2/1 and other modes could reveal what details of Tokapole II make it different from other poloidal divertor tokamaks with no conducting boundary, in which the achievement of  $q < 2$  operation has not been possible. A number of possibilities suggest that the separatrix in Tokapole II may always be ergodic, including the interaction of modes generated at the many rational value  $q$  surfaces in this area, an interaction of these modes with the separatrix, a nonaxisymmetry in the ring position, or a combination of these effects. The experimental evidence for the suppression of the 2/1 mode with 3/1 helical windings on another tokamak (chapter 2), suggests that this possibility may have some validity. It may be possible to include these effects in HIB runs. The flattening of the pressure profile in an ergodic region near the separatrix might be observable with Langmuir probes. Extending the baffle plates to reach the separatrix will make the Tokapole very similar, in terms of profiles, to other divertor tokamaks:  $\langle q \rangle < 2$  operation then would not be expected.

The  $\langle q \rangle = 1$  case may be a unique experimental observation of a 1/1 disruption of the classic Kadomtsev type. The S value for these discharges in comparison to other tokamaks, in which the disruption associated with the 1/1 mode is poloidally and toroidally symmetric, is low. At low S, the current spike generated by the reconnection will not have a large current density gradient. Thus, the  $m, n > 1$  modes driven by this current density gradient, which could be responsible for the  $n=m=0$  structure of the disruption in the nonlinear phase, may not occur in the  $\langle q \rangle = 1$  case. It should be possible to verify this conclusion with magnetic probe measurements near the plasma edge. Qualitative simulations of these signals could be done with the existing HIB results. Simulations of the SXR data, assuming infinite thermal conductivity parallel to the magnetic field and zero perpendicular thermal conductivity, along with energy conservation, could also be done with the existing resistive MHD code output.

The observation of  $q < 1$  discharges, in which the q values do not relax to 1 during sawtooth oscillations, suggests that the reconnection process in the 1/1 mode is limited by some effect. The close proximity of the  $q=1$  surface to the separatrix for this case indicates that magnetic flux outside the separatrix must be involved in the reconnection, if this process is to proceed beyond the point at which the magnetic island reaches the separatrix. The uniqueness of the q observations, and their variance with the standard theory, suggest that the unusual attributes of the

separatrix in Tokapole II might be involved. Unfortunately, probes can no longer be inserted into the  $q < 1$  discharges because of their large perturbing effect, so that the magnetic probe data cannot be repeated with the knowledge of the toroidal asymmetry of the sawtooth oscillations. The transition of the modes observed in these discharges from nearly toroidally symmetric sawteeth to a distorted 1/1 mode needs further study to reveal what plasma parameters determine the degree of toroidal asymmetry in the 1/1 disruption. The HIB runs indicate that exhaustion of the helical flux supply within the separatrix does not stop the growth of the 1/1 island reconnection seems to continue across the separatrix, probably through the formation of an ergodic field region. An HIB run with current outside the separatrix will more accurately model the experiment, and may reconcile the experimental observations with resistive MHD. The field line mapping section of the code should be modified to allow q profiles to be computed even for a highly kinked case, in order to resolve the questions regarding resistive diffusion.

## APPENDIX

REDUCED RESISTIVE MHD EQUATIONS TO ORDER  $\epsilon^3$ 

The set of equations solved by the HIB computer code are the resistive MHD equations.

$$\frac{d\rho}{dt} = -\rho \nabla \cdot \vec{v} \quad (\text{A.1a})$$

$$\rho \frac{d\vec{v}}{dt} = -\nabla p + \vec{J} \times \vec{B} \quad (\text{A.1b})$$

$$\frac{\partial \vec{B}}{\partial t} = -\nabla \times \vec{E} \quad (\text{A.1c})$$

$$\frac{dp}{dt} = -\gamma p \nabla \cdot \vec{v} \quad (\text{A.1d})$$

$$\vec{E} = \eta \vec{J} - \vec{v} \times \vec{B} \quad (\text{A.1e})$$

$$\vec{J} = \nabla \times \vec{B} \quad (\text{A.1f})$$

where  $d/dt$  is the convective derivative  $\partial/\partial t + \vec{v} \cdot \nabla$ ,  $\rho$  is the mass density,  $\vec{v}$  is the fluid velocity,  $p$  is the pressure, and  $\gamma$  is the ratio of specific heats. The assumptions made in the derivation of the reduced form of these equations used in HIB are 1) that the torus is of large aspect ratio  $\epsilon = a/R \ll 1$ , 2)  $B_{\perp} \sim \epsilon B_{\phi}$ , which holds for tokamaks with  $q > 1$ , 3) that the toroidal wavelengths are long compared to the poloidal scale lengths,  $\partial/R\partial\phi \sim \epsilon\partial/\partial l$  this

will be true for low mode number resonant modes because of assumption 2. 4)  $\nabla \cdot \vec{v} = 0$  this will be true provided that all modes grow at rates much slower than the sound speed time scale, so that flow along field lines can equalize any compression. 5) that the plasma pressure is small,  $\beta \sim \epsilon^2$ , and 6) that the growth times for the modes are long compared to the characteristic time for the propagation of a compressional wave in the  $B_{\phi}$  across the poloidal cross section (the "fast poloidal Alfvén time"). The goal of this ordering is to produce a consistent set of equations, accurate to order  $\epsilon^3$  in the dynamical equations, in which the perpendicular components of  $\vec{B}$  and  $\vec{v}$  are derivable from potential functions, and  $\tilde{B}_{\phi}$  and  $v_{\phi}$  are negligible. The coordinate system used in the solution takes  $\hat{x}$  in the direction of increasing major radius, and  $\hat{y} = \hat{\phi} \times \hat{x}$ .

Assumptions 5 and 6 are the key assumptions to the reduction of the equations (A.1) from a set with 3 velocity and magnetic field variables, to a set in which the velocity and magnetic field are derivable from 2 potential functions,  $\phi$  and  $U$ . Assumption 6 leads to a constraint on the velocity components in the poloidal plane similar to the constraint  $\nabla \cdot \vec{v} = 0$  that results from neglecting the sound wave time scale. Taking the  $\phi$  component of equation A.1c gives.

$$\frac{1}{RB_\phi} \left[ \frac{\partial(RB_\phi)}{\partial t} + \vec{v}_1 \cdot \nabla(RB_\phi) \right] = \frac{1}{B_\phi} \nabla_1 \cdot (\vec{v}_\phi \vec{B}) - R^2 \nabla \cdot \left( \frac{\vec{v}_1}{R^2} \right) + O\left(\frac{\epsilon^2}{S\tau_{HP}}\right) \quad (A.2)$$

Taking the  $\phi$  component of equation A.1b gives

$$\vec{\phi} \cdot \frac{d\vec{v}}{dt} = \frac{v_A}{\tau_{HP} \epsilon} \frac{a}{RB_\phi} \left( \frac{\vec{B}_1}{B_\phi} \cdot \nabla \right) RB_\phi + O\left(\frac{\epsilon^2 v_A}{\tau_{HP}}\right) \quad (A.3)$$

where  $v_A$  is the Alfvén speed in the toroidal field  $(B_\phi^2/\rho)^{1/2}$ . Since  $\beta \sim \epsilon^2$  and the time scale for the relaxation of compressions in the toroidal field is neglected the left hand side of equation A.2. can only produce changes in  $RB_\phi \sim \epsilon^2 RB_\phi$  by convection in the poloidal plane so that the left hand side of equation A.2  $\sim (\epsilon^2/\tau_{HP})$ . From equation A.3 under the same assumptions  $v_\phi \sim \epsilon^2 v_A$  since the poloidal Alfvén time is the fastest time scale allowed. Applying this last ordering into equation A.2 and assuming  $S \sim 1/\epsilon$  (a very modest assumption).

$$R^2 \nabla \cdot \left( \frac{\vec{v}_1}{R^2} \right) \sim \frac{\epsilon^2}{\tau_{HP}} = \frac{\epsilon^3 v_{HP}}{a} \quad (A.4)$$

which is the desired constraint on the poloidal flows. Thus  $\vec{v}_1$  can be written as.

$$\vec{v}_1 = \frac{R^2}{R_0} (\nabla U \times \nabla \phi) + O(\epsilon^3 v_{HP}) \quad (A.5)$$

The final term is of such an order that it does not enter into the dynamical equations.

$\vec{B}$  can always be written as

$$\vec{B} = R_0 \nabla \phi \times \nabla \phi + b_{31} \vec{e}_1 + RB_\phi \nabla \phi. \quad (A.6)$$

Taking the divergence of A.6 and again invoking the fact that  $RB_\phi$  can change by convection only, and that because of the low  $\beta$ , this change can only be  $O(\epsilon^2 RB_\phi)$  gives

$$\nabla \cdot b_{31} \vec{e}_1 \sim \frac{\epsilon^3 B_\phi}{a} \quad (A.7)$$

so that

$$\vec{B}_1 = R_0 \nabla \phi \times \nabla \phi + O(\epsilon^3 B_\phi) \quad (A.8)$$

As in the poloidal velocity the third order term in the poloidal field does not enter the dynamical equations to the lowest order retained. Operating on A.8 with  $\nabla_1 \times$  gives

$$\Delta^* \phi = \nabla_1^2 \phi - \frac{1}{R} \frac{\partial \phi}{\partial R} = - \frac{R}{R_0} J_\phi. \quad (A.9)$$

To obtain the  $\phi$  time dependent equation operate with  $\hat{\phi} \times$  on equation A.1c to give an equation involving the poloidal components of  $\vec{B}$

$$\nabla_{\perp} \frac{\partial \phi}{\partial t} = -\nabla_{\perp} \left( \frac{R}{R_0} \hat{\phi} \cdot \vec{E} \right) + \frac{\hat{\phi}}{R_0} \times \frac{\partial}{\partial \phi} (\hat{\phi} \times \vec{E}) \quad (\text{A.10})$$

Substituting ohms law (A.1e) into the second term on the right of A.10 after some algebra gives.

$$\nabla_{\perp} \frac{\partial \phi}{\partial t} = -\nabla_{\perp} \left( \frac{R}{R_0} \hat{\phi} \cdot \vec{E} - \frac{B_{\phi} R}{R_0^2} \right) + O\left(\frac{e^4 B_{\perp}}{a \tau_{HP}}\right) \quad (\text{A.11})$$

Since pure functions of  $\phi$  will not enter in computing  $B_{\perp}$  from A.8.  $\nabla_{\perp}$  operator can be dropped in the above equation. Substituting in  $E_{\phi}$  from ohms law and using A.5 and A.9 gives.

$$\frac{\partial \phi}{\partial t} = -\eta \Delta^* \phi + \frac{R^2}{R_0^2} \hat{\phi} \cdot \nabla U + O\left(\frac{e^4 B_{\perp}}{a \tau_{HP}}\right). \quad (\text{A.12})$$

Defining  $D/dt$  as the convective derivative in the poloidal plane. A.12 can also be written as

$$\frac{D\phi}{dt} = -\eta \Delta^* \phi + \frac{R}{R_0} B_{\phi} \hat{\phi} \cdot \nabla U + O\left(\frac{e^4 B_{\perp}}{a \tau_{HP}}\right). \quad (\text{A.13})$$

Equation A.13 shows that convection of  $\phi$  in the poloidal plane is driven by resistive diffusion and by any lack of toroidal symmetry in the flows.

The equation for the flows in the poloidal plane is obtained by operating on the momentum equation (A.1b) with  $\hat{\phi} \cdot \nabla \times (R^2)$ ; this eliminates  $v_{\phi}$  and results in an equation for essentially the vorticity of a 2-D flow with some toroidal corrections. Applying this operator to the force terms in A.1b gives

$$\hat{\phi} \cdot \nabla \times (R^2 (\vec{J} \times \vec{B})) = R (\vec{B} \cdot \nabla) R J_{\phi} + O\left(\frac{R^2 \epsilon^3 \rho v_A}{a \tau_{HP}}\right). \quad (\text{A.14a})$$

$$\hat{\phi} \cdot \nabla \times (R^2 \nabla p) = 2R \hat{\phi} \cdot \nabla R \times \nabla p + O\left(\frac{R^2 \epsilon^3 \rho v_A}{a \tau_{HP}}\right). \quad (\text{A.14b})$$

Using this operator on the left side of A.1b and combining equation A.1a and A.5 give

$$\hat{\phi} \cdot \nabla \times \left( R^2 \rho \frac{d\vec{v}}{dt} \right) = -R_0 \rho_0 R \left[ \frac{D}{dt} (\nabla \cdot \nabla_{\perp} U) + \frac{2}{R_0} \frac{\partial U}{\partial y} (\nabla \cdot \nabla_{\perp} U) \right]. \quad (\text{A.15})$$

Defining the vorticity  $W = \nabla \cdot \nabla_{\perp} U$  and putting together A.14 and A.15 give

$$\rho_0 \left[ \frac{DW}{dt} + \frac{2}{R_0} \frac{\partial U}{\partial y} W \right] = (\vec{B} \cdot \nabla) \Delta^* \phi + 2 \hat{\phi} \cdot \nabla \frac{R}{R_0} \times \nabla p + O\left(\frac{\epsilon^3 \rho_0 v_A}{a \tau_{HP}}\right). \quad (\text{A.16})$$



The vorticity is driven by variations of  $RJ_\phi$  on a magnetic surface through the second term on the right in equation A.16 the derivatives of this term in the toroidal direction in conjunction with the second term on the right of equation A.13 generate the toroidal mode coupling effects. A viscosity term of the form  $\mu v^2 w$  is added to A.16 for numerical stability this term has no effect on the physics of the results provided that the viscous damping time is much less than the resistive time.<sup>3</sup>

Equation A.13 and A.16 are solved in NIB by Fourier expanding in toroidal and poloidal angle with a grid in the radial direction. This has a great advantage over a 3-D grid since the most unstable modes turn out to have low mode number with most of the radial structure localized in a small region. This last fact allows grid packing to be used near the reconnection radius only, and reduces the number of radial grids needed to adequately resolve the structure. In the runs for Tokapole II geometry  $n=0$  to 4,  $m=-4$  to 8, and up to 100 radial grids were used.

The technique used in the solution of A.13 and A.16 is a semi-implicit half time step method in which the convective terms are advanced explicitly, and the dissipative terms implicitly.

$$\frac{\xi(t+\Delta t/2)}{\Delta t/2} = C(t) + D(t+\Delta t/2), \quad (\text{A.17a})$$

$$\frac{\xi(t+\Delta t)}{\Delta t} = C(t+\Delta t/2) + D(t+\Delta t), \quad (\text{A.17b})$$

where  $\xi$  represents a dependent variable  $C$  represents the convective terms and  $D$  represents the dissipative terms. This technique allows numerical stability with a much larger time step than would be possible in a fully explicit method.<sup>4</sup> Unfortunately, for the cases in Tokapole II geometry in which  $\eta \sim 1/J_\phi$ ,  $\eta$  is a function of both  $r$  and  $\theta$  so that the dissipative term in the  $\phi$  equation is a convolution that cannot be handled implicitly in the Fourier analysis. There is a provision in NIB that allows for the  $\eta \Delta^* \phi$  term to be advanced at a smaller time step than the rest of the code so that not all the advantages of an implicit time step are lost. Generally a time step of 0.01 was sufficient for the constant  $\eta$  case with  $S=5000$ . For the cases with  $S=1000$  and  $\eta \sim 1/J_\phi$ , a time step of 0.01 was used with the  $\eta \Delta^* \phi$  term advanced at a time step of 0.001

## References for Appendix

- <sup>1</sup>R. Izzo, D.A. Monticello, W. Park, J. Manickam, H.R. Strauss, R. Grimm and K. McGuire PPPL Report-1982 (1983).
- <sup>2</sup>R. Izzo, D.A. Monticello and W. Park. private communication.
- <sup>3</sup>W. Park, D.A. Monticello and R.B. White Phys. Fluids, 27, 137 (1984).
- <sup>4</sup>G.D. Smith Numerical Solution of Partial Differential Equations: Finite Difference Methods Clarendon Press, Oxford (1978).